STUDIES ON PREPARATION AND MAGNETIC AND ELECTRICAL PROPERTIES OF TERNARY RARE EARTH FIRST-ROW TRANSITION METAL SILICIDES

Hiroyasu KIDO

STUDIES ON PREPARATION AND MAGNETIC AND ELECTRICAL PROPERTIES OF TERNARY RARE EARTH FIRST-ROW TRANSITION METAL SILICIDES

(三成分系希土類第一遷移金属ケイ化物の合成と磁気的および電気的性質に関する研究)

Hiroyasu KIDO

CONTENTS

CHAPTER 1	INTRODUCTION	1
1-1	Binary transition metal silicides and rare-earth metal silicides	1
1-2	Ternary rare-earth transition metal silicides and germanides RM_2X_2 (R: rare-earth metal, M: transition metal, X: Si or Ge)	6
1-3	Ternary rare-earth transition metal silicides RMSi (R: rare-earth metal, M: first-row transition metal)	11
CHAPTER 2	EXPERIMENTAL PROCEDURE	15
2-1	Starting materials	15
2-2	Methods of Synthesis	15
2-2-1	Synthesis using an evacuated silica tube	15
2-2-2	Synthesis using high pressure apparatus	16
2-2-3	Synthesis using an induction furnance	16
2-3	Identification of products	17
2-4	Measurements of magnetic properties	17
2-5	Measurements of electrical resistivity	17
2-6	Measurements of thermoelectric power	18
CHAPTER 3	EXPERIMENTAL RESULTS	20
3-1	Preparation and magnetic properties of GdTiSi	20
3-2	Preparation and magnetic and electrical properties of RMnSi (R=Y, Ce, Nd, Sm, Gd)	23

3-3	Preparation and magnetic and electrical properties of RCoSi (R=Nd, Gd, Tb, Ho)	37
3-4	Preparation and magnetic and electrical properties of RNiSi (R=Nd, Gd)	50
3-5	Preparation and magnetic and electrical properties of RCuSi (R=Y, Ce, Nd, Sm, Gd, Tb, Dy, Ho)	55
3-6	Preparation and magnetic and electrical properties of RZnSi (R=Y, Ce, Nd, Sm, Gd, Tb, Dy, Ho)	63
3-7	Preparation and magnetic and electrical properties of $GdCu_{1-x}Zn_xSi$ ($0 \leq x \leq 1$)	73
3-8	Preparation and magnetic and electrical properties of $DyCu_{1-x}Zn_xSi$ ($0 \leq x \leq 1$)	85
3-9	Preparation and magnetic and electrical properties of $HoCu_{1-x}Zn_xSi$ ($0 \leq x \leq 1$) and $NdCu_{0.6}Zn_{0.4}Si$	91
3-10	Preparation and magnetic properties of RMn_2Si_2 (R=Y, Nd, Gd) and YNi_2Si_2	98
3-11	Preparation and magnetic properties of $YMn_2(Si_{1-x}Ge_x)_2$ ($0 \leq x \leq 1$)	105
CHAPTER 4	DISCUSSION	113
4-1	Crystal structures of RMSi compounds	113
4-2	Magnetic and electrical properties of RMnSi, RCoSi and RNiSi compounds	127
4-3	Magnetic and electrical properties of RCuSi, RZnSi and $RCu_{1-x}Zn_xSi$ compounds	132

4-4 Magnetic properties of RMn_2Si_2 and $YMn_2(Si_{1-x}Ge_x)_2$ compounds 141

4-5 Thermoelectric power of RZnSi compounds 144

4-6 Solid state chemistry of rare-earth first-row transition metal silicides 146

CHAPTER 5 SUMMARY 148

ACKNOWLEDGMENTS 153

REFERENCES 154

PUBLICATION LIST 161

PREFACE

The research work described in this thesis was carried out under the guidance by Professor Mitsue Koizumi at the Institute of Scientific and Industrial Research, Osaka University.

The purpose of the present research is to prepare the ternary rare-earth first-row transition metal silicides and to examine their magnetic and electrical properties.

The author hopes that the findings obtained in this study would give the valuable suggestions for the development of this field.

CHAPTER 1

INTRODUCTION

In this chapter, as the background of the present studies, binary transition metal silicides and rare-earth metal silicides are briefly surveyed on their preparations, crystal structures and physical properties. Then, studies on ternary rare-earth transition metal silicides and germanides are described. Finally, the reason why the rare-earth transition metal silicides with formula of RMSi are chosen as the main subject of the present study is described.

1-1 Binary transition metal silicides and rare-earth metal silicides

The first systematic preparations of transition metal silicides were carried out by Moissan at about the turn of the century. But progress in this field was rather slow until 1950's (1). Then it was found that binary transition metal silicides had a considerable resistance to the attack of acids and bases and to oxidation in air. By these advantages in industrial applications such as electrodes within strongly acidic and basic electrolytes and heating elements, extensive studies in these fields were accelarated from 1950's.

These compounds were usually prepared by the direct reaction of elements. In Table 1, binary transition metal silicides and rare-earth metal silicides already reported are listed. The crystallographycal parameters are summarized in ref. 1-2.

Table 1 Binary silicides

Sc_5Si_3	Ti_3Si	V_3Si	Cr_3Si	Mn_3Si	Fe_3Si	Co_3Si	Ni_3Si	Cu_3Si
	Ti_5Si_3	V_5Si_3	Cr_5Si_3	Mn_5Si_3	Fe_5Si_3	Co_2Si	Ni_5Si_2	CuSi
	TiSi	VSi_2	CrSi	MnSi	FeSi	CoSi	Ni_2Si	
	$TiSi_2$		$CrSi_2$	$MnSi_2$	$FeSi_2$	$CoSi_2$	NiSi	
							$NiSi_2$	
Y_5Si_4	Zr_3Si	Nb_3Si	Mo_3Si		Ru_2Si	Rh_2Si	Pd_3Si	
YSi	Zr_2Si	Nb_5Si_3	Mo_5Si_3		RuSi	Rh_5Si_3	Pd_2Si	
YSi_2	Zr_3Si_2	$NbSi_2$	$MoSi_2$		Ru_2Si_3	Rh_3Si_2	PdSi	
	ZrSi					RhSi		
La_5Si_4	Hf_2Si	Ta_3Si	W_5Si_3	Re_5Si_3	OsSi	Ir_3Si	Pt_3Si	
LaSi	Hf_3Si_2	Ta_2Si_3	WSi_2	ReSi	Os_2Si_3	Ir_2Si	Pt_2Si	
$LaSi_2$	HfSi	$TaSi_2$		$ReSi_2$		Ir_3Si_2	PtSi	
	$HfSi_2$					IrSi		
						$IrSi_3$		

Ce_5Si_4	Pr_5Si_4	Nd_5Si_4	Sm_5Si_4	$EuSi_2$	Gd_5Si_4	Tb_5Si_4	Dy_5Si_4	HoSi	Er_5Si_4
CeSi	PrSi	NdSi	SmSi		GdSi	TbSi	DySi	$HoSi_2$	ErSi
$CeSi_2$	$PrSi_2$	$NdSi_2$	$SmSi_2$		$GdSi_2$	$TbSi_2$	$DySi_2$		$ErSi_2$

$TmSi_2$	$YbSi_2$	Lu_5Si_4	
		$LuSi_2$	

Most of binary transition metal silicides have the metal content greater than 33 atom% except $IrSi_3$ (3,4). The first-row transition metal silicides with metal content less than 33 atom% could not be synthesized even in the high pressure (3 GPa) and high temperature (1800°C) conditions (5).

The crystal structure, electrical and magnetic properties of the first-row transition metal silicides are summarized in Table 2 (6,7). Although all monosilicides, except NiSi, have the cubic B20-type crystal structure, they show the various electrical and magnetic properties. CrSi is paramagnetic with a temperature independent susceptibility in the temperature range from 1.5K to 300K. MnSi is the itinerant helimagnet (8-18). FeSi is paramagnetic with an unusual temperature dependence of the susceptibility having a pronounced maximum at around 500K (19). However, no spin alignment have not been observed by neutron diffraction (20,21). CoSi is diamagnetic with a temperature independent susceptibility (22,23). NiSi is diamagnetic with a temperature independent susceptibility (24). The $Fe_{1-x}Co_xSi$ solid solutions are ferromagnetic in the composition range from x=0.2 to x=0.8 (25-27). The crystal structure of MnMSi (M=Co, Ni) compounds are orthorhombic Co_2P-type structure at room temperature (28,29). MnNiSi and $MnCo_{1-x}Ni_xSi$ ($0.25 \leq x \leq 1$) were ferromagnetic above 4.2K and MnCoSi is noncollinear antiferromagnet (30). The magnetic spin structure of Mn and Co in MnCoSi is collinear at room temperature in which magnetic moments are parallel to the b-axis, but at 80K it changes to a complex helicoidal order with the wave vector parallel to the c-axis (31,32).

Table 2 Crystal structure and magnetic and electrical properties of first-row transition metal silicides

Compound	Crystal structure	Magnetic property	Electrical property
CrSi	cubic (B20)	constant para.	metallic
MnSi	cubic (B20)	ferro.	metallic
FeSi	cubic (B20)	unusual para.	semicon. and metallic
CoSi	cubic (B20)	dia.	semimetallic
NiSi	ortho. (B31)	dia.	metallic
$CrSi_2$	hexa. (C40)	dia.	semicon.
$MnSi_2$	tetra.	metamag.	semicon.
$FeSi_2$	tetra.	unusual para.	metallic semicon.
$CoSi_2$	cubic (C1)	constant para.	metallic

In both MnCoSi and MnNiSi compounds, the phase transitions from the orthorhombic Co_2P-type to the hexagonal Ni_2In-type were observed at 917 °C and 933 °C (33).

Disilicides show the more various crystal structures and their electrical and magnetic properties widely change depending upon the kinds of transition metals. $CrSi_2$ is semiconductor and diamagnetic (6,7). $MnSi_{1.72}$ is metamagnet. $FeSi_{2.43}$ is metallic and shows unusual paramagnetism similar to FeSi. $FeSi_2$ is a semiconductor (34). $CrSi_2$, $MnSi_{1.72}$ and $FeSi_2$ have the large thermoelectric power (35).

Rare-earth monosilicides RSi (R=La-Er) have the FeB-type structure (36) and YSi has the CrB-type structure (37). Rare-earth monosilicides, except PrSi and NdSi, are antiferromagnetic (38,39). PrSi and NdSi are ferromagnetic.

According to the results reported by Perri et al. (40,41), rare-earth disilicides (R=La-Ho) have the composition of $RSi_{1.4}$, and their crystal structures are the distorted orthorhombic $ThSi_2$-type at low temperatures, but at high temperatures they transformed to the tetragonal $ThSi_2$-type structure. Rare-earth disilicides (R=Er, Tm, Lu) have the composition of RSi_2 and their crystal structures are the hexagonal AlB_2-type. Slightly different results were reported by Mayer et al. (42,43) using samples prepared by the amalgam method. They reported that rare-earth disilicides (R=Gd-Lu) had the composition of RSi_2 and their crystal structures were the hexagonal AlB_2-type. RSi_2 (R=Gd-Ho) changed the crystal structure from the AlB_2-type to the orthorhombic $ThSi_2$-type by heating the sample at 1600 °C. But in case of RSi_2 (R=Er-Lu) their crystal structures did not

change after heat treatment.

Magnetic properties of RSi_2 (R=Gd, Tb, Dy, Ho, Er) were investigated by Sekizawa et al. (44). These compounds, except $ErSi_2$, are antiferromagnetic. The Néel temperatures of $GdSi_2$, $TbSi_2$, $DySi_2$ and $HoSi_2$ are 27K, 17K, 17K and 18K, respectively. $ErSi_2$ is paramagnetic above 4.2K. They suggested that the ratio of the radius of 4f wave function to the atomic distance between rare-earth atoms was one of the important factors which decide the magnetic properties of RSi_2.

R_5Si_4 (R=Gd, Tb, Dy, Y) have the orthorhombic Sm_5Ge_4-type crystal structure, and the crystal structures of R_5Si_3 (R=Pr, Ce) are the body-centered tetragonal Cr_5B_3-type (45).

1-2 Ternary rare-earth transition metal silicides and germanides RM_2X_2 (R: rare-earth metal, M: transition metal, X: Si or Ge)

The ternary rare-earth transition metal silicides and germanides have more interesting electrical and magnetic properties than those of binary transition metal silicides, because both 3d and 4f electrons contribute to them. The studies in these fields started since the end of 1960's. So far, many investigations on RM_2X_2 compounds were performed.

The crystal structure of RM_2X_2 is the body-centered tetragonal $ThCr_2Si_2$-type (space group I4/mmm). The R, M and X atoms occupy the 2a, 4d and 4e sites, respectively. The RM_2X_2 compounds already reported are summarized in Fig. 1. Rieger et al. (46) prepared $GdCr_2Si_2$, RMn_2Si_2 (R=La, Ce), RFe_2X_2 (R=Ce, Gd), RCo_2X_2 (R=Ce, Gd) and RM_2X_2 (R=Y, La-Lu;

RM_2Si_2

M \ R	Y	La	Ce	Pr	Nd	Pm	Sm	Eu	Gd	Tb	Dy	Ho	Er	Tm	Yb	Lu
Ti																
V																
Cr									a							
Mn	b	b	a	b	b		b		b	b	b	b	b		b	
Fe	b	b	a	b	b				a		b				b	
Co	b	b	a	b	b		b		a	b	b	b	b		b	
Ni	a	a	a	a	a		a	a	a	a	a	a	a	a	a	a
Cu	a	a	a	a	a		a		a	a	a	a	a	a	a	a
Zn																

a) W. Rieger et al.

b) D. Rossi et al.

Fig. 1 Ternary rare-earth first-row transition metal silicides RM_2Si_2 (R: rare-earth metal, M: first-row transition metal).

M=Ni, Cu) by using the arc melting method. Rossi et al. (47, 48) prepared RCo_2Si_2 (R=Y, La-Sm, Gd-Er, Yb), RFe_2Si_2 (R=Y, La-Nd, Gd, Dy, Yb), RFe_2Ge_2 (R=La-Nd, Gd, Dy, Yb) and RMn_2Si_2 (R=Y, La-Sm, Gd-Er, Yb) by using the induction furnance under argon atmosphere. Mayer et al. (49) prepared RAu_2Si_2 (R=La-Eu, Dy, Er) by the induction melting.

The physical properties of RM_2X_2 have been investigated only on the magnetic properties for few compounds. In RFe_2Si_2 the R sublattice ordered antiferromagnetically below 50K for R=Nd, Gd and Tb, but magnetic ordering of the R sublattice was not observed for the compounds containing the other rare-earth elements (50). Most of iron atoms were diamagnetic due to the transfered electron from Si or Ge. The iron sublattice showed the ferromagnetic ordering at high temperatures (50,51). RCo_2Si_2 were antiferromagnetic for R=Gd, Dy, Er, but were ferromagnetic for R=Tb, Ho below about 50K (52). RCo_2Ge_2 were antiferromagnetic for R=Gd, Tb, Dy, Ho below 50K and paramagnetic for R=La, Ce, Sm, Eu, Tm, Yb, Y above 4.2K (53). The 3d shells of cobalt atoms in RCo_2X_2 were partially or fully filled with electrons. RCu_2Ge_2 (R=Gd, Tb, Dy, Ho) were antiferromagnetic with T_N=12K, 15K, 8K, 6.4K, respectively (54,55). RCu_2Ge_2 (R=Er, Tm) did not show any magnetic ordering down to 4.2K. RCu_2Si_2 (R=Pr, Gd, Tb, Dy, Ho) were antiferromagnetic with T_N below 20K (56,57). RCu_2Si_2 (R=Nd, Er, Tm) were ferromagnetic at 4.2K and paramagnetic above 20K. $CeCu_2Si_2$ showed a superconductivity (57-59). The superconductive transition temperature was below 0.7K, but this compound was the first noncubic material with unstable 4f-shell.

RAu_2Si_2 (R=Ce, Sm, Gd, Tb and Dy) were antiferromagnetic with T_N=6.6K, 15.9K, 5.7K, 14.8K and 7.5K, respectively. RAu_2Si_2 (R=Eu, Ho and Er) were ferromagnetic with T_c=15.5K, 14.8K and 40.0K, respectively. $PrAu_2Si_2$ and $NdAu_2Si_2$ were paramagnetic above 4.2K (60). RMn_2Ge_2 (R=La, Ce, Pr, Nd, Gd, Tb, Dy, Ho and Er) had T_c=306K, 316K, 334K, 334K, 97K, 33K, 47K, 37K, and 38K, respectively. $GdMn_2Ge_2$ also had T_N=365K. In RMn_2Ge_2, the magnetic moments of R and Mn atoms coupled ferromagnetically for the light rare-earth elements, but antiferromagnetically for the heavy rare-earth elements at low temperatures. At high temperatures, R spins did not order, and Mn spins order ferromagnetically for the light rare-earths but antiferromagnetically for the heavy rare-earths (61). It was suggested that RMn_2Si_2 (R=Ce-Nd, Gd-Ho) compounds showed the same magnetic behavior as RMn_2Ge_2 at low temperatures (62). At high temperatures, RMn_2Si_2, except $LaMn_2Si_2$, were antiferromagnetic with T_N higher than 300K (62-67). $LaMn_2Si_2$ was ferromagnetic with T_c=303K. $La_{1-x}Y_xMn_2Si_2$ showed ferromagnetism for $x<0.2$ and antiferromagnetism for $x>0.2$. The sample with x=0.2 showed the magnetic phase transition from antiferromagnetism to ferromagnetism when temperature was increased (66).

In recent years, neutron diffraction investigations on RM_2X_2 were carried out, and the results were somewhat different from those of magnetometric studies. These investigations indicated that in all these compounds, except RMn_2X_2, magnetic moments were localized only on R sublattices. Pinto et al. (68) showed that magnetic moments localized only on the Nd sublattice in $NdFe_2Si_2$ and it ordered in the collinear (+--+)-

type. The magnetic unit cells are doubled to the c direction with respect to the crystallographic structure. The same magnetic structure was reported for $NdFe_2Ge_2$ (69). Pinto et al. (70) also showed that the magnetic structure of $DyCo_2Si_2$ was the collinear (+-+-)-type, in which the magnetic unit cell was the same as the crystallographic structure. The same magnetic structures were reported for $PrCu_2Si_2$, $PrCu_2Ge_2$ (69), $TbCo_2Si_2$ (71), $HoCo_2Si_2$, $PrCo_2Si_2$, $NdCo_2Si_2$ (72) and $ThMn_2Si_2$ (73). In $DyCu_2Si_2$ (70) and $DyCu_2Ge_2$ (74), the magnetic unit cells are doubled to the a and c directions. The magnetic structure consists of ferromagnetic (101) plains of Dy, which are coupled antiferromagnetically with the adjacent layers. The magnetic moments of Dy in $DyCu_2Si_2$ lie along the b-axis. The magnetic moments of Dy in $DyCu_2Ge_2$ make an angle of 30 degrees with the a-axis and 70 degrees with the c-axis. $ThMn_2Si_2$ is antiferromagnetic with a Néel temperature of 483K (73). The magnetic structure consists of ferromagnetic layers perpendicular to the c-axis.

As mentioned above, transition metals except Mn had little magnetic moments in RM_2X_2. Magnetic parameters reported on RMn_2Si_2 were rather different among investigators. Thus, present author prepared RMn_2Si_2 (R=Y, Nd, Gd) and examined their magnetic properties. Also, $YMn_2(Si_{1-x}Ge_x)_2$ was prepared to examine the dependence of magnetic interaction between Mn spins on Mn-Mn interatomic distances and studied the effect of disordered R spins on the ordering of Mn spins. YNi_2Si_2 was prepared by using a cubic anvil-type high pressure apparatus (63,75) to examine the electron transfer from Si to Ni atoms.

1-3 Ternary rare-earth transition metal silicides RMSi (R: rare-earth metal, M: first-row transition metal)

There are a few reports on this ternary RMSi system. The RMSi compounds already reported are shown in Fig. 2. Indexes of a, b, c and d indicate the works done by the present author, Rieger et al., Bodak et al. and Mayer et al., respectively. Rieger et al. (76) prepared RCuSi using an arc melting method. Bodak et al (77) prepared RFeSi (R=La-Sm, Gd-Ho, Yb) and RCoSi (R=La-Sm) using the arc furnance. Mayer et al. (78) prepared PrNiSi and NdNiSi by an induction melting. The crystal structure of RCuSi was the hexagonal AlB_2-type, and that of RMSi (M=Fe and Co) was the tetragonal PbFCl-type. PrNiSi and NdNiSi had the tetragonal $ThSi_2$-type crystal structure.

Magnetic and electrical properties of RMSi compounds except RCuSi (R=Pr, Gd and Tb) have not been reported. According to Oesterreicher (56), RCuSi (R=Pr, Gd and Tb) were ferromagnetic with T_c=14K, 49K and 47K, respectively.

The RMSi compounds are the most simple compositional compounds in these ternary compounds, but crystallographic, magnetic and electrical data are very few. It is very interesting to study the change in crystal structure of the large rare-earth metal-transition metal silicides, and to study the crystallographic relation between PbFCl-type , $ThSi_2$-type and AlB_2-type structures and kinds of rare-earth elements and transition metals. And it is very interesting to examine the effect of 4f electrons

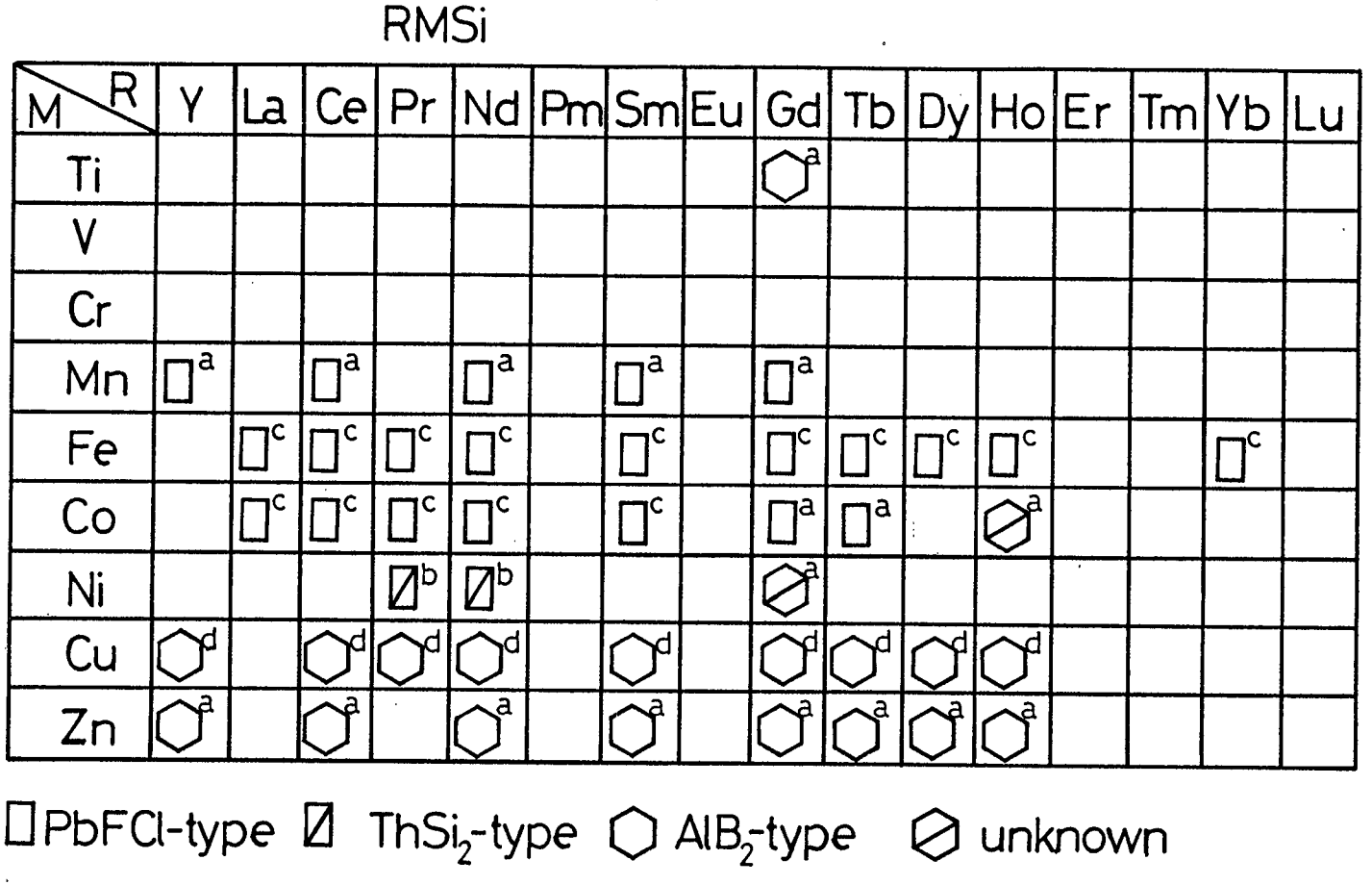

Fig. 2 Ternary rare-earth first-row transition metal silicides RMSi (R: rare-earth metal, M: first-row transition metal).

on magnetic and electrical properties of the ternary rare-earth transition metal silicides. The most important feature of 4f electrons, which is different from 3d electrons, is to localize inside the $(5s)^2(5p)^6$ closed shell. From this fact, it is expected that 4f electrons contribute mainly to the magnetic properties and secondary to the electric conduction.

Therfore, in the present studies, ternary rare-earth first-row transition metal silicides were prepared and their crystal structures were determined, and then magnetic and electrical properties of these compounds were investigated.

The crystal structures of RMSi (R: rare-earth metal, M: first-row transition metal) were mainly divided into two groups depending on the kinds of transition metal elements. One was the tetragonal PbFCl-type (space group: P4/nmm) for M=Mn, Fe and Co (77,79). Another was the hexagonal AlB_2-type structure (space group: P6/mmm) for M=Ti, Cu and Zn (56,76,80,81). PrNiSi and NdNiSi had the tetragonal $ThSi_2$-type structure. The crystal structures of HoCoSi and GdNiSi were hexagonal, but were not be related to known structures. The crystallographycal relation between these crystal structures will be discussed in 4-1.

The preparation and magnetic properties of GdTiSi are introduced in 3-1. The preparation and magnetic and electrical properties of RMSi (M=Mn, Co) with the PbFCl-type structure are presented in 3-2, 3-3, and discussed in 4-2.

The preparation and magnetic and electrical properties of NdNiSi are introduced in 3-4.

The preparation and magnetic and electrical properties of RCuSi and RZnSi are presented in 3-5 and 3-6. The paramagnetic Curie temperature of RZnSi was higher than that for RCuSi, but the temperature gradients of electrical resistivities $d\rho/dT$ for RZnSi were smaller than those for RCuSi. To examine these differences in magnetic and electrical properties between RZnSi and RCuSi, solid solutions $RCu_{1-x}Zn_xSi$ (R=Gd, Dy and Ho) were prepared and their magnetic and electrical properties were investigated as mentioned in 3-7, 3-8 and 3-9. The magnetic and electrical properties will be discussed in 4-3 on the basis of the RKKY (Ruderman-Kittel-Kasuya-Yosida) theory. This theory deals with the magnetic interaction between localized magnetic moments through the conduction electrons. The magnitude of the magnetic interaction is in proportion to the product of de Genne function and lattice sum of Ruderman functions.

The preparation and magnetic and electrical properties of RMn_2Si_2 (R=Y, Nd, Gd) and YNi_2Si_2 are presented in 3-10 and discussed in 4-4.

To make the magnetism of RMn_2Si_2 more clear and examine the effects of disordered R spins on the ordering of Mn spins, the $YMn_2(Si_{1-x}Ge_x)_2$ compounds were prepared and their magnetic properties were studied as described in 3-11.

The thermoelectric power of RZnSi is discussed in 4-5.

CHAPTER 2

EXPERIMENTAL PROCEDURE

2-1 Starting materials

Rare-earth metals (purity 99.9%), Ti (99%), Mn (99.9%), Co (99.99%), Ni (99.99%), Cu (99.7%), Zn (99.99%), Si (99.99%) and Ge (99.99%) were used as the starting materials. Rare-earth metals in ingot form were filed in the glove box which was filled with an argon gas, and mixed with other powders of transition metals and metalloid elements. The mixed powders were formed into the pellet form under 10 MPa at room temperature.

2-2 Methods of synthesis

2-2-1 Synthesis using an evacuated silica tube

The pellet obtained in the above mentioned way was sealed in an evacuated silica tube. The pressure in the silica tube was less than 10^{-3} Torr. Then, it was heated at 800-1000 °C for 7-10 days. The samples containing manganese, cobalt and nikel elements were set in the BN cells to prevent the reaction between samples and silica tubes. The heating temperature was determined by considering the reactivity of samples, which was examined using X-ray powder diffractometry. The volatilization of SiO from a silica glass is caused by the following equation (82),

$$2SiO_2\ (s)=2SiO\ (g)+O_2\ (g). \qquad (1)$$

At 900 °C, the equilibrium constant is

$$K=\frac{p_{SiO}^2 \cdot p_{O_2}}{a_{SiO_2}^2}=10^{-42} \quad (2)$$

where p_{SiO} and p_{O_2} are the partial pressure of SiO and O_2 gases. The a_{SiO_2} is the activity of SiO_2 solid. Under reducing conditions, the above reaction become rapid (83).

This preparation method is quite simple and it is easy to protect the oxidation of sample. Thus, this method was mainly used to prepare the ternary rare-earth transition metal silicides.

2-2-2 Synthesis using high pressure apparatus

The cubic anvil-type high pressure apparatus (75) was used. The sample was put into a BN cell, which was inserted in a graphite heater. Then, the high pressure cell assembly was set in a pyropylite cube. The temperature of samples was measured by a Pt-Rh13% thermocouple. The pressure was calibrated by using the pressure-induced phase transition of Bi.

This preparation method is applied to the high temperature synthesis above 1100 C under reducing conditions and it is available to synthesize the samples containing the elements with relatively large vaper pressure.

2-2-3 Synthesis using an induction furnance

The sample with the pellet form was wrapt by the tantalum foil and set into the BN crucible, and then inserted in the graphite heater. The samples were heated under the Ar gas atmosphere of 10-15 MPa. The temperature was measured by using W-Re thermocouple.

2-3 Identification of products

Powdered samples were examined by means of X-ray powder diffractometry using Mn-filtered FeKα or Ni-filtered CuKα radiation. Lattice constants were determined by using silicon as an internal standard.

2-4 Measurements of magnetic properties

Magnetic measurements were performed by a torsion balance magnetometer in the temperature range from 77K to 700K in the magnetic fields up to 13 kOe. The change in temperature of samples was performed by dipping the protecting quartz tube in the Dewar flask filled with the liquid nitrogen, or heating the Pt resistance coil around the quartz tube. The temperature was measured by using the AuCo-Cu or Cromel-Constantan thermocouple. Magnetization and magnetic susceptibility were calculated using Ni and Mn-Tutton's salt as the standard materials.

2-5 Measurements of electrical resistivity

The electrical resistivity was measured by a four probe method in the temperature range from 77K to 300K. The temperature of samples was measured by using a Cromel-Constantan thermocouple. The sample-holder assembly was placed in a quartz tube which could be evacuated and back-filled with a helium gas to avoid the condensation of water vapor at low temperature and to transmit the heat. The temperature was changed by dipping the quartz tube into a Dewar flask filled with a liquid nitrogen.

2-6 Measurements of thermoelectric power

The thermoelectric power was measured in the temperature range from 77K to 300K. The schematic diagram of an apparatus is shown in Fig. 3. The powder of sample was filled in the quartz tube (3 mm in diameter and 3 cm in height) and sintered at 900 ℃. The Cu-Constantan thermocouples were placed at both ends of the sample. These thermocouples served as electrodes for thermoelectric power measurements as well as to measure the temperature of sample. The exchange of gas and change in temperature of samples were achieved in the same way in the case for measurements of electrical resistivity.

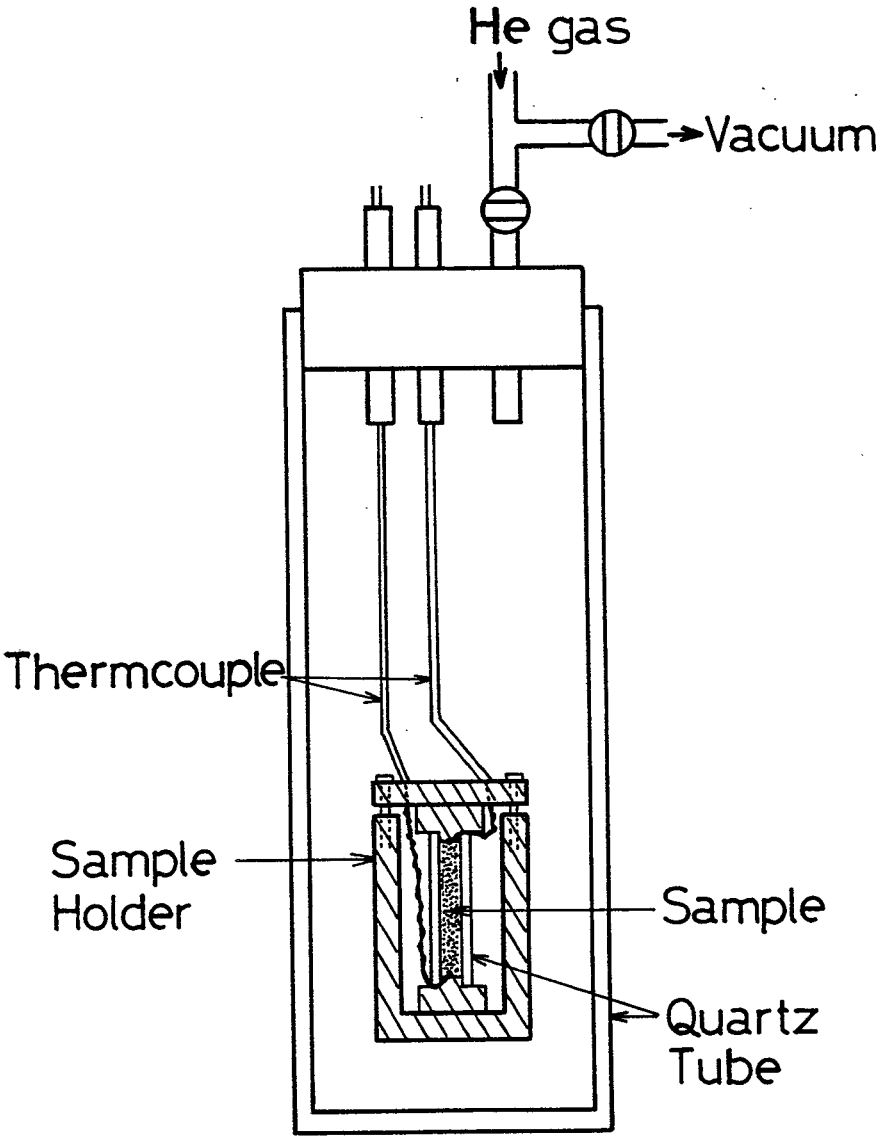

Fig. 3 Schematic diagram of apparatus for measurement of thermoelectric power.

CHAPTER 3

EXPERIMENTAL RESULTS

3-1 Preparation and magnetic properties of GdTiSi

GdTiSi was prepared by heating the starting materials at 1700 °C for 40 min in an induction furnance under an argon atmosphere.

The X-ray powder diffraction pattern of GdTiSi was completely indexed on the basis of the hexagonal AlB_2-type crystal structure (space group P6/mmm). The Gd atoms occupy the (1a) sites, and Ti and Si atoms occupy the (2d) sites. The crystal structure of the RMSi compounds with the hexagonal AlB_2-type is shown in Fig. 4. Lattice constants of GdTiSi were a=0.3877 nm and c=0.4170 nm.

The temperature dependence of the inverse magnetic susceptibility, χ^{-1}, is shown in Fig. 5. The GdTiSi compound was paramagnetic above 77 K and χ^{-1}-T relation obeyed the Curie-Weiss law. The effective magnetic moment, μ_{eff}, and the paramagnetic Curie temperature, θ_a, were 7.1 μ_B and 10 K, respectively. The value of μ_{eff} was in good agreement with the calculated value for Gd^{3+} ion. This fact indicated that magnetic properties of GdTiSi was due to the Gd^{3+} spins.

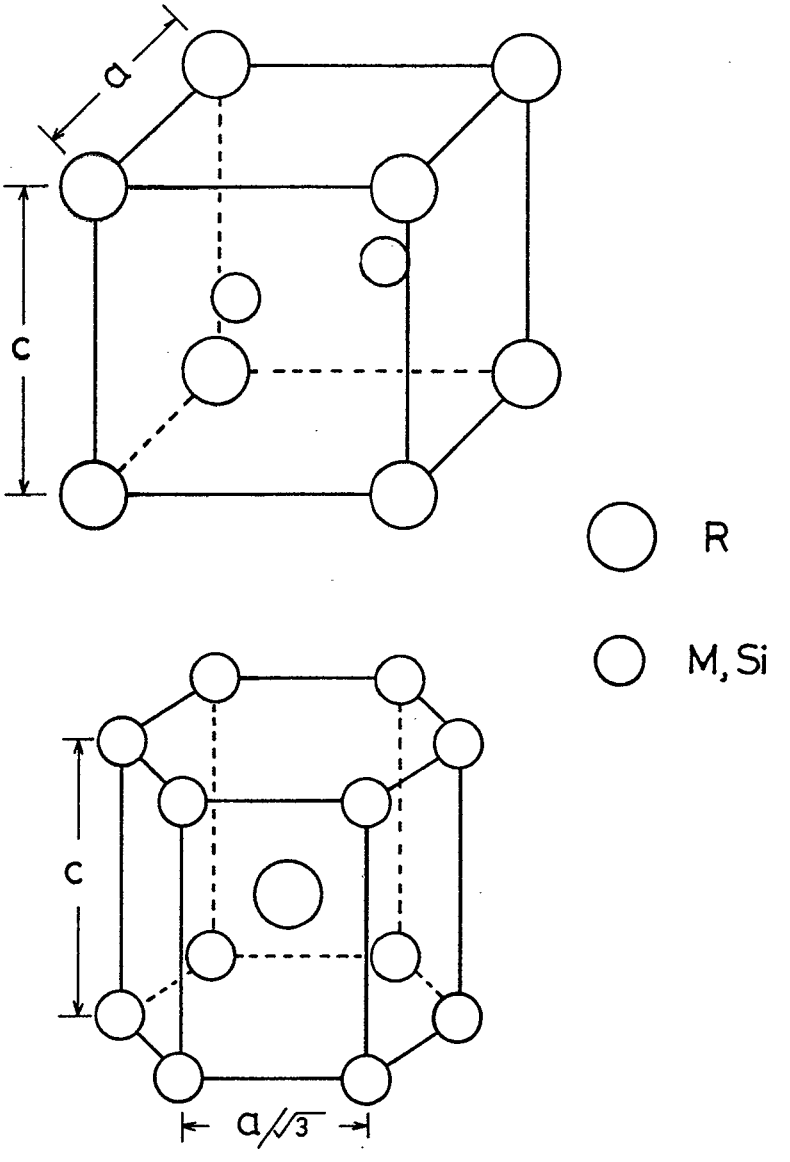

Fig. 4 Crystal structure of RMSi with the hexagonal AlB_2-type.

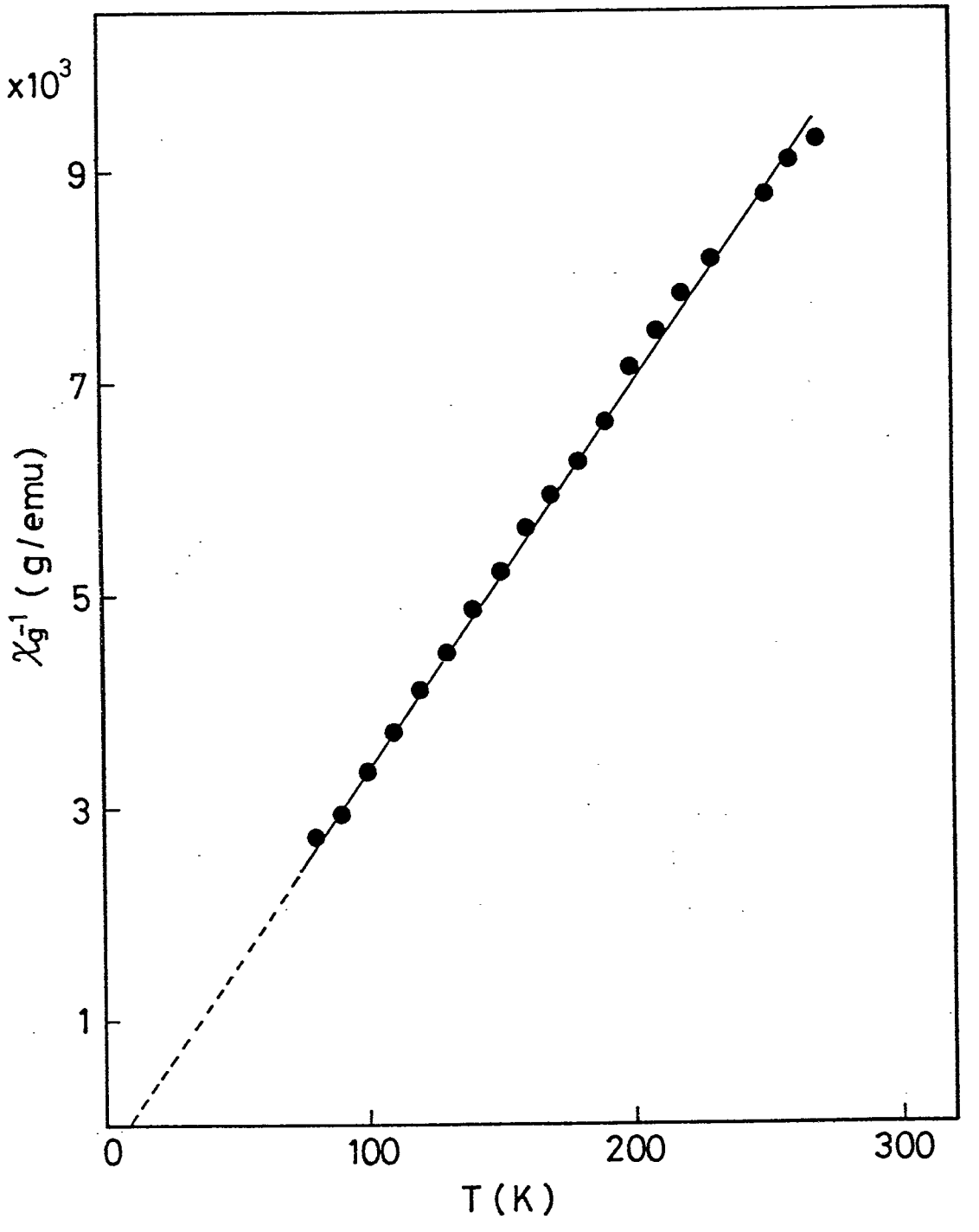

Fig. 5 Temperature dependence of inverse magnetic susceptibility of GdTiSi.

3-2 Preparation and magnetic and electrical properties of RMnSi (R=Y, Ce, Nd, Sm, Gd)

YMnSi and GdMnSi were prepared by heating the starting materials at 1.0 GPa and 1300 ℃ for 1 hr (79,84). The other RMnSi compounds were prepared by heating the starting materials in the evacuated silica tubes at 900 ℃ for 7 days.

The X-ray powder diffraction patterns of these compounds were completely indexed on the basis of the tetragonal PbFCl-type structure (space group P4/nmm). The crystal structure of the RMSi compounds with the PbFCl-type is shown in Fig. 6. The large open circles, small open circles and and closed circles indicate the R, M and Si atoms, respectively. The R and Si atoms occupy the (2c) sites, and M atoms occupy the (2a) sites. The lattice constants, c/a and unit cell volumes of the RMnSi compounds are shown in Fig. 7 and listed in Table 3. Lattice constants linearly decreased with increasing the atomic number of rare-earth elements. This fact was due to the lanthanide contraction and showed that the rare-earth ions had the trivalent state.

The interatomic distances of RMnSi (R=Y, Ce, Nd, Sm and Gd) were obtained by using z-parameters of 0.672 for R and 0.175 for Si (77). The results are shown in Table 4. The values in the parenthesis indicate the comparison with the sum of corresponding atomic radii (85). From Table 4, it was found that the Mn-Si interatomic distances were rather smaller than the sum of corresponding atomic radii.

The temperature dependences of magnetic susceptibilities, χ, for NdMnSi and SmMnSi are shown in Fig. 8. NdMnSi and

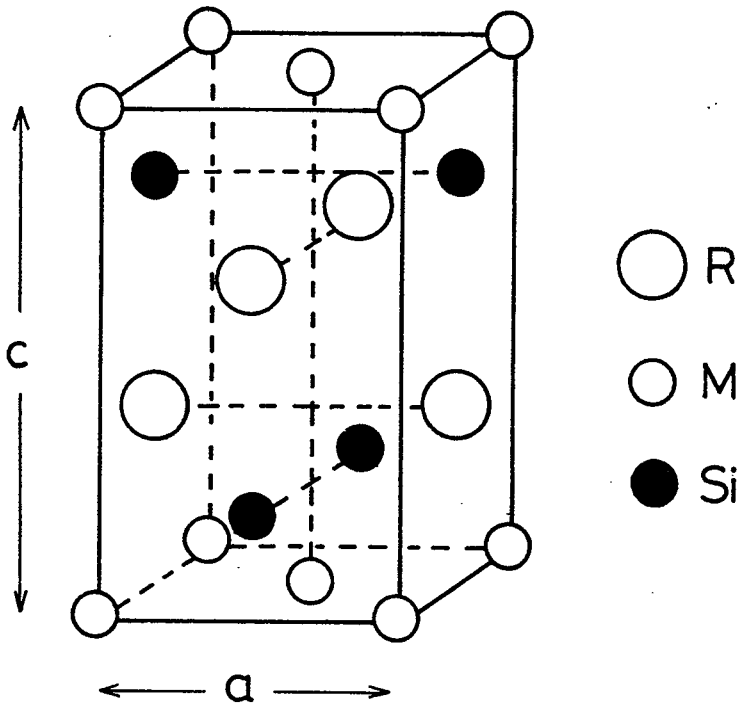

Fig. 6 Crystal structure of RMSi with the tetragonal PbFCl-type.

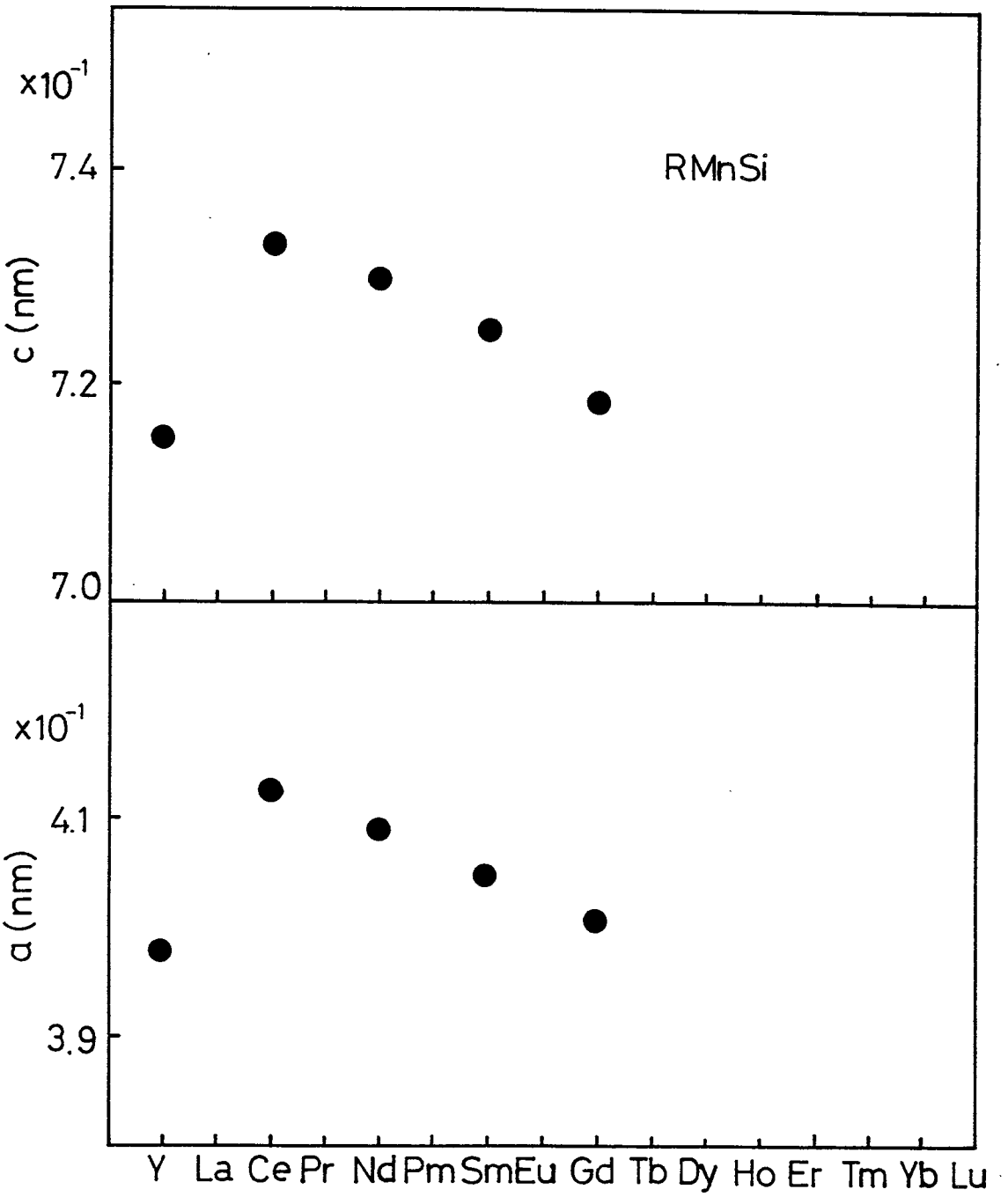

Fig. 7 Lattice parameters of RMnSi compounds.

Table 3 Lattice parameters of RMnSi compounds

RMnSi	a (10^{-1}nm)	c (10^{-1}nm)	c/a	V ($10^{-3}nm^3$)
YMnSi	3.978	7.152	1.798	113.2
CeMnSi	4.124	7.329	1.777	124.6
NdMnSi	4.092	7.300	1.784	122.2
SmMnSi	4.047	7.255	1.793	118.8
GdMnSi	4.009	7.183	1.792	115.4

Table 4 Interatomic distances of RMnSi compounds

RMnSi	Interatomic distances (10^{-1}nm)						
	4R-R	4R-R	4R-Mn	4R-Si	2R-Si	Mn-Mn	Mn-Si
YMnSi	3.978 (10.5)	3.737 (3.81)	3.076 (-1.10)	3.018 (-3.26)	3.555 (13.9)	2.813 (7.36)	2.350 (-10.6)
CeMnSi	4.124 (13.3)	3.855 (5.90)	3.167 (1.19)	3.124 (-0.50)	3.643 (16.0)	2.920 (11.5)	2.428 (-7.67)
NdMnSi	4.092 (12.4)	3.831 (5.25)	3.149 (0.62)	3.101 (-1.23)	3.628 (15.5)	2.893 (10.4)	2.412 (-8.29)
SmMnSi	4.047 (9.38)	3.797 (2.62)	3.124 (-1.15)	3.070 (-3.17)	3.606 (13.7)	2.862 (9.23)	2.389 (-9.17)
GdMnSi	4.009 (11.4)	3.761 (4.50)	3.093 (-0.50)	3.040 (-2.60)	3.600 (15.4)	2.835 (8.20)	2.366 (-10.3)

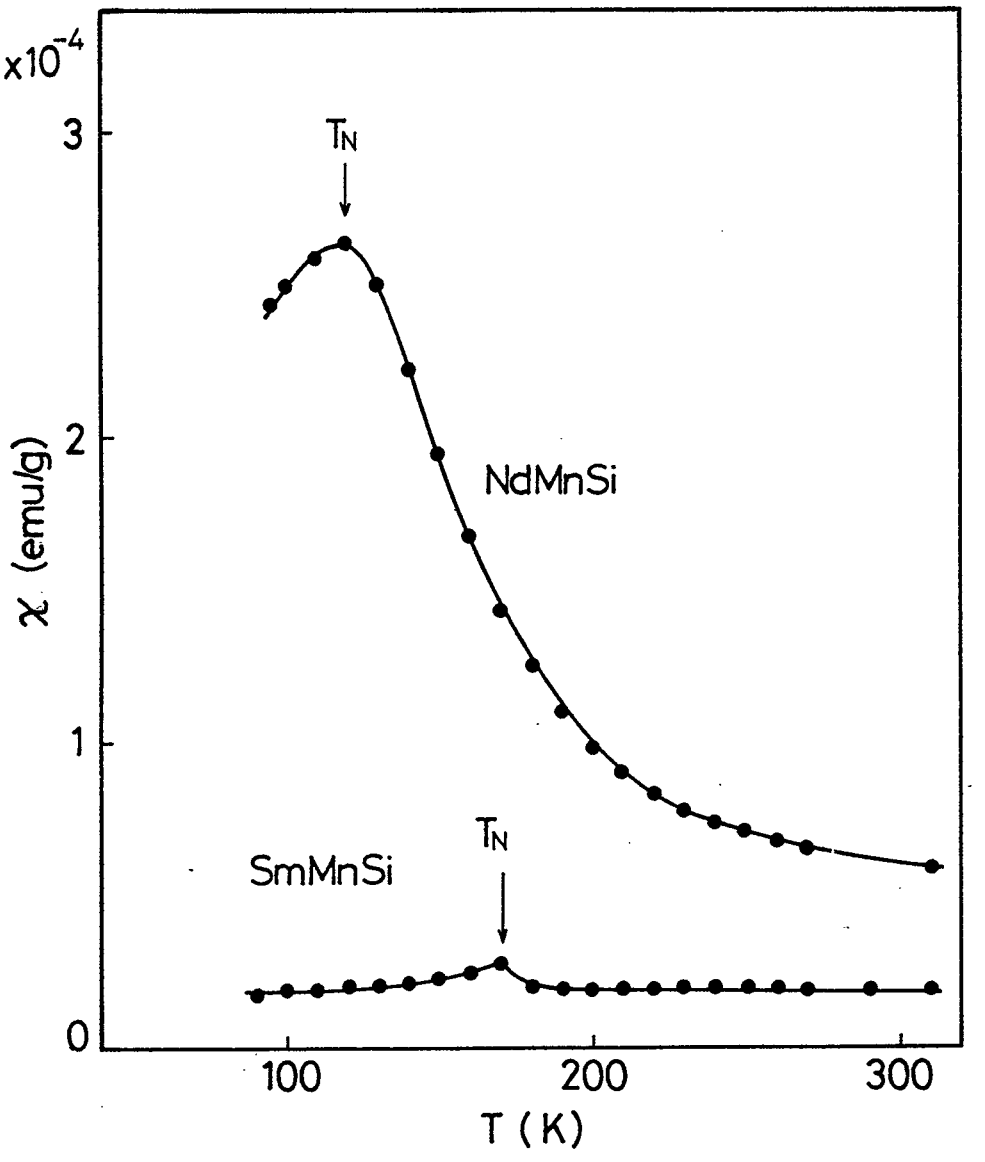

Fig. 8 Temperature dependence of magnetic susceptibility of NdMnSi and SmMnSi.

SmMnSi were antiferromagnetic with T_N=120K and 172K, respectively. The temperature dependences of χ^{-1} in the paramagnetic region obeyed the Curie-Weiss law. The effective magnetic moments, μ_{eff}, and paramagnetic Curie temperature, θ_a, of NdMnSi were 5.3 μ_B and 150K, respectively.

The temperature dependence of magnetizations, σ, of GdMnSi is shown in Fig. 9. The σ versus magnetic fields, H, at 77K are plotted in Fig. 9. GdMnSi was ferromagnetic with T_C=320K. The ferromagnetic moment of GdMnSi was n_f=5.2 μ_B at 77K.

The temperature dependences of σ and χ^{-1} of YMnSi are shown in Fig. 11. The magnetic field dependence of σ is shown in Fig. 12. As seen in Fig. 12 showing the results of σ-H curve, the magnetization above 190K was saturated, but below 170K the magnetization increased with increasing the applied magnetic field and no saturation was observed up to 13 kOe. As seen in Fig. 11, it is considered that YMnSi is metamagnetic. The Mn spins may gradually change the alignment from the antiferromagnetic ordering to the ferromagnetic ordering when H is increased. The ferromagnetic moment of YMnSi at 190K was 1.3 μ_B. The values of n_f per Mn atom of $LaMn_2Si_2$ (67) and $LaMn_2Ge_2$ (61) were 1.54 μ_B and 1.5 μ_B, respectively. The Mn spins in $ThMn_2Si_2$ were collinear and the magnetic moment was 1.75 μ_B per Mn atom (73). Therefore, the value of n_f=1.3 μ_B of YMnSi is due to the almost parallel alignment of Mn spins.

The abrupt increase in σ at about 100 K may be due to the magnetic phase transition from the antiferromagnetic phase to

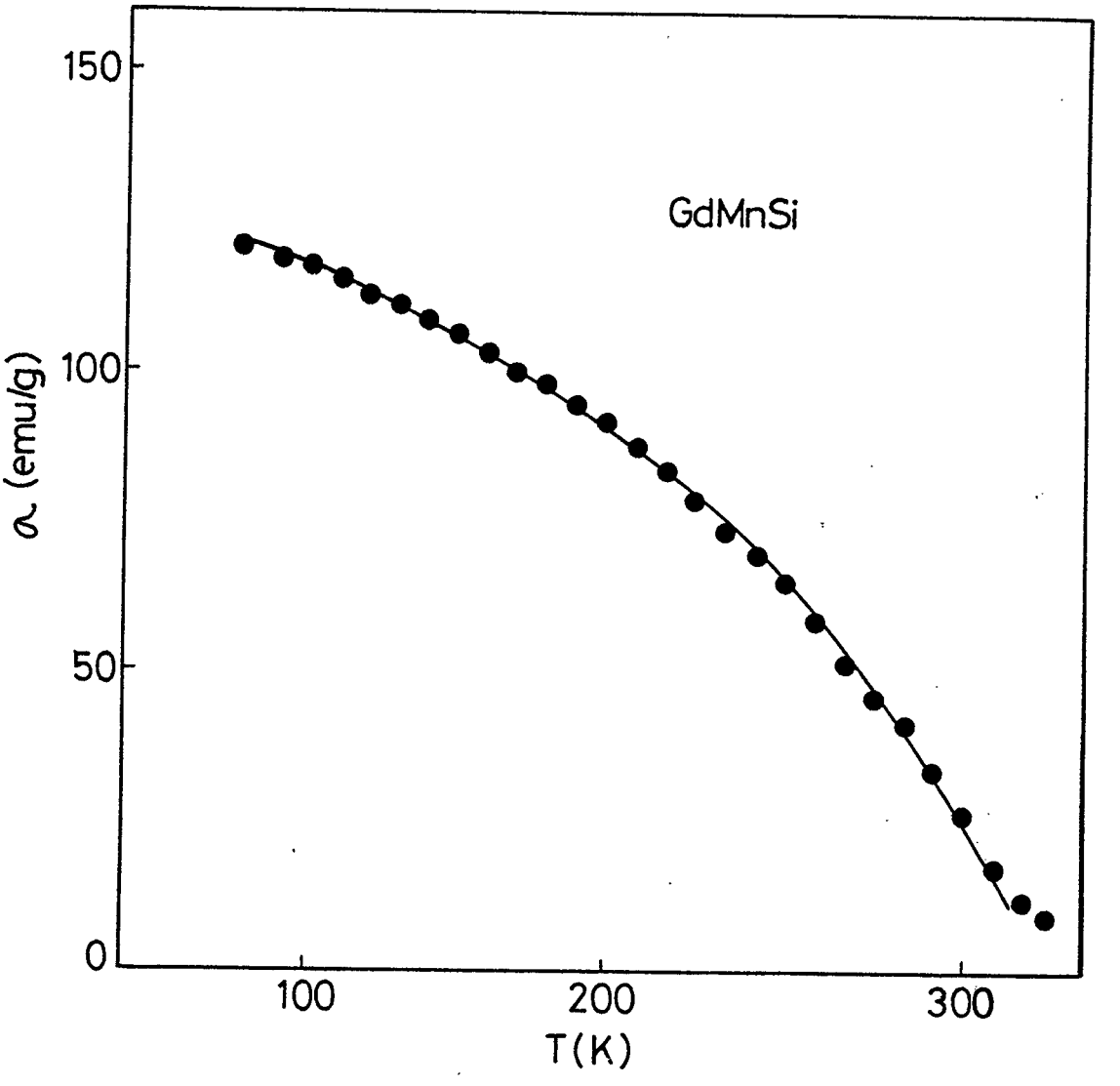

Fig. 9 Temperature dependence of magnetization of GdMnSi.

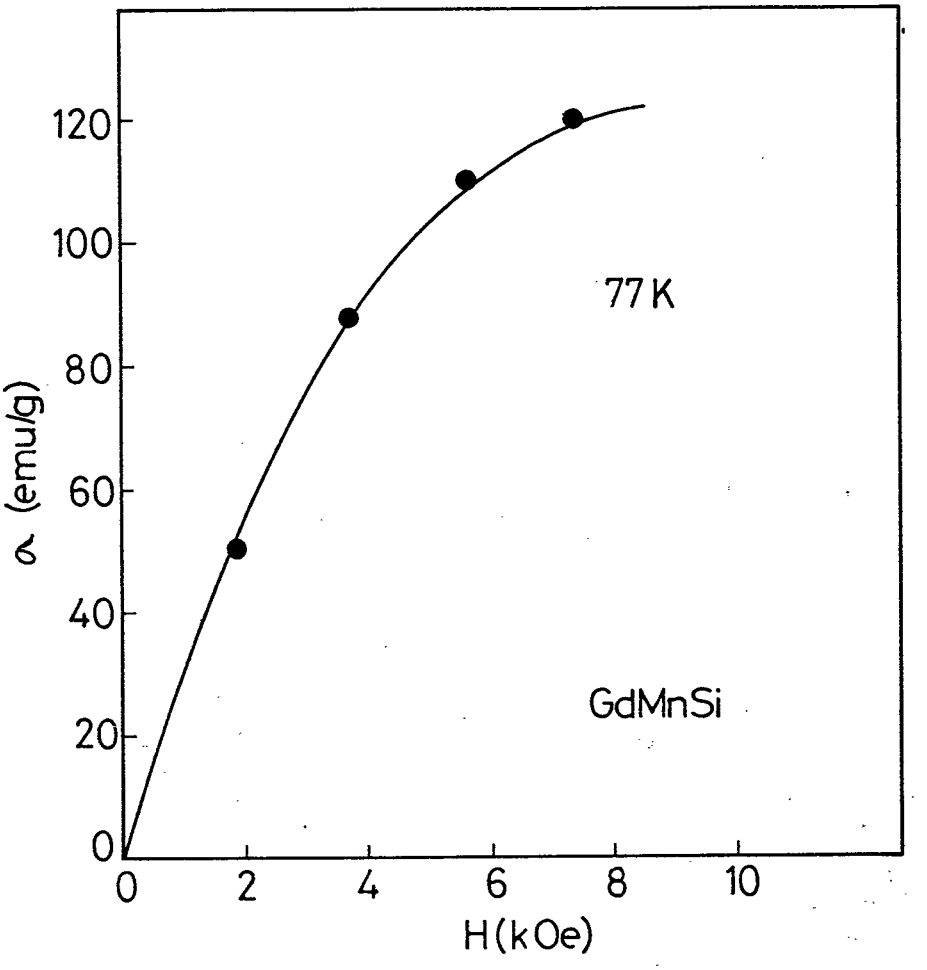

Fig. 10 Magnetization versus magnetic field for GdMnSi.

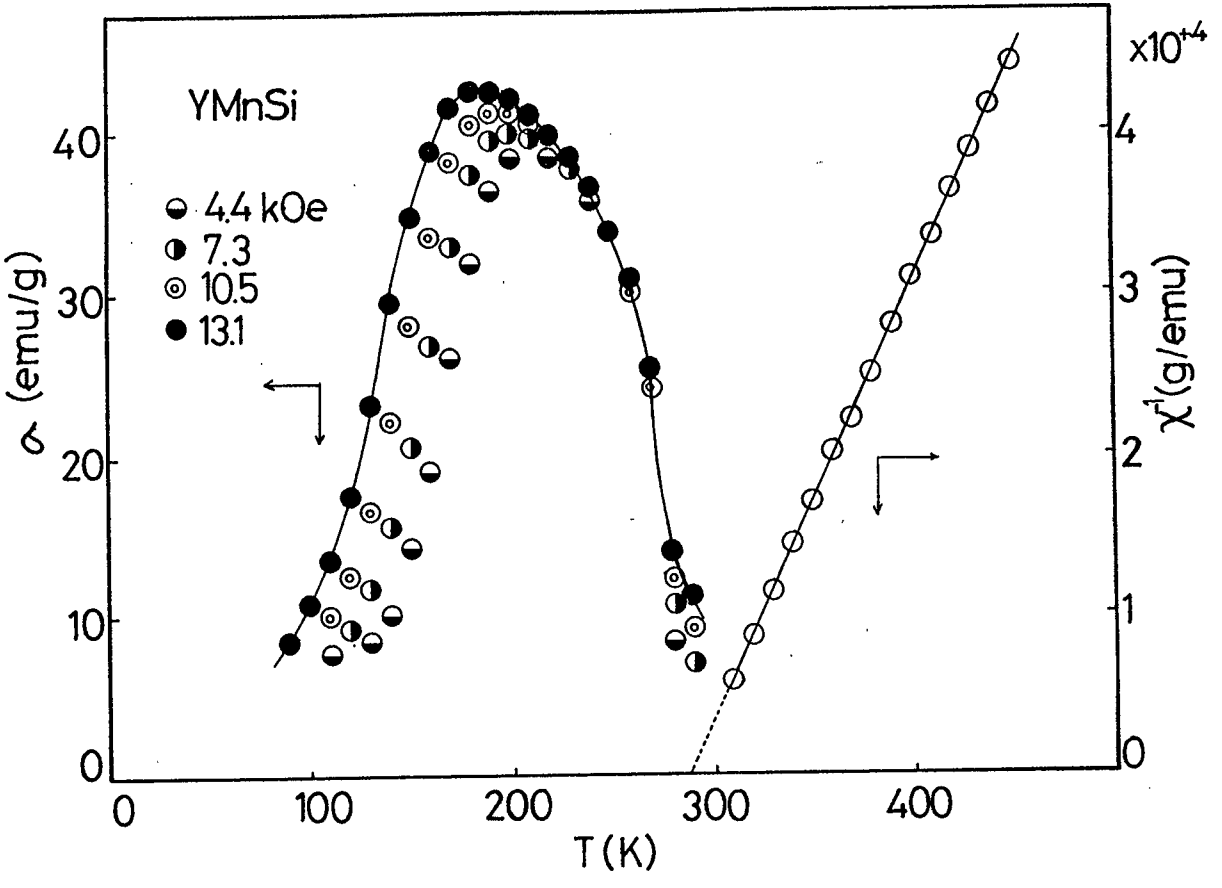

Fig. 11 Temperature dependences of magnetization and inverse magnetic susceptibility of YMnSi.

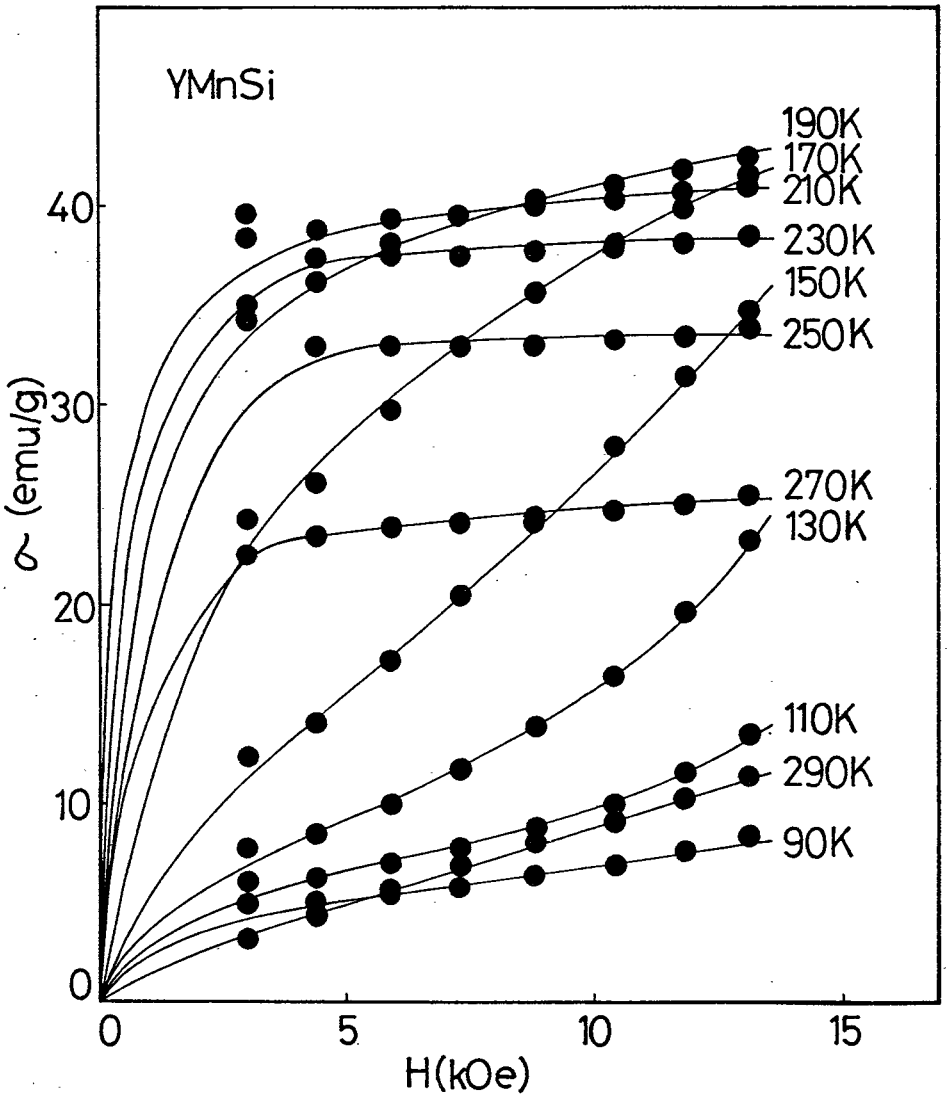

Fig. 12 Magnetization versus magnetic field for YMnSi.

the ferromagnetic phase. From the σ^2 versus T curve, the Curie temperature was determined to be 282 K. The similar results were reported for the $La_{0.8}Y_{0.2}Mn_2Si_2$ (66) and CoMnSi (31,32).

The temperature dependence of χ^{-1} for YMnSi in the paramagnetic region obeyed the Curie-Weiss law. The μ_{eff} and θ_a were 2.3 μ_B and 280 K, respectively.

The magnitude of the effective magnetic moments for RMnSi indicated that the magnetic moment per Mn atom was about 2.0 μ_B, which well agreed with the values of the Mn atom in the related compounds of RMn_2X_2 (R=Y, La; X=Si, Ge) (61-67).

The values of T_C or T_N of RMnSi are plotted as a function of the Mn-Mn interatomic distances in Fig. 13. The $D_{Mn-Mn}(a)$ and $D_{Mn-Mn}(c)$ denote the intralayer and interlayer Mn-Mn interatomic layers, respectively. The values of T_N or T_C decreased with increasing Mn-Mn distances. The change in magnetic properties from antifettomagnetism to ferromagnetism was found in the critical Mn-Mn interatomic distances.

The temperature dependences of electrical resistivities of NdMnSi and SmMnSi are shown in Fig. 14. The electrical resistivities of these compounds increased with increasing temperature. The change in slope of ρ -T curve is observed for both compounds. This fact may be due to the magnetic phase transition.

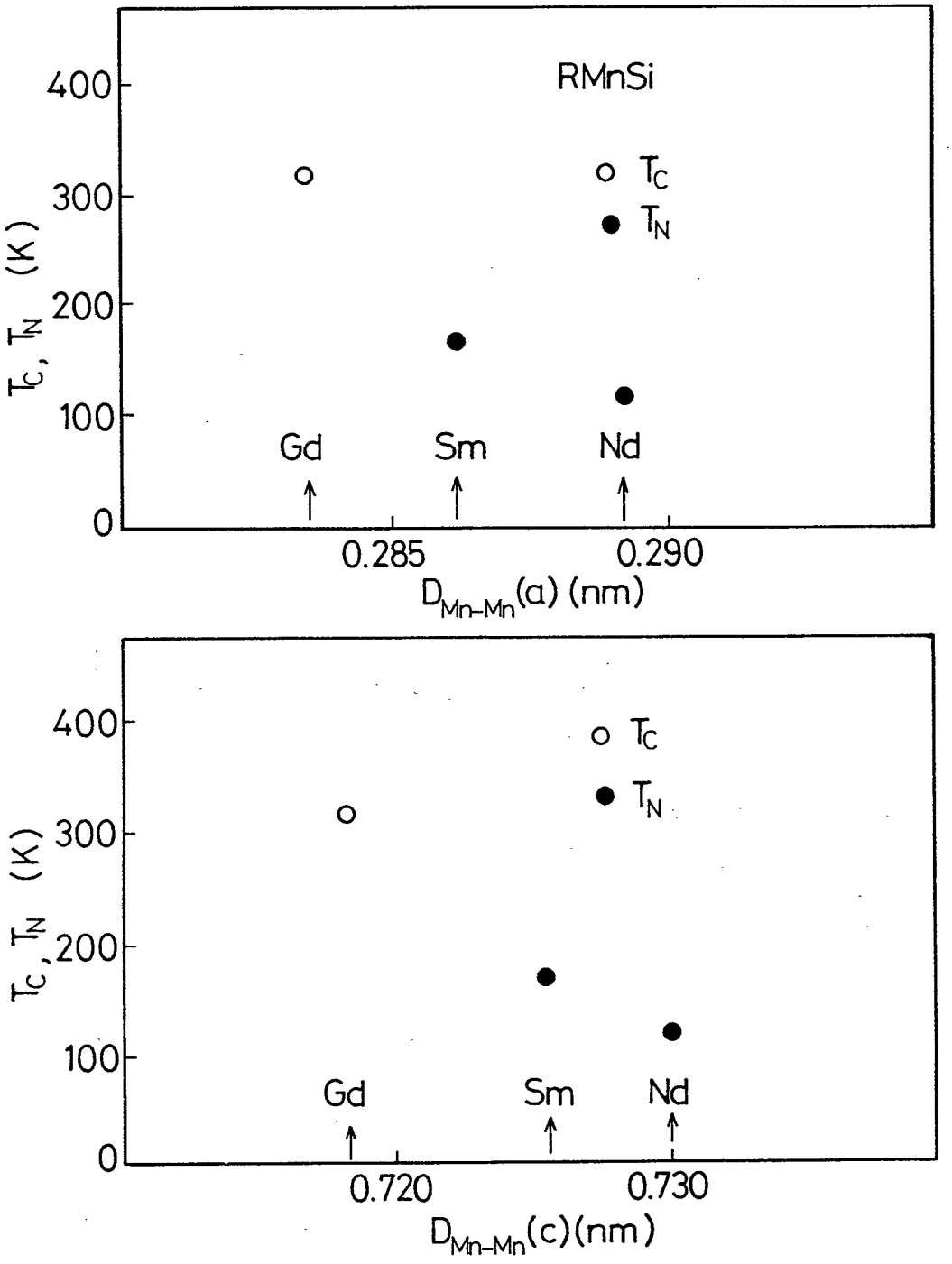

Fig. 13 Dependence of T_C or T_N of RMnSi on interatomic Mn-Mn distances.

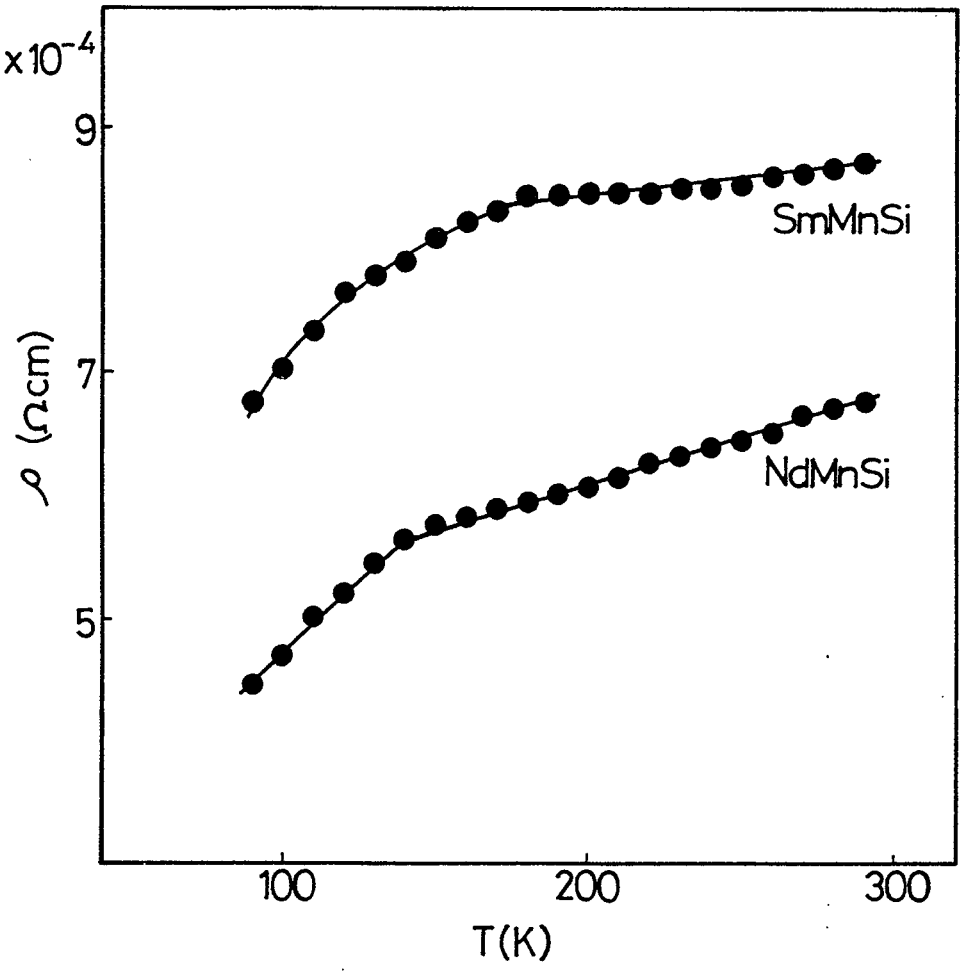

Fig. 14 Temperature dependence of electrical resistivity of NdMnSi and SmMnSi.

3-3 Preparation and magnetic and electrical properties of RCoSi (R=Nd, Gd, Tb, Ho)

RCoSi (R=Nd, Gd, Tb, and Ho) were prepared by heating the starting materials at 900°C for 7 days in the evacuated silica tubes. The crystal structure of RCoSi (R=Nd, Gd, Tb) was the tetragonal PbFCl-type. The lattice constants, c/a and unit cell volumes are listed in Table 5. The lattice parameters are plotted against the rare-earth elements together with the results by Bodak et al.(77) in Fig. 15. The lattice constants decreased with increasing atomic number of rare-earth element.

The interatomic distances of RCoSi (R=Nd, Gd, Tb) are shown in Table 6. It was found that Mn-Si interatomic distances were much smaller than the sum of corresponding atomic radii. This fact suggests that electron transfer occurs from Si to Co.

The crystal structure of HoCoSi was unknown. The X-ray powder diffraction pattern of HoCoSi could be indexed on the basis of the hexagonal structure with a=0.8222 nm and c=0.6802 nm, but was not related with the crystal structures which were known for silicides.

The temperature dependence of ρ and χ^{-1} for GdCoSi is shown in Fig. 16. GdCoSi was ferromagnetic with T_c=250 K. The magnetization did not saturate, as seen in Fig. 17. The increase in σ below 50 K was probably due to the ordering of Gd^{3+} spins. The χ^{-1}-T relation in the paramagnetic region obeyed the Curie-Weiss law. The effective magnetic moment and paramagnetic Curie temperature were 8.7 μ_B and 131 K, respectively.

The smaller values of magnetizations of GdCoSi than the value of GdMnSi is caused by the electron transfer from Si to

Table 5 Lattice parameters of RCoSi compounds

RCoSi	a (10^{-1}nm)	c (10^{-1}nm)	c/a	V (10^{-3}nm^3)
NdCoSi	4.026	6.935	1.723	112.4
GdCoSi	3.975	6.746	1.697	106.6
TbCoSi	3.957	6.714	1.697	105.1

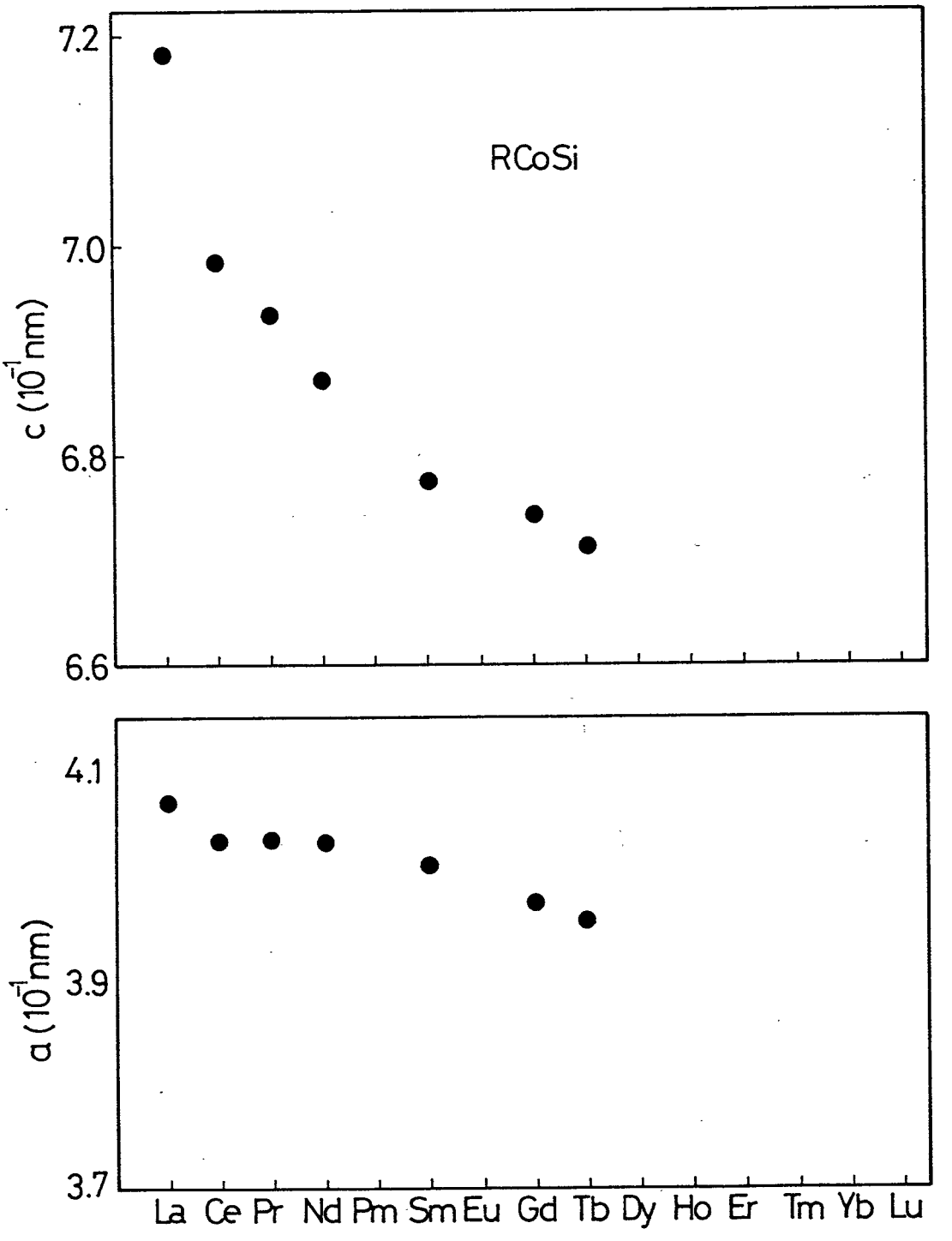

Fig. 15 Lattice constants of RCoSi compounds. Values for RCoSi (R=La, Ce, Pr and Sm) are quoted from Ref. 77.

Table 6 Interatomic distances of RCoSi compounds

RCoSi	Interatomic distances (10^{-1}nm)						
	4R-R	4R-R	4R-Co	4R-Si	2R-Si	Co-Co	Co-Si
NdCoSi	4.026 (10.6)	3.714 (2.04)	3.037 (-1.06)	3.038 (-3.25)	3.447 (9.77)	2.847 (13.9)	2.351 (-8.54)
GdCoSi	3.975 (10.4)	3.645 (1.25)	2.974 (-2.48)	2.994 (-4.03)	3.353 (7.46)	2.811 (12.4)	2.312 (-10.1)
TbCoSi	3.957 (11.8)	3.628 (2.49)	2.960 (-1.97)	2.981 (-3.54)	3.337 (7.99)	2.798 (11.9)	2.301 (-10.5)

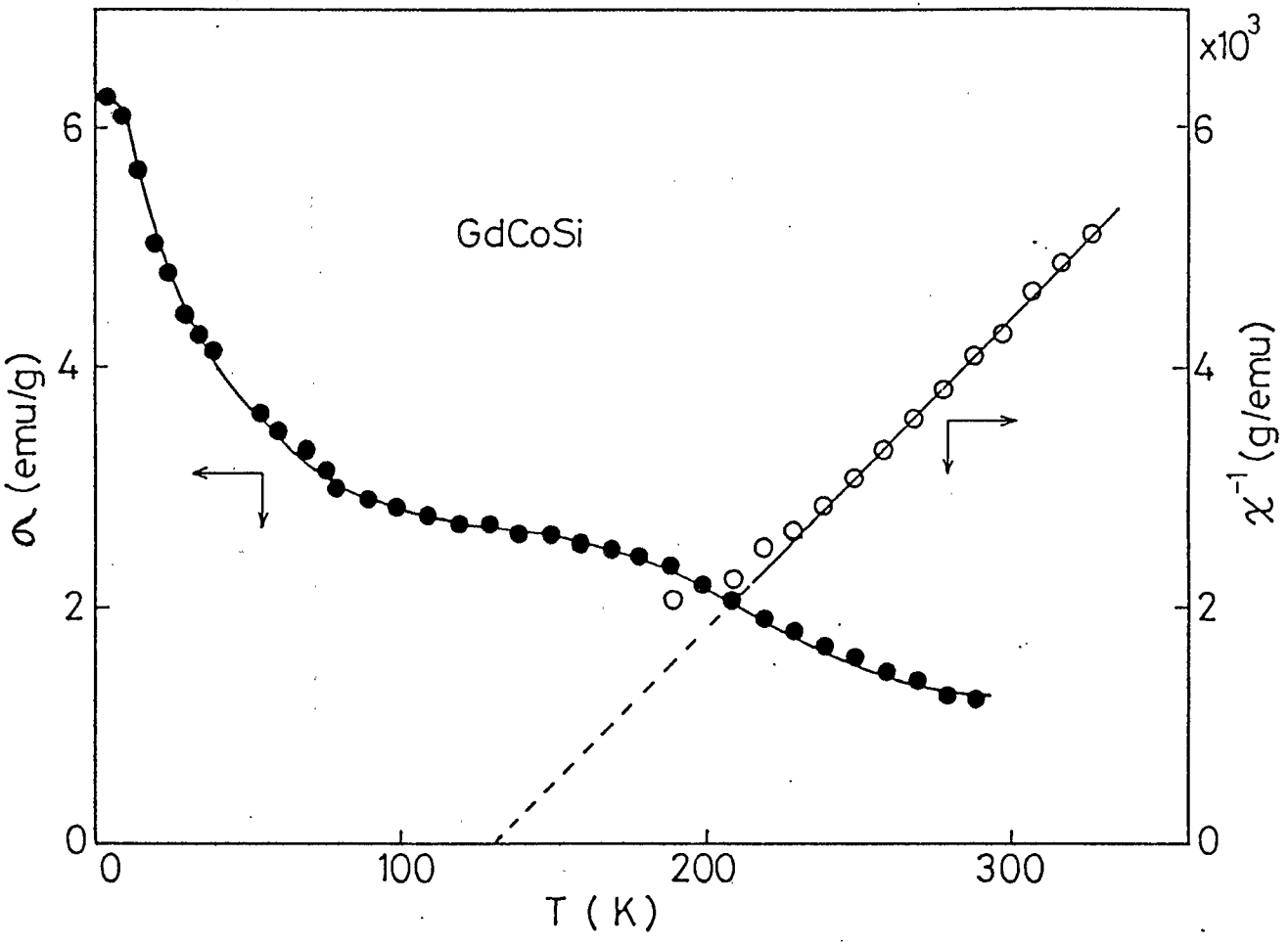

Fig. 16 Temperature dependences of magnetization and magnetic susceptibility of GdCoSi.

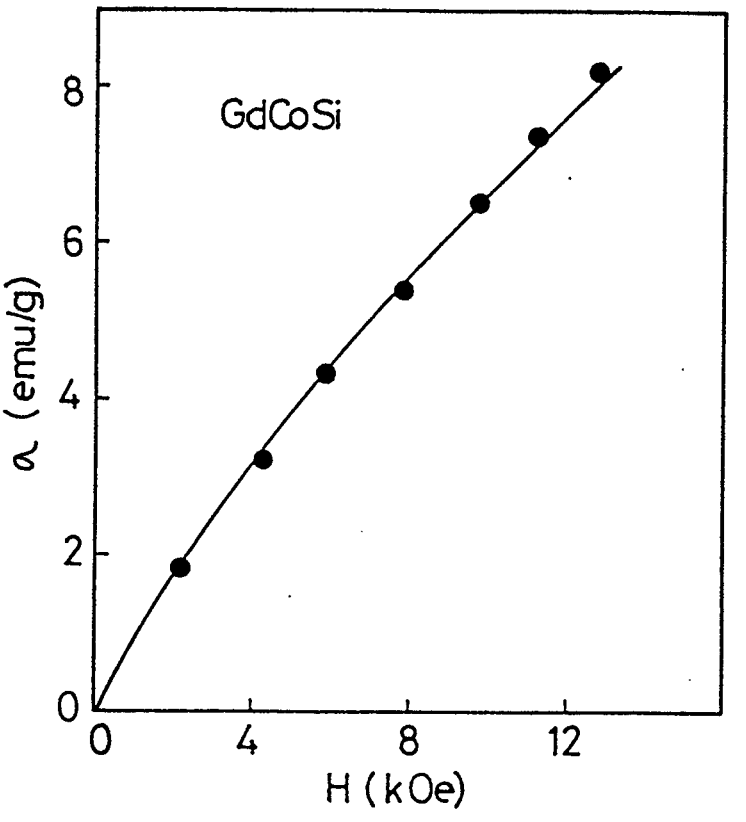

Fig. 17 Magnetization versus magnetic field for GdCoSi.

transition metal atoms, which shifts the Slater-Pauling curve to the lower electron number side.

The temperature dependence of the electrical resistivity of GdCoSi is shown in Fig. 18. The values of electrical resistivity ρ had the magnitude of 10^{-3} Ωcm and increased with increasing temperature. The change in $d\rho/dT$ was corresponded to the magnetic phase transition from the ferromagnetic phase to paramagnetic phase.

The temperature dependences of χ and χ^{-1} for NdCoSi are shown in Fig. 19. NdCoSi was paramagnetic above 77K. The effective magnetic moment and paramagnetic Curie temperature were 3.2 μ_B and 32K, respectively.

The temperature dependences of χ and χ^{-1} for TbCoSi are shown in Fig. 20. TbCoSi was antiferromagnetic with T_N=128K. In the paramagnetic region, χ^{-1}-T relation obeyed the Curie-Weiss law. The effective magnetic moment and paramagnetic Curie temperature were 9.1 μ_B and 108K, respectively.

The temperature dependences of σ and χ^{-1} for HoCoSi are shown in Fig. 21 together with the σ-H curve at 77K. HoCoSi showed the ferromagnetic behavior, but σ did not saturate at 13 kOe. From σ^2 versus T plot, T_c was obtained to be 158K. In the paramagnetic region, χ^{-1}-T relation obeyed the Curie-Weiss law. The effective magnetic moment and paramagnetic Curie temperature were 9.5 μ_B and 44K, re-respectively.

The values of effective magnetic moment of RCoSi, except GdCoSi, were almost in agreement with the calculated values for R^{3+} ions. From this results, it was expected that Co atoms.

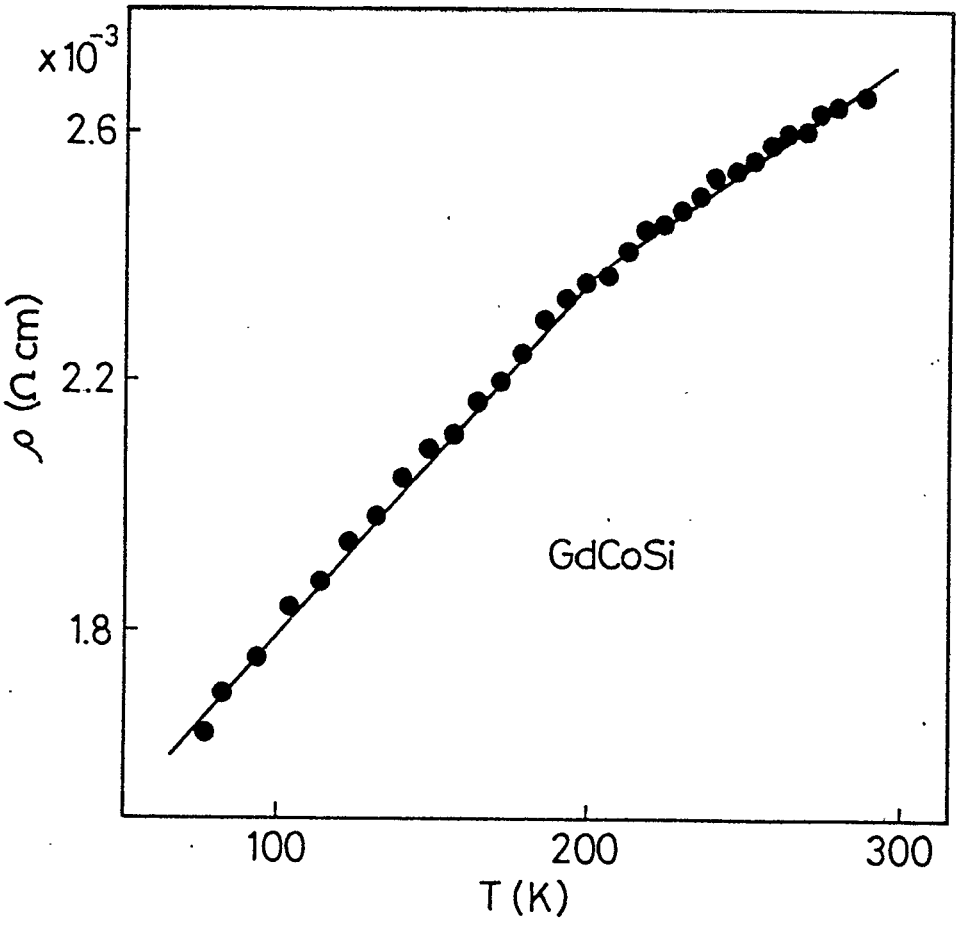

Fig. 18 Temperature dependence of electrical resistivity of GdCoSi.

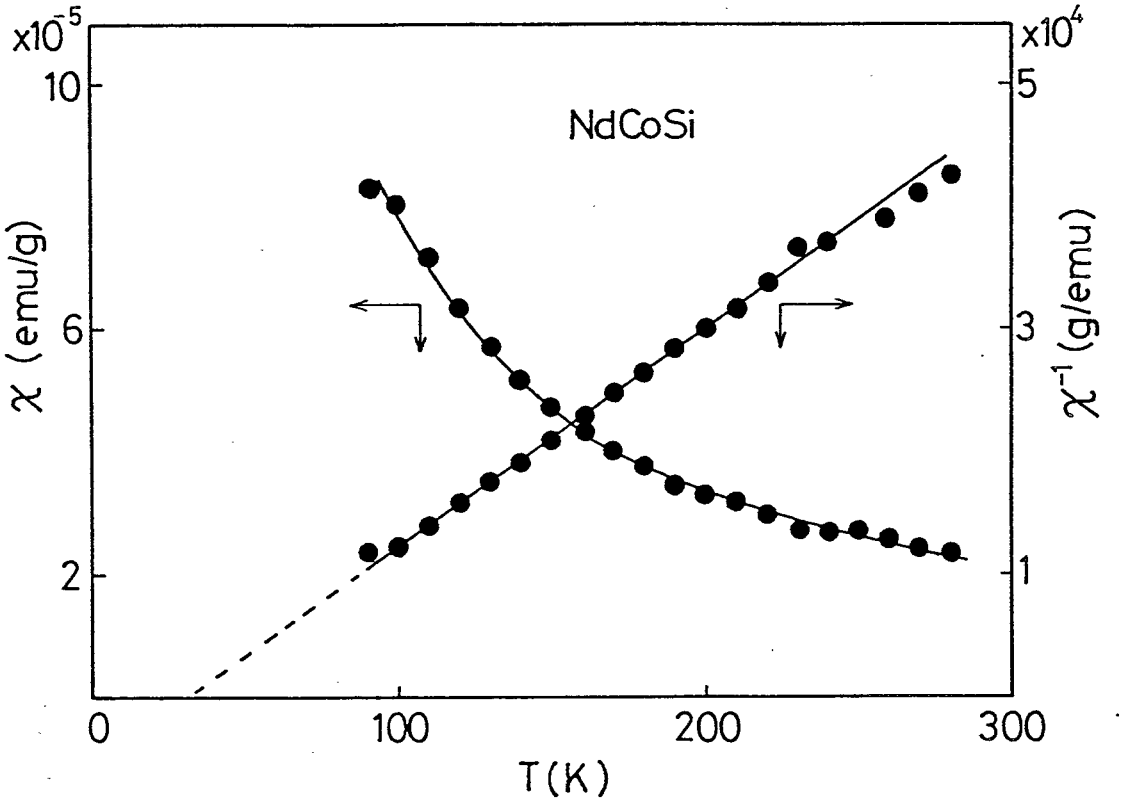

Fig. 19 Temperature dependences of magnetic susceptibility and inverse magnetic susceptibility for NdCoSi.

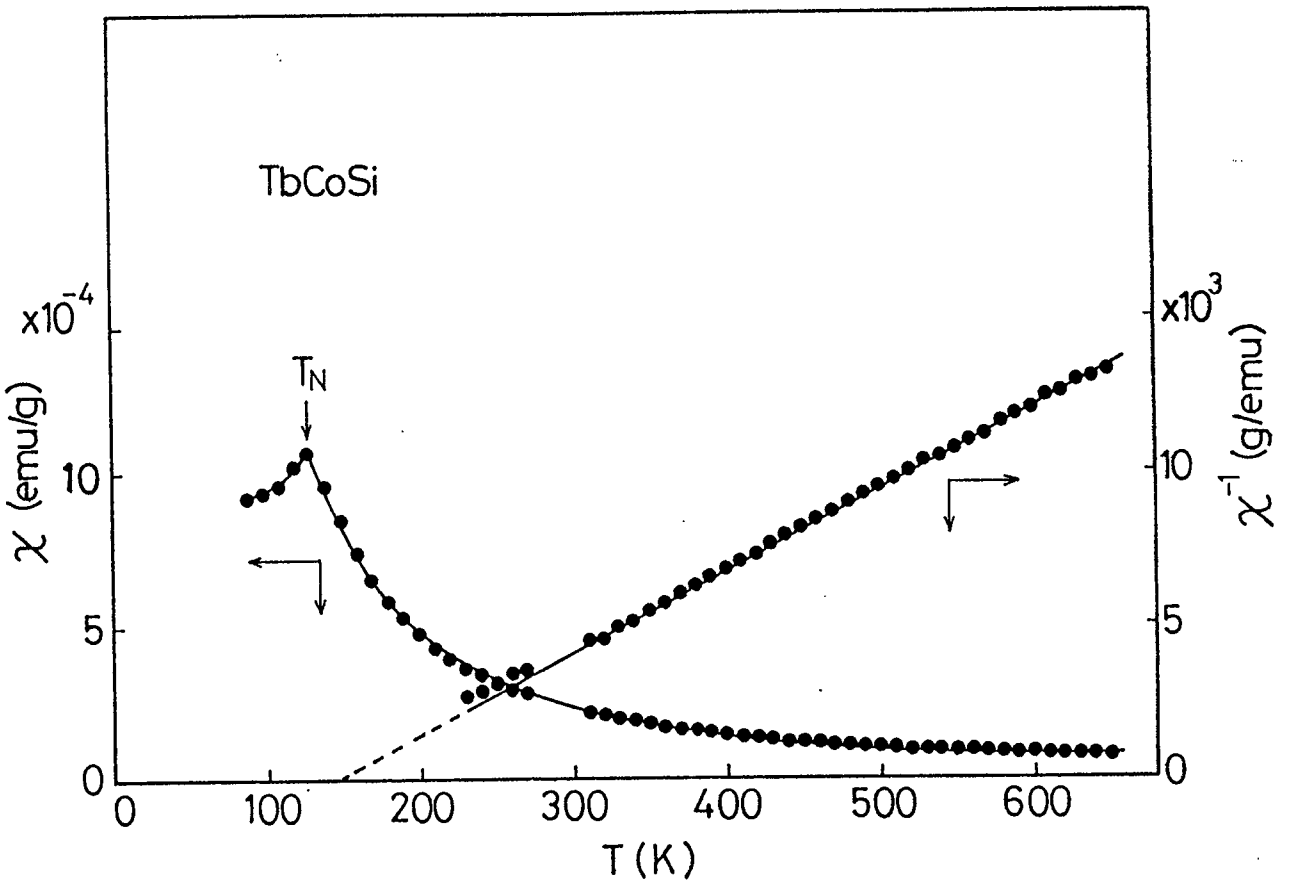

Fig. 20 Temperature dependences of magnetic susceptibility and inverse magnetic susceptibility for TbCoSi.

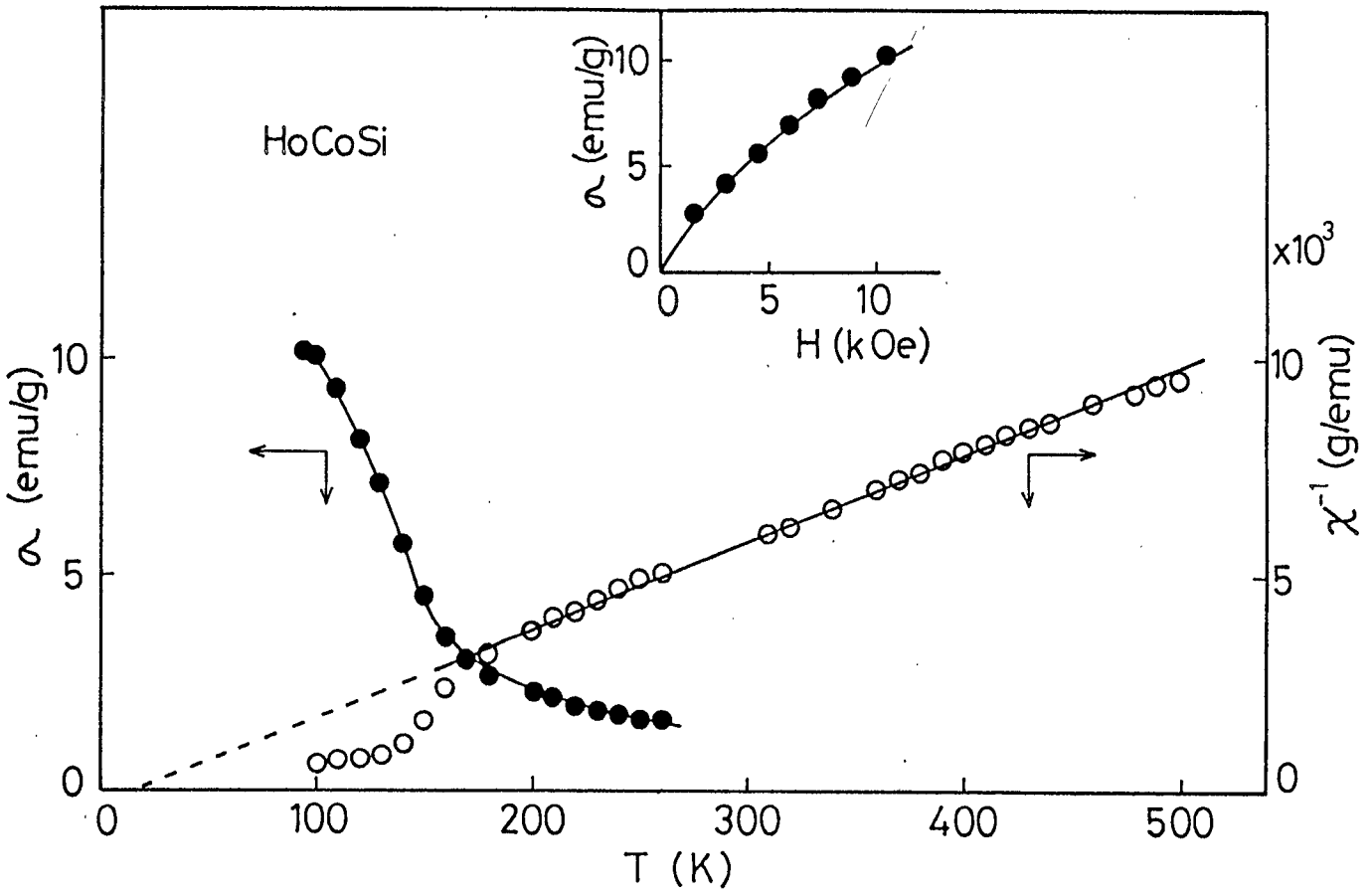

Fig. 21 Temperature dependences of magnetization and inverse magnetic susceptibility of HoCoSi and magnetization versus magnetic field.

in RCoSi, except GdCoSi, had little magnetic moments. The 3d shells of Co atoms probably fully occupied by the electrons transfered from Si atoms. In Fig. 22, paramagnetic Curie temperatures θ_a of RCoSi are plotted as a function of the de Genne function ξ. The solid line was calculated by the formula of $\theta_a = 20.9\ \xi^{2/3}$. The experimental values of θ_a were in good agreement with the calculated ones. This fact also indicated that Co atoms had little magnetic moments.

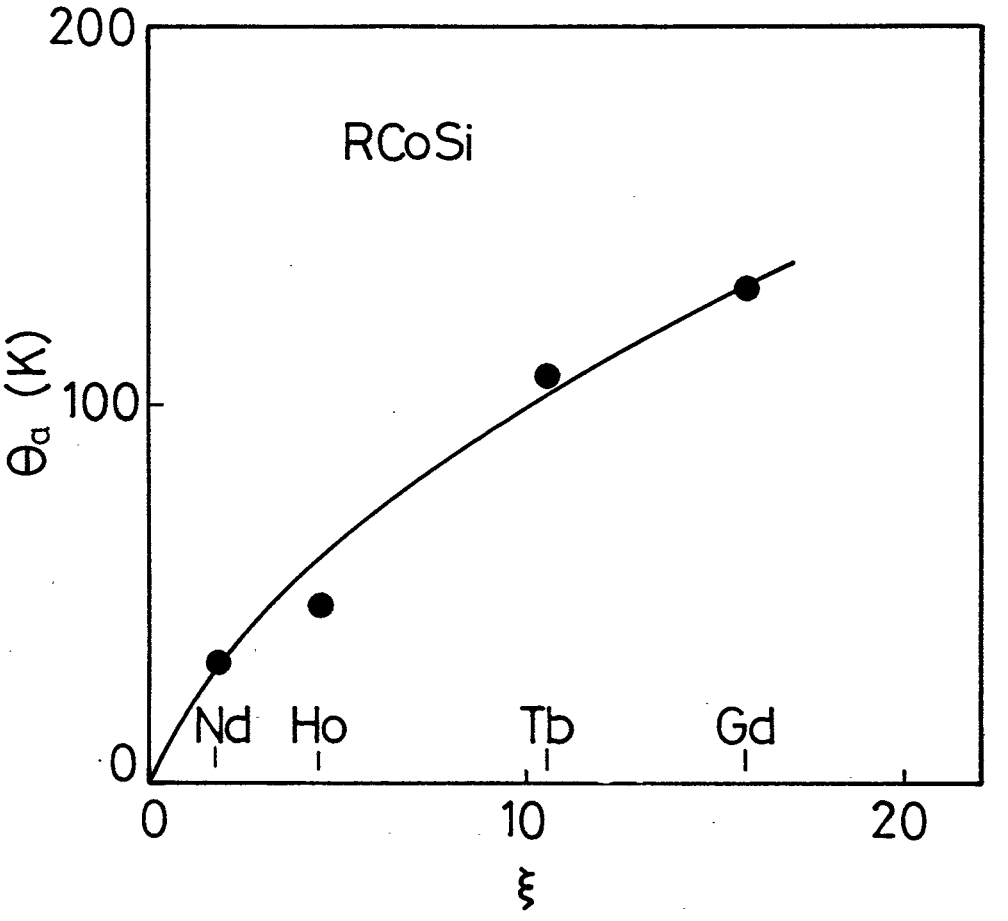

Fig. 22 Paramagnetic Curie temperatures of RCoSi compounds as a function of the de Genne function $\xi=(g-1)^2J(J+1)$. The solid line was calculated by the formula of $\Theta_a=20.9\xi^{2/3}$.

3-4 Preparation and magnetic and electrical properties of RNiSi (R=Nd, Gd)

RNiSi (R=Nd, Gd) were prepared by heating the starting materials at 900 °C for 7 days in the evacuated silica tubes. The crystal structure of NdNiSi was the tetragonal $ThSi_2$-type as shown in Fig. 23. Lattice constants were a=0.4083 nm and c=1.3922 nm. The X-ray powder diffraction pattern of GdNiSi was indexed on the basis of hexagonal lattice with a=0.8336 nm and c=0.6963 nm, but did not belong to the known crystal structure.

The temperature dependences of magnetic susceptibilities χ and χ^{-1} of NdNiSi are shown in Fig. 24. NdNiSi was paramagnetic above 77 K. The effective magnetic moment and paramagnetic Curie temperature were 3.6 μ_B and -16 K, respectively.

The temperature dependence of electrical resistivities ρ is shown in Fig. 25. The values of ρ increased with increasing temperature, indicating that NdNiSi was metallic.

The temperature dependences of χ and χ^{-1} for GdNiSi are shown in Fig. 26, together with the magnetization versus magnetic field plot. GdNiSi was paramagnetic above 77 K. The effective magnetic moment and paramagnetic Curie temperature were 7.4 μ_B and 9 K, respectively.

The values of effective magnetic moments were in good agreement with calculated values for Gd^{3+} ion. The 3d shell of Ni atoms is probably fully filled with electrons transfered from Si atoms.

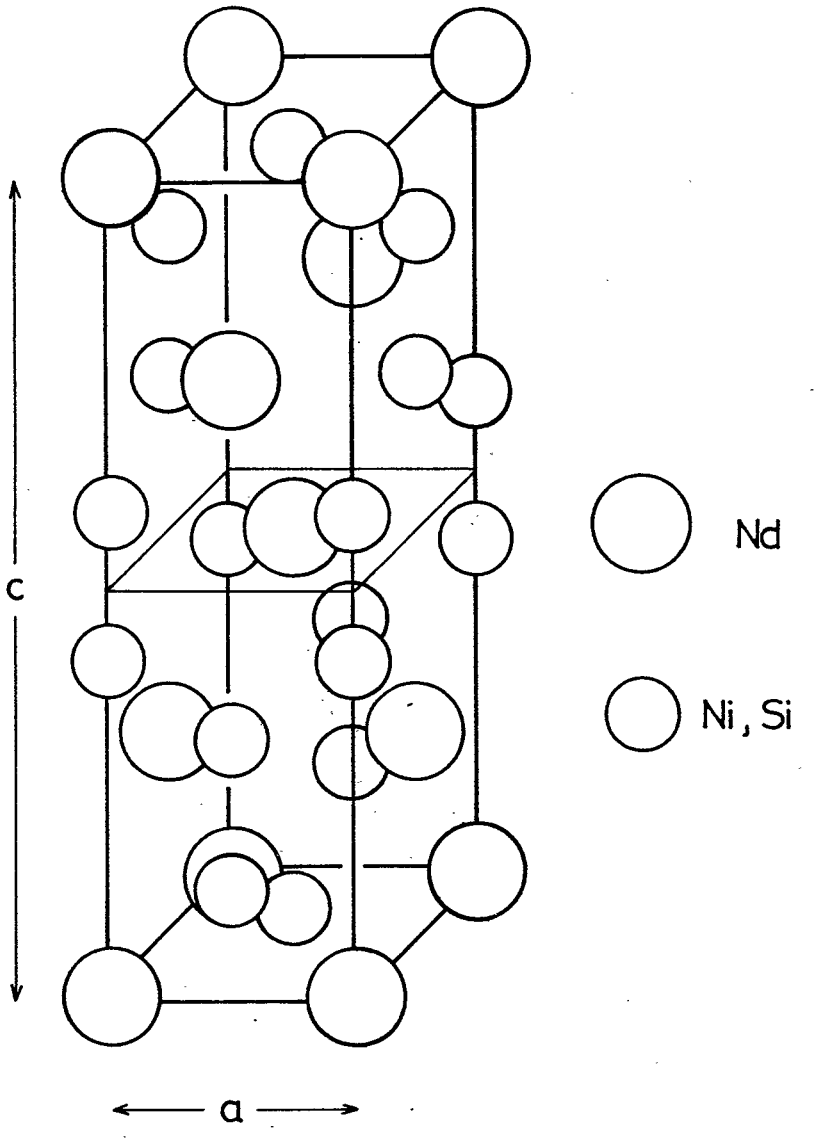

Fig. 23 Crystal structure of NdNiSi compound.

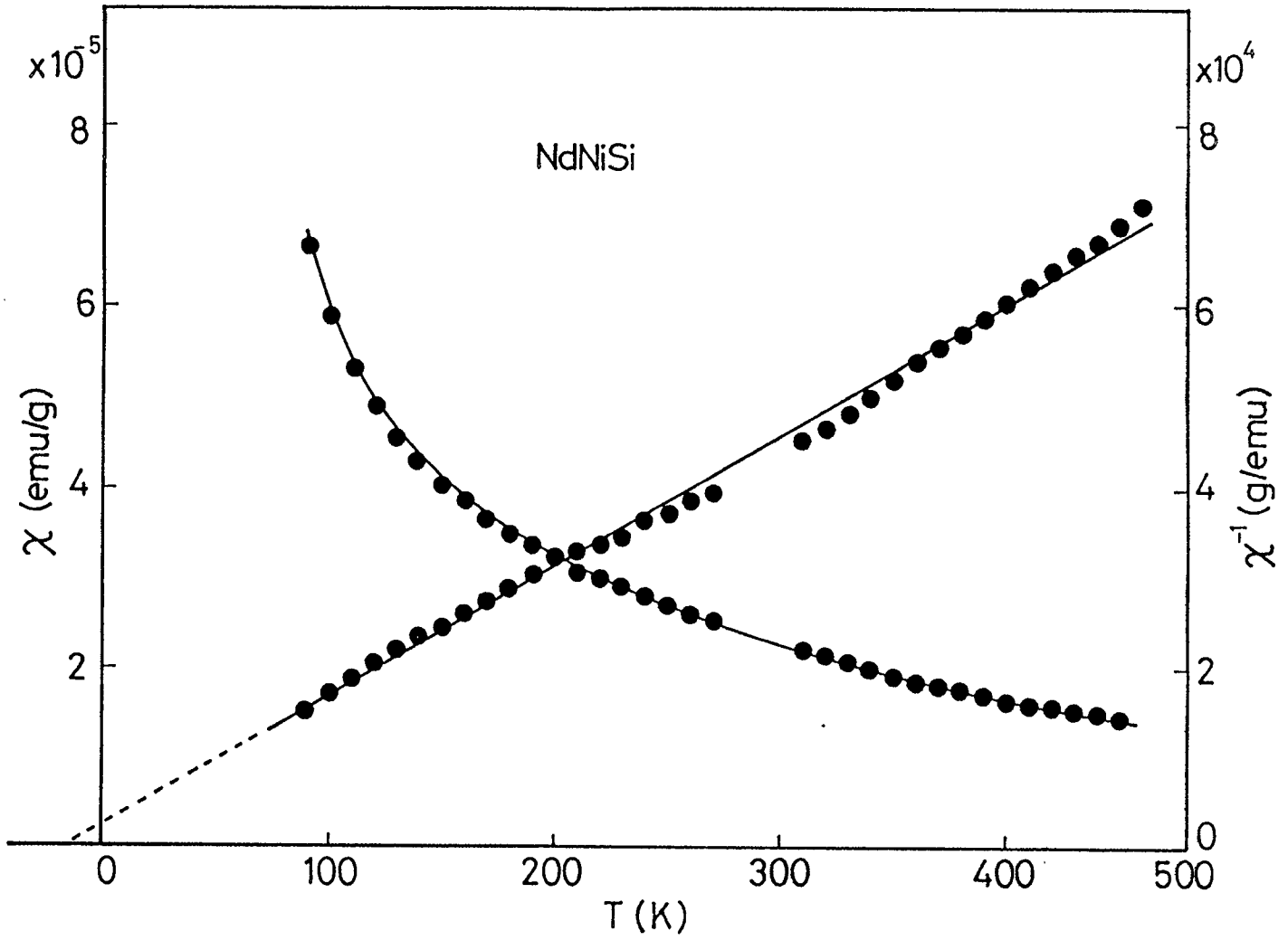

Fig. 24 Temperature dependences of magnetic susceptibility and inverse magnetic susceptibility of NdNiSi.

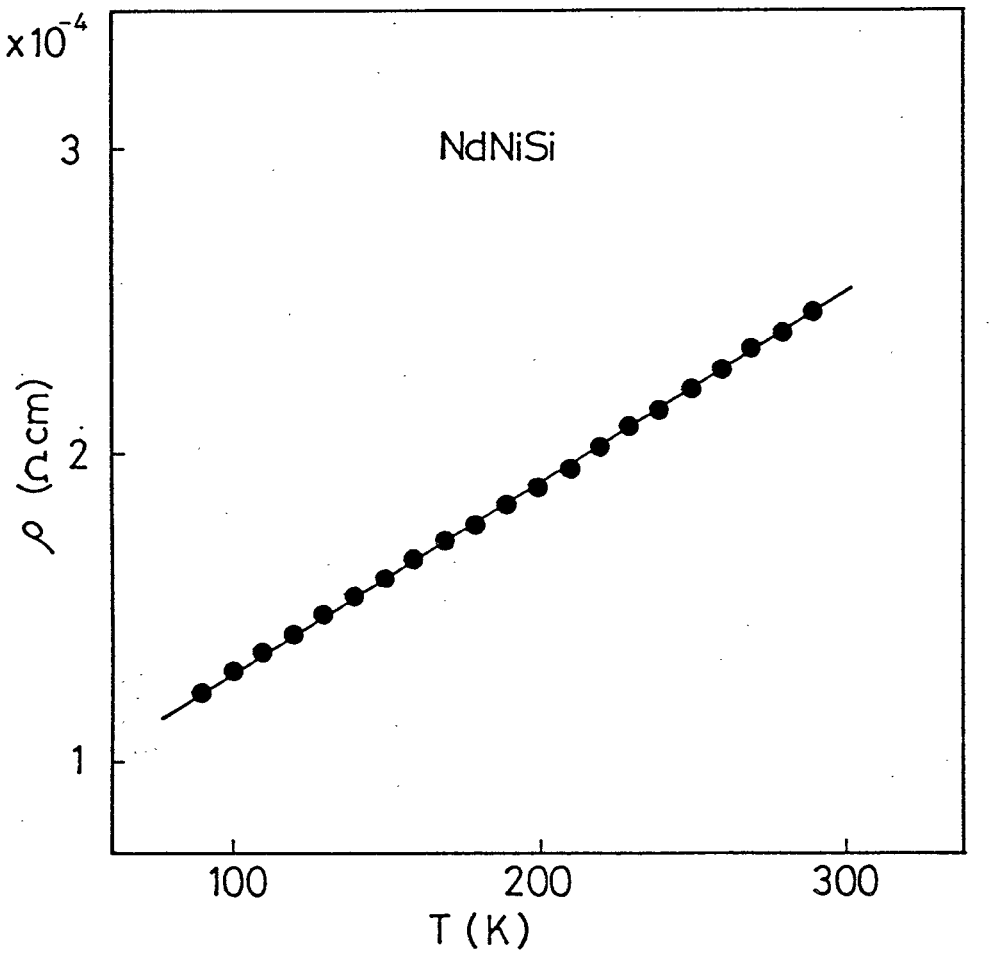

Fig. 25 Temperature dependence of electrical resistivity of NdNiSi.

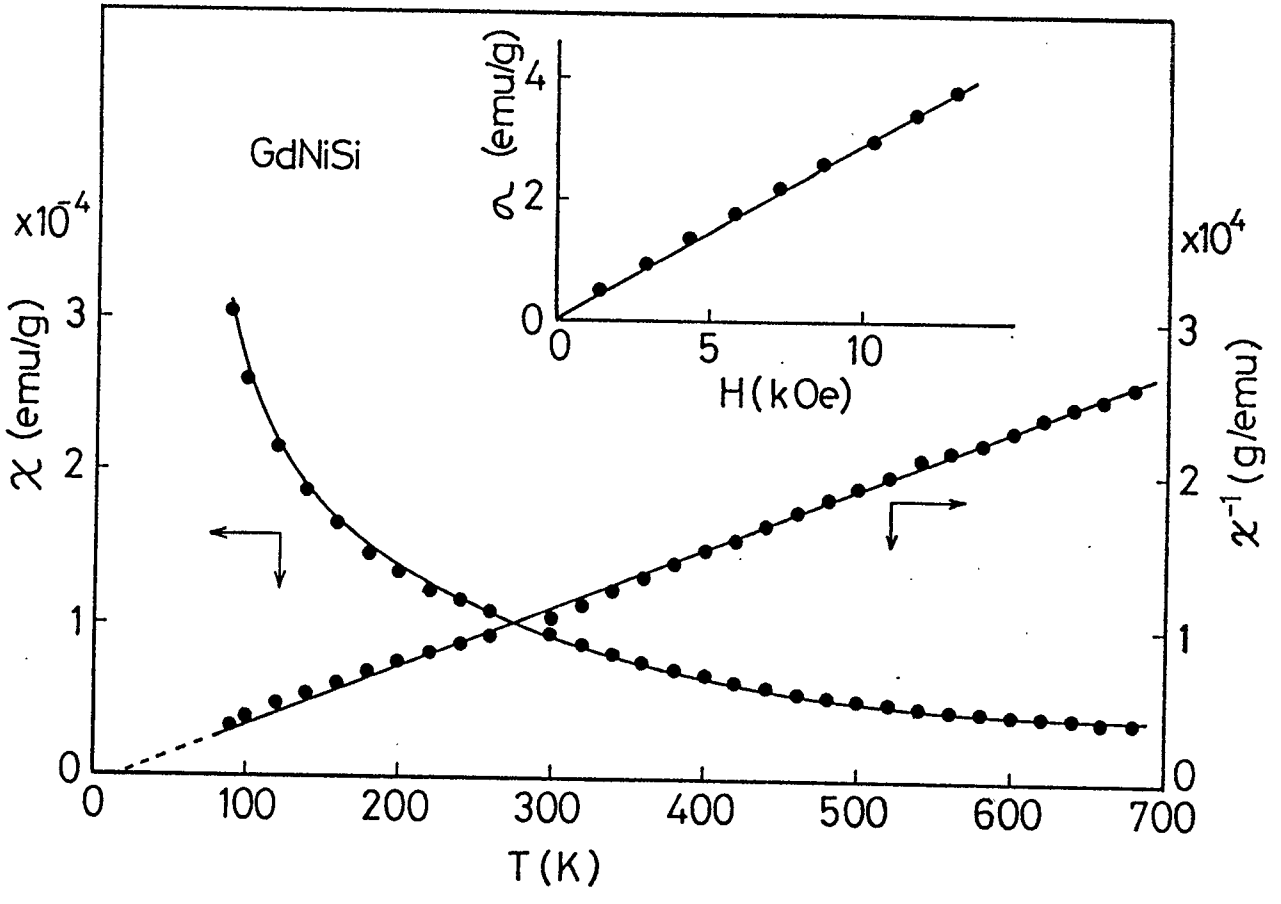

Fig. 26 Temperature dependences of magnetic susceptibility and inverse magnetic susceptibility of GdNiSi and magnetization versus magnetic field.

3-5 Preparation and magnetic and electrical properties of RCuSi (R=Y, Ce, Nd, Sm, Gd, Tb, Dy, Ho)

RCuSi were prepared by heating the starting materials at 900 °C for 7 days in the evacuated silica tubes.

The X-ray powder diffraction patterns of these compounds were completely indexed on the basis of the hexagonal AlB_2-type crystal structure. R atoms occupy the (1a) sites, and Cu and Si atoms occupy the (2d) sites. Lattice constants, c/a and unit cell volumes for RCuSi are listed in Table 7, and plotted in Fig. 27. Lattice constants, c/a and unit cell volumes decreased linearly with increasing atomic number of rare-earth elements. This fact indicated that the valence state of rare-earth ion was trivalent. The c-axis decreased more rapidly than the a-axis, indicating that the distance between hexagonal layers (Fig. 5b) mainly decreased when the radius of the rare-earth atom became small.

The temperature dependence of magnetic susceptibility χ of RCuSi is shown in Fig. 28. The values of χ of SmCuSi and YCuSi were 10^2 times smaller than those of other RCuSi compounds, and no temperature dependence was found. The magnitude of χ for RCuSi increased with increasing the magnetic moment of rare-earth element. In the temperature range above 100 K, χ^{-1}-T relations of all these compounds, except YCuSi and SmCuSi, obeyed the Curie-Weiss law.

The effective magnetic moments μ_{eff} of RCuSi are shown in Fig. 29. The solid line indicates the calculated values for the R^{3+} ions. The observed effective magnetic moments of RCuSi were in good agreement with the calculated ones, assuming that rare-earth ions were trivalent and copper atoms had no

Table 7 Lattice parameters of RCuSi compounds

RCuSi	a (10^{-1}nm)	c (10^{-1}nm)	c/a	V (10^{-3}nm^3)
YCuSi	4.143	3.730	0.9003	55.45
CeCuSi	4.246	3.937	0.9272	61.47
NdCuSi	4.212	3.915	0.9295	60.15
SmCuSi	4.188	3.845	0.9181	58.40
GdCuSi	4.178	3.781	0.9050	57.16
TbCuSi	4.159	3.747	0.9009	56.10
DyCuSi	4.184	3.709	0.8865	56.23
HoCuSi	4.139	3.680	0.8891	54.60

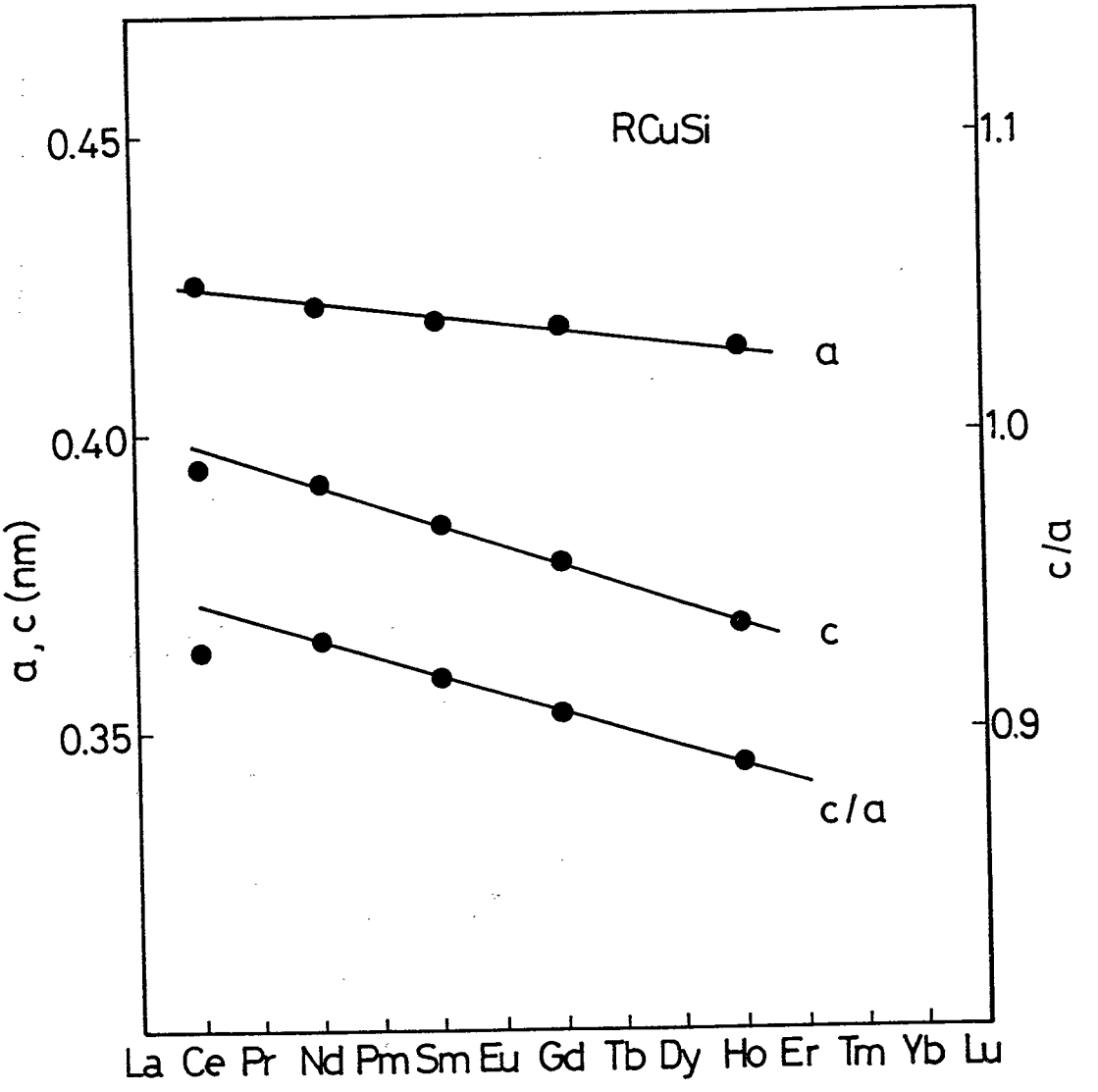

Fig. 27 Lattice constants of RCuSi compounds.

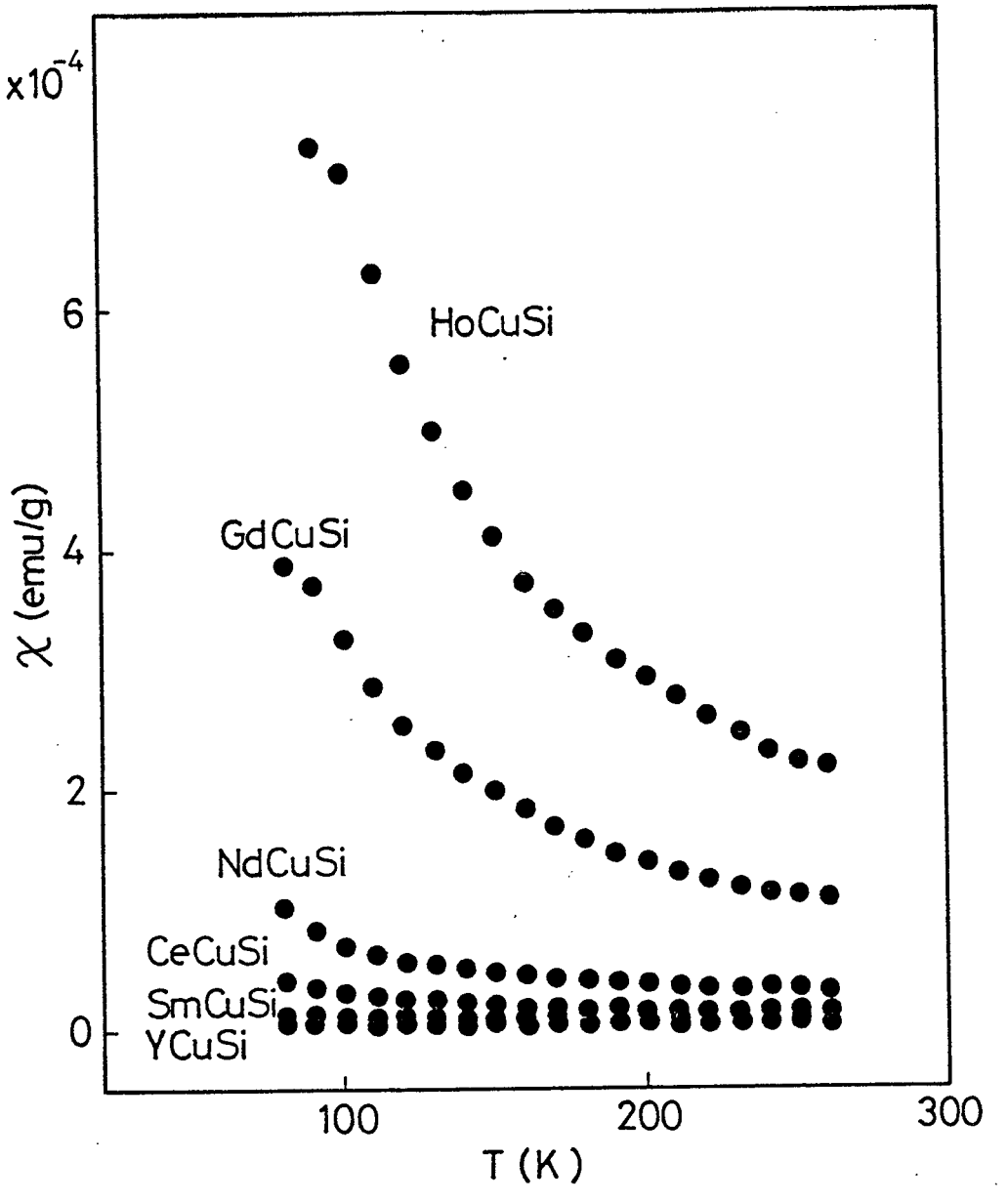

Fig. 28 Temperature dependence of magnetic susceptibility of RCuSi compounds.

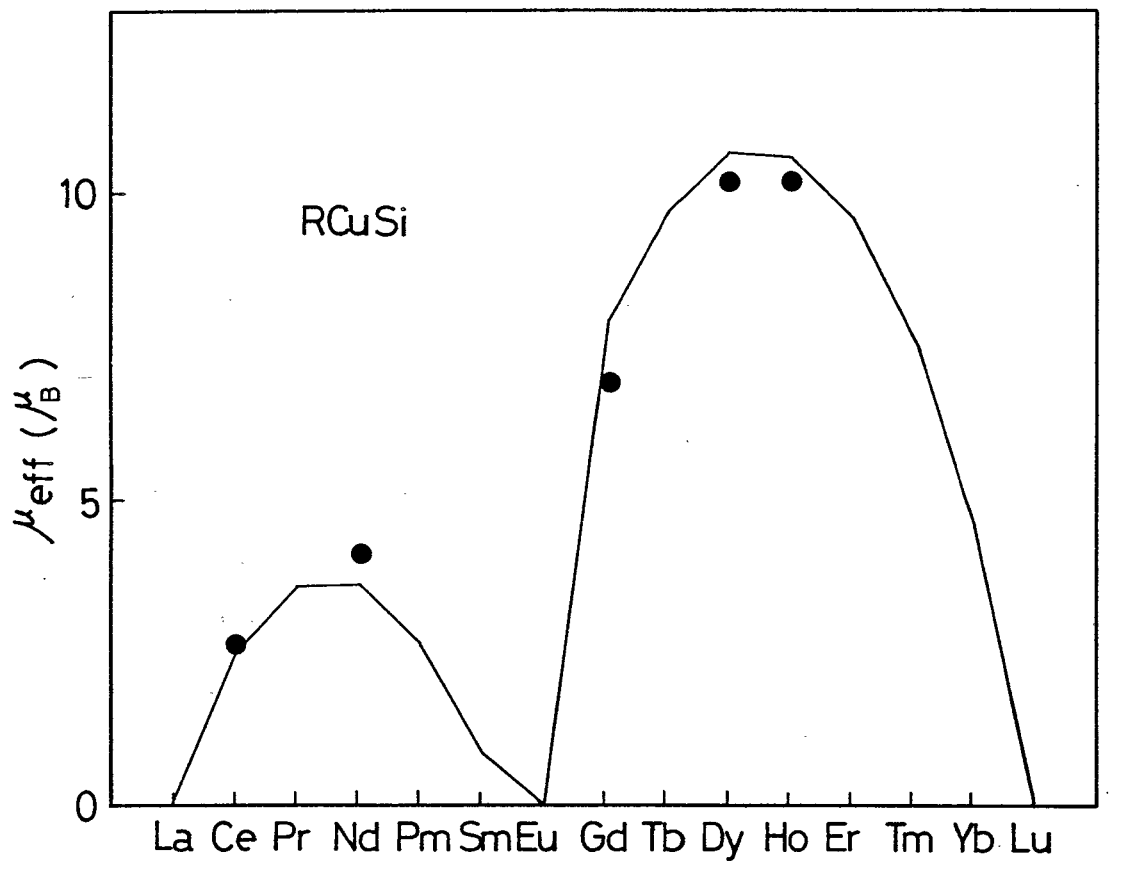

Fig. 29 Effective magnetic moments of RCuSi compounds. The solid line was calculated for R^{3+} ions.

magnetic moment.

The paramagnetic Curie temperatures, θ_a, for these compounds are plotted in Fig. 30. The values of θ_a were negative for compounds containing light rare-earth elements, but positive for RCuSi compounds containing heavy rare-earth elements. These results were similar with those obtained for rare-earth metals. Howere, magnitude of θ_a for RCuSi was rather smaller than those for rare-earth metals. This is due to the elongation of distance between rare-earth atoms in the RCuSi compounds.

The temperature dependences of the electrical resistivities of RCuSi compounds are shown in Fig. 31. The electrical resistivity, ρ, increased with increasing temperature, which indicated that these compounds were metallic. The temperature gradient of ρ increased with increasing the atomic number of rare-earth element. The electrical resistivity is caused by scattering the electrons by not only phonons and defects, but also spins of R ions in RCuSi compounds.

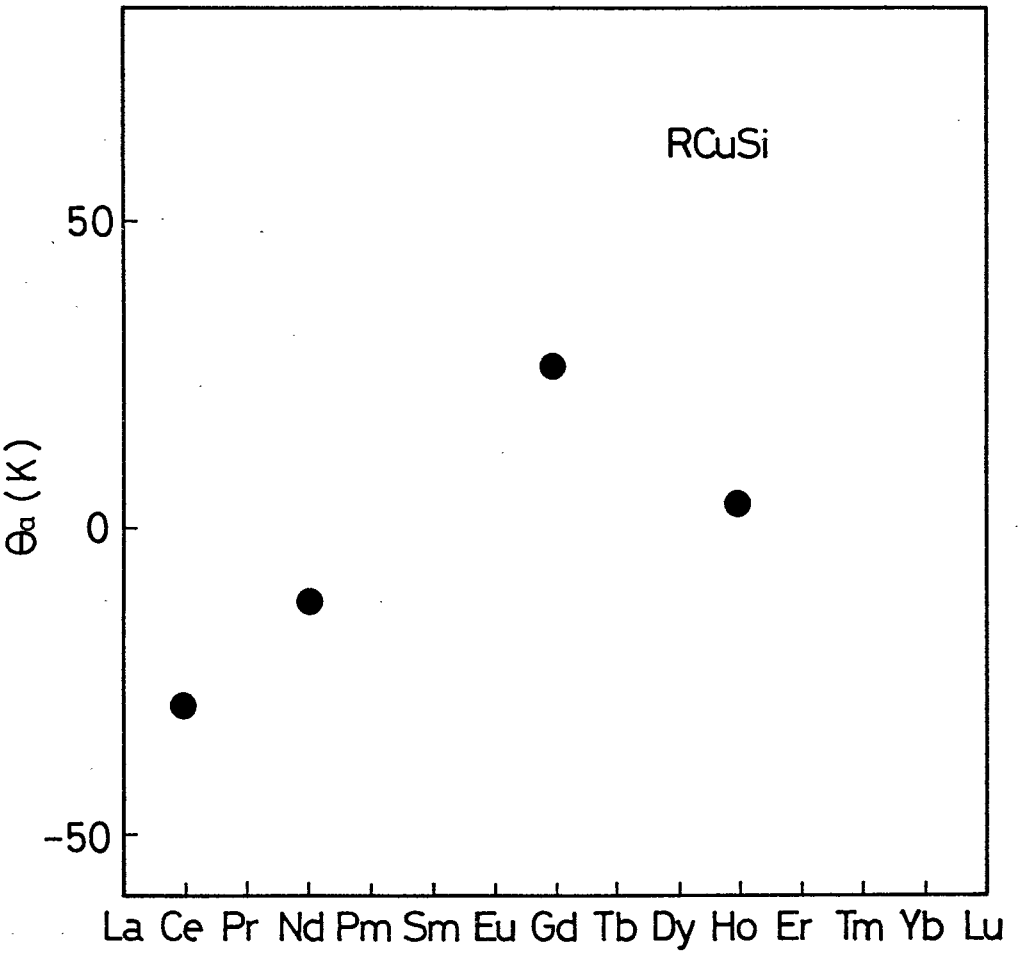

Fig. 30 Paramagnetic Curie temperatures for RCuSi compounds.

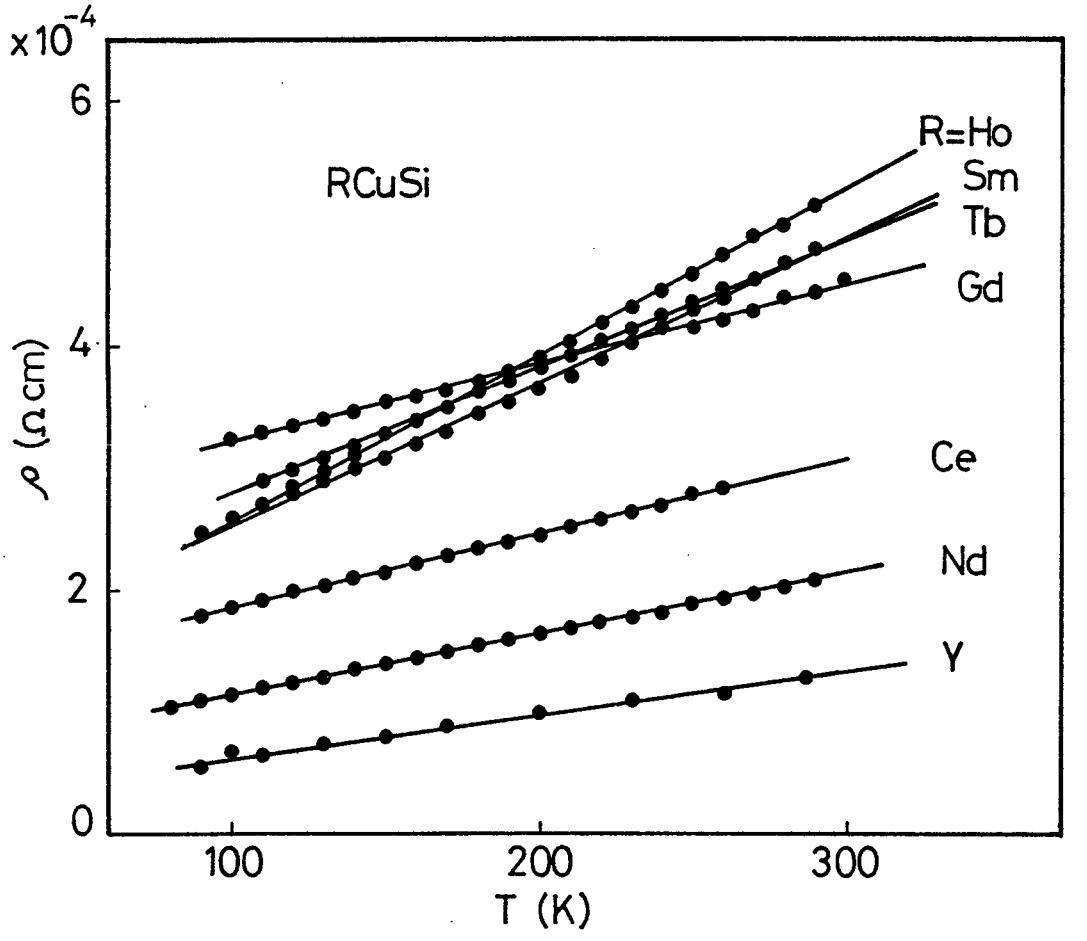

Fig. 31 Temperature dependence of electrical resistivity of RCuSi compounds.

3-6 Preparation and magnetic and electrical properties of RZnSi (R=Y, Ce, Nd, Sm, Gd, Tb, Dy, Ho)

RZnSi were prepared by heating the mixture of starting materials at 500 °C for 1 day, then grinding and heating again at 900 °C for 10 days in the evacuated silica tubes.

The X-ray powder diffraction patterns of these compounds were completely indexed on the basis of the hexagonal AlB_2-type crystal structure. Lattice constants, c/a and unit cell volumes for RZnSi are listed in Table 8, and compositional dependence of crystallographycal parameters is shown in Fig. 32. As seen in Fig. 32, they decreased with increasing the atomic number of rare-earth elements. This fact indicated that the valence state of rare-earth ions was trivalent. The c-axis decreased more rapidly than the a-axis, which is the same results as RCuSi.

The temperature dependences of magnetic susceptibilities are shown in Fig. 33. The values of χ for YZnSi and SmZnSi reveal no temperature dependence. The χ^{-1}-T relations of other RZnSi compounds obeyed the Curie-Weiss law.

The observed effective magnetic moments of RZnSi are shown in Fig. 34. The solid line indicated the calculated values for R^{3+} ions. The observed values of effective magnetic moments were in good agreement with the calculated ones. This fact indicated that the magnetic moment of RZnSi is due to the rare-earth atoms with an electronic configuration $(4f)^n(5s)^2(5p)^6$. It is considered that electrons in $(5d)^1(6s)^2$ would be supplied to the conduction band.

The paramagnetic Curie temperature of RZnSi is plotted in Fig. 35. The absolute values of paramagnetic Curie

Table 8 Lattice parameters of RZnSi compounds

RZnSi	a (10^{-1}nm)	c (10^{-1}nm)	c/a	V ($10^{-3}nm^3$)
YZnSi	4.135	3.968	0.9596	58.76
CeZnSi	4.223	4.238	1.004	65.45
NdZnSi	4.167	4.174	1.002	62.77
SmZnSi	4.147	4.095	0.9875	60.99
GdZnSi	4.163	4.000	0.9608	60.03
TbZnSi	4.141	3.962	0.9568	58.84
DyZnSi	4.119	3.944	0.9575	57.95
HoZnSi	4.103	3.941	0.9605	57.46

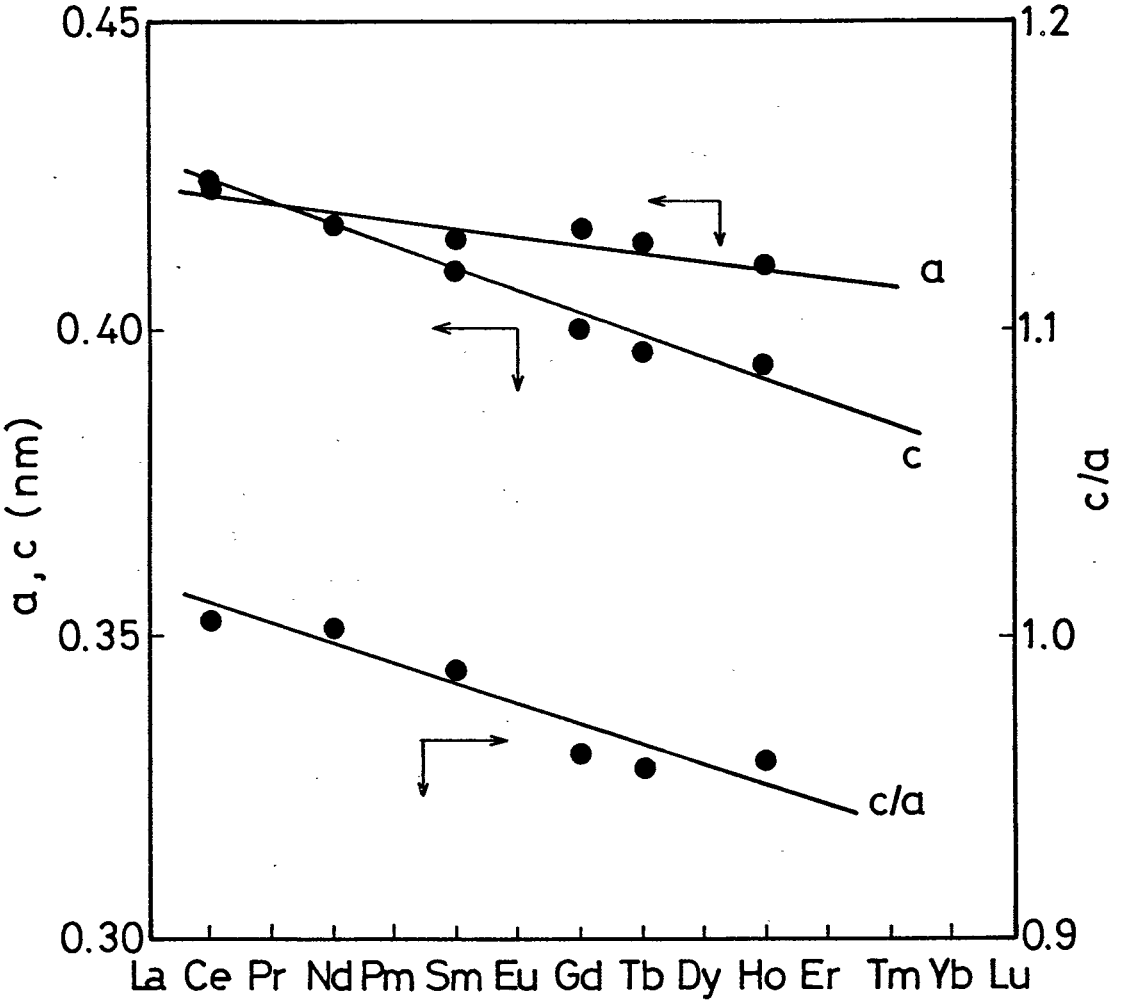

Fig. 32 Lattice constants of RZnSi compounds.

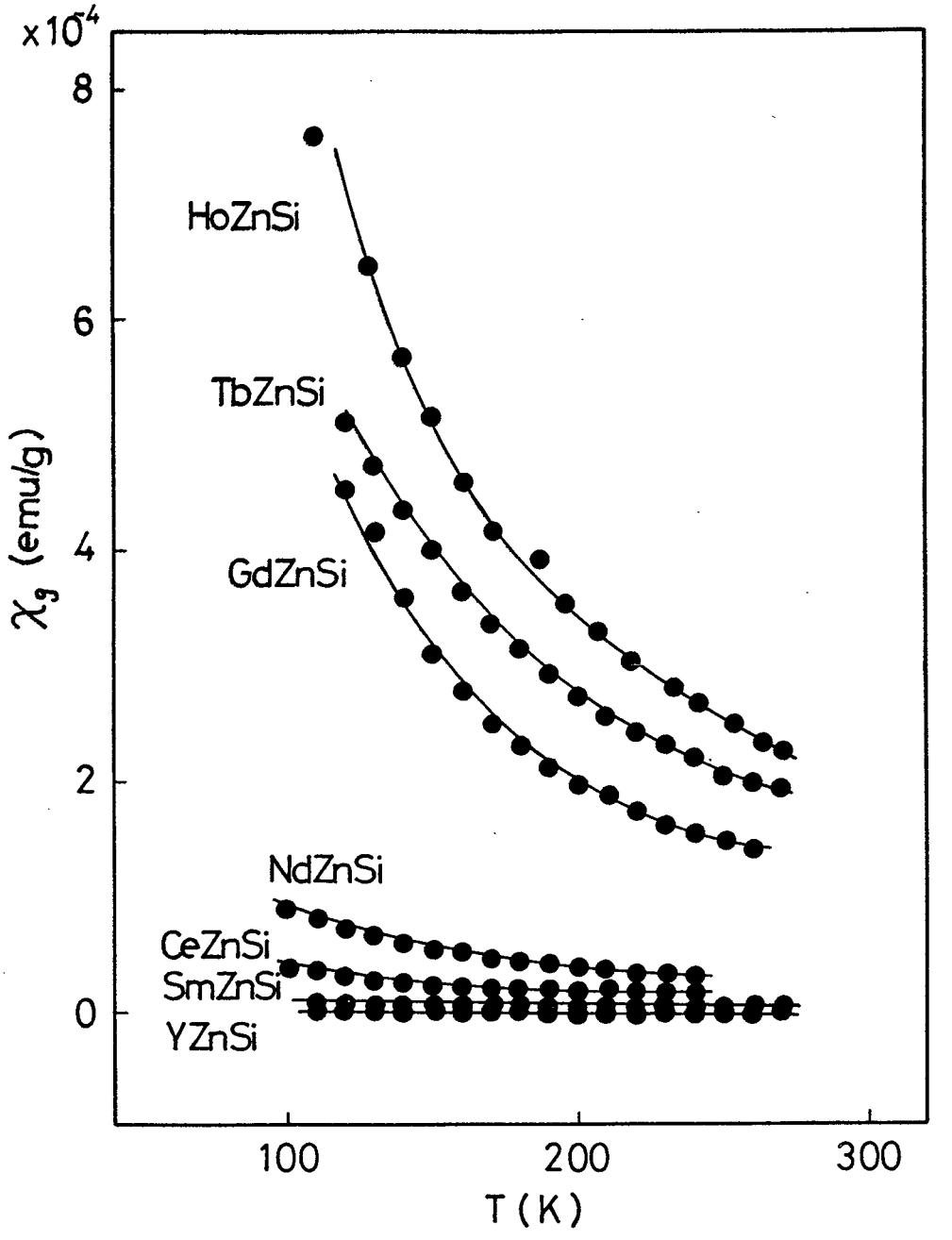

Fig. 33 Temperature dependence of magnetic susceptibility of RZnSi compounds.

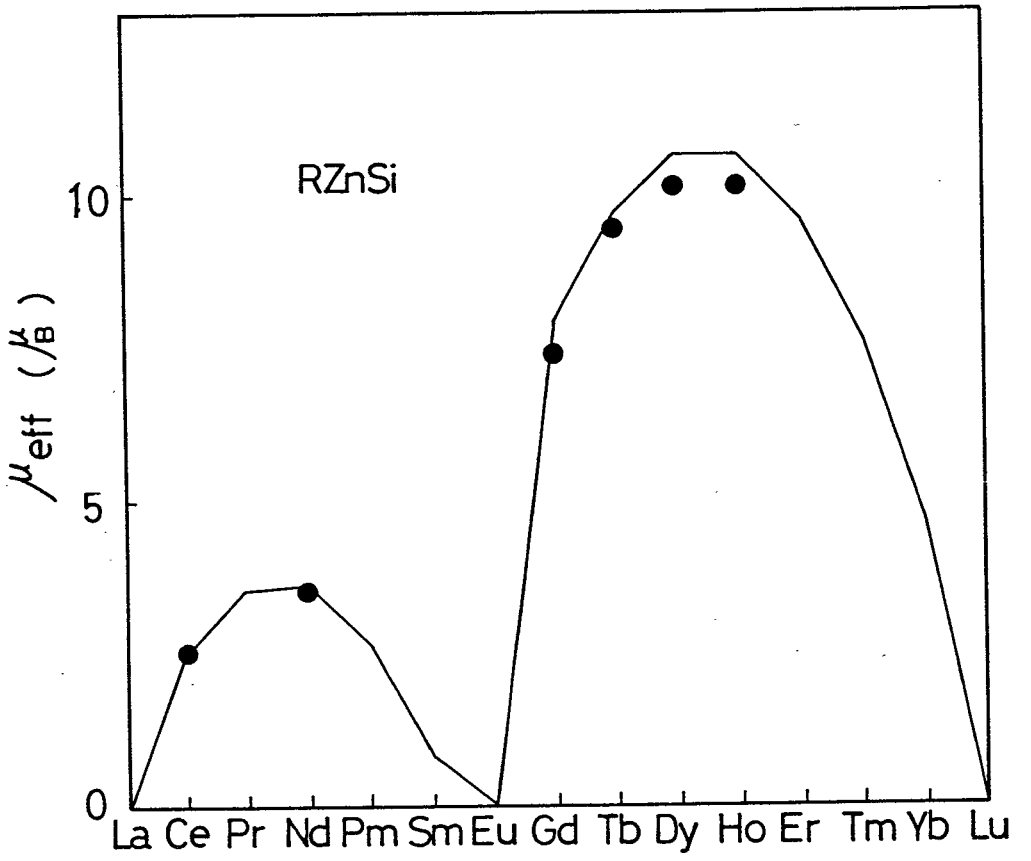

Fig. 34 Effective magnetic moments of RZnSi compounds. The solid line was calculated for R^{3+} ions.

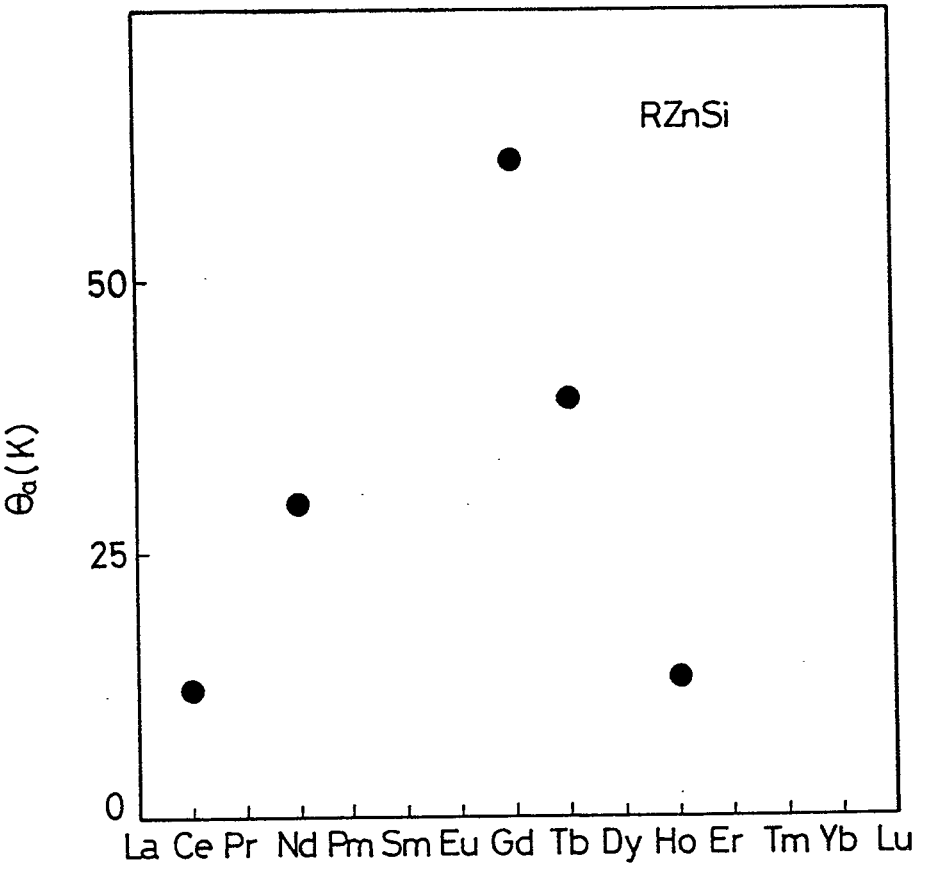

Fig. 35 Paramagnetic Curie temperatures of RZnSi compounds.

temperature for RZnSi were larger than those of RCuSi.

In Fig. 36, paramagnetic Curie temperatures, θ_a, of RZnSi and RCuSi are plotted against the de Genne function, ξ. The value of θ_a increased with increasing ξ.

The temperature dependences of the electrical resistivities, ρ, of RZnSi are shown in Fig. 37. The values of ρ of RZnSi increased with increasing temperature, showing that these compounds were metallic.

The temperature dependences of the thermoelectric powers, S, of RZnSi are shown in Fig. 38. The absolute values of S increased with increasing temperature.

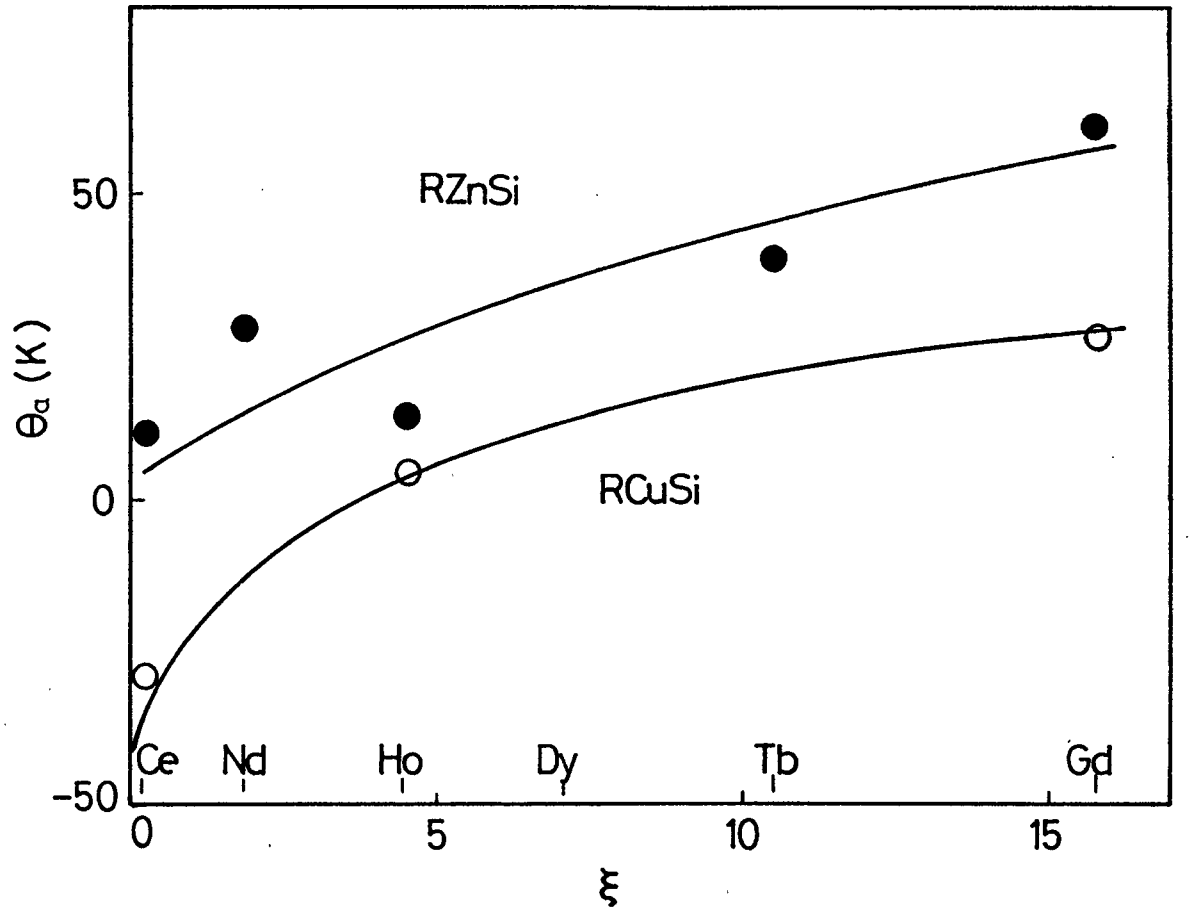

Fig. 36 Dependences of paramagnetic Curie temperatures of RCuSi and RZnSi compounds on the de Genne function.

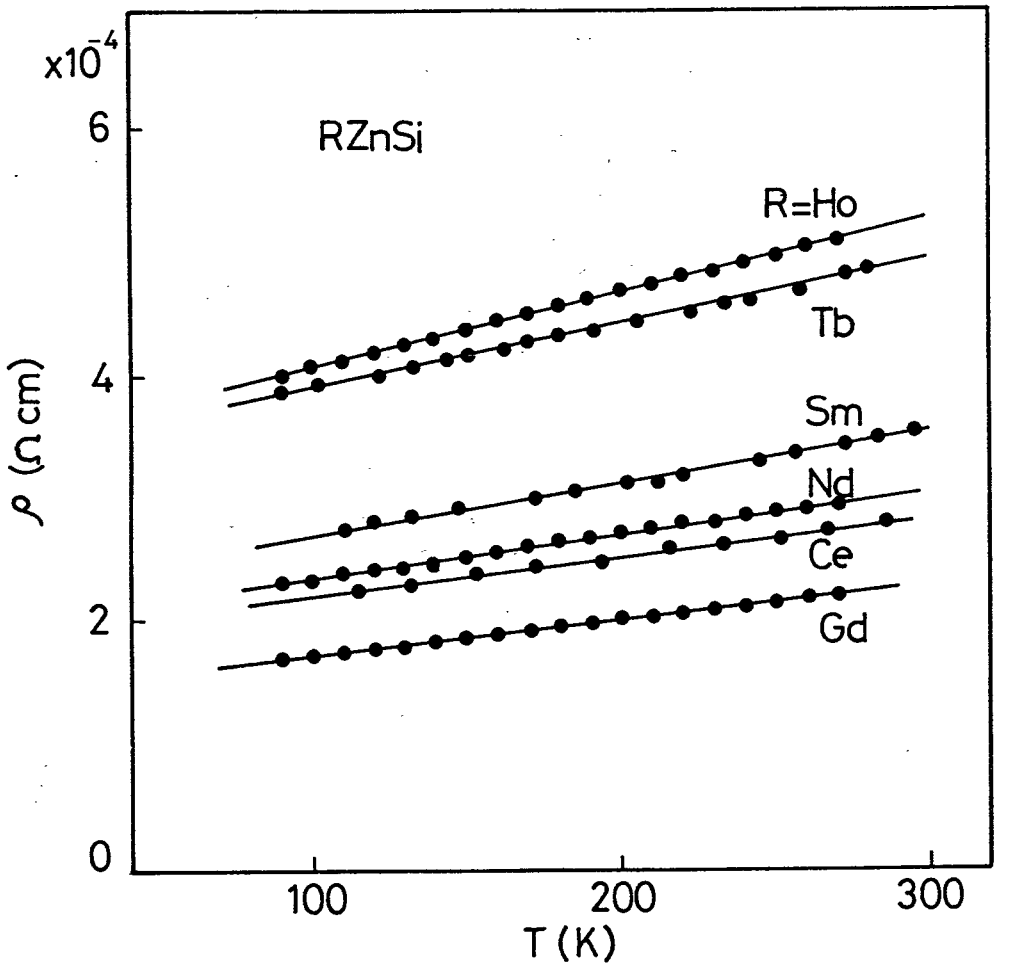

Fig. 37 Temperature dependence of electrical resistivity of RZnSi compounds.

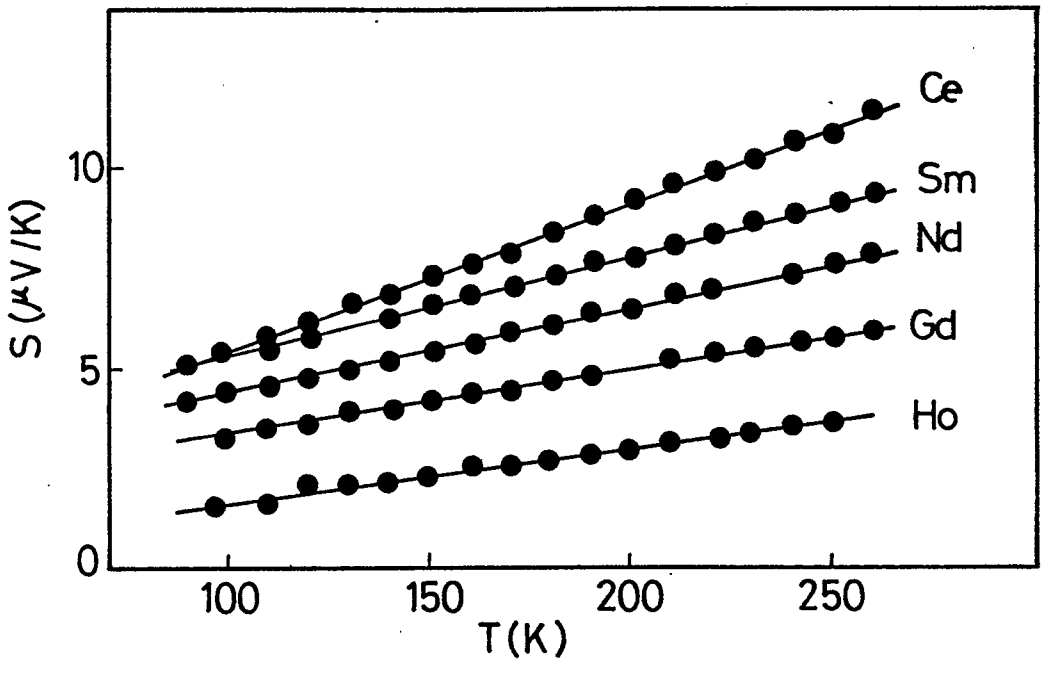

Fig. 38 Temperature dependence of thermoelectric power of RZnSi compounds.

3-7 Preparation and magnetic and electrical properties of $GdCu_{1-x}Zn_xSi$ ($0 \leq x \leq 1$)

The pseudo-ternary $GdCu_{1-x}Zn_xSi$ compounds were prepared by heating the mixed powders of GdCuSi and GdZnSi with desired ratios at 900 ℃ for 7 days in the evacuated silica tube (86). The preparation procedure is shown in Fig. 39. The preparation of GdCuSi and GdZnSi have been already described in 3-5 and 3-6, respectively.

The X-ray powder diffraction patterns of these compounds were completely indexed on the basis of the hexagonal AlB_2-type structure. The rare-earth atoms occupy the (1a) sites and the other atoms occupy the (2d) sites. The compositional dependences of lattice constants of these compounds are plotted in Fig. 40. Lattice parameters obeyed the Vegard's law. This fact indicated that copper atoms were randomly replaced by zinc atoms. Lattice parameter a was almost constant, but c linearly increased with increasing the compositional parameter x, indicating that only distances between the graphite-like layers increased when the amount of zinc atoms increased.

The electrical resistivities, ρ, of $GdCu_{1-x}Zn_xSi$ are shown in Fig. 41. The ρ increased with increasing temperature, indicating that these compounds were metallic. the change in slope was observed in the composition range from x=0.1 to x=0.6, which corresponded to the magnetic phase transition from the ferromagnetic phase to the paramagnetic phase.

The $d\rho/dT$ of $GdCu_{1-x}Zn_xSi$ are plotted as a function

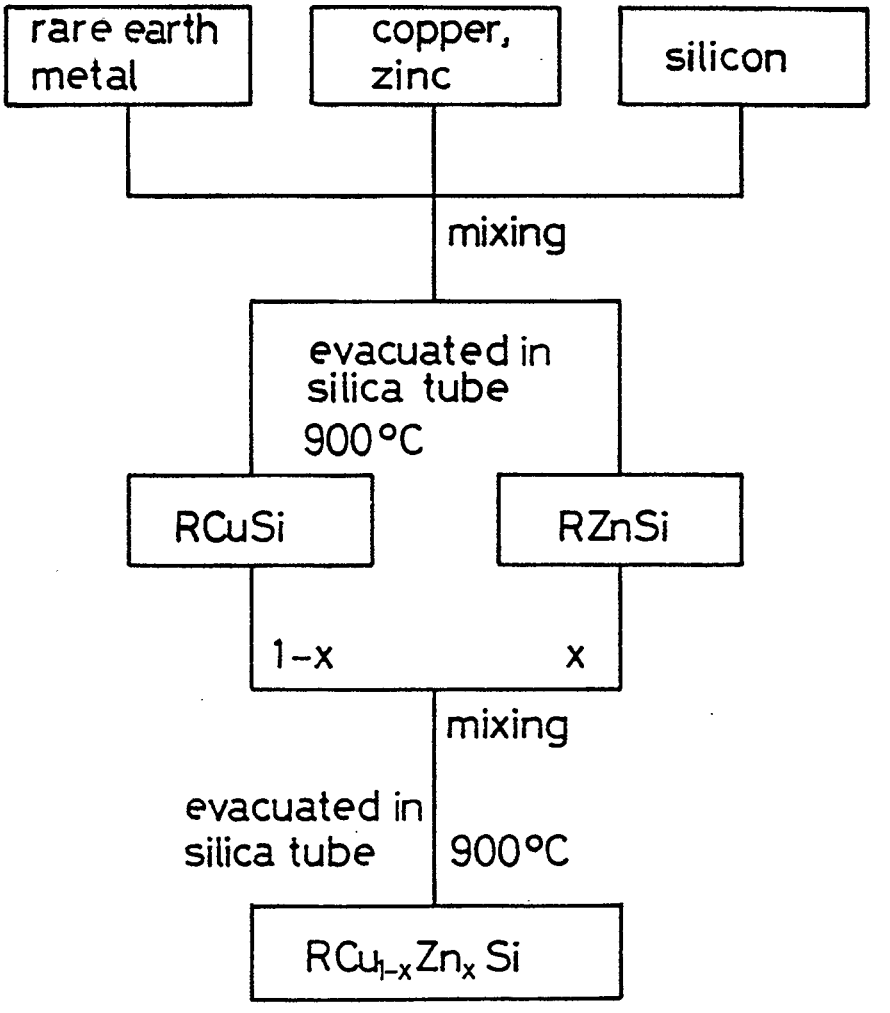

Fig. 39 Preparation procedure of $RCu_{1-x}Zn_xSi$ compounds.

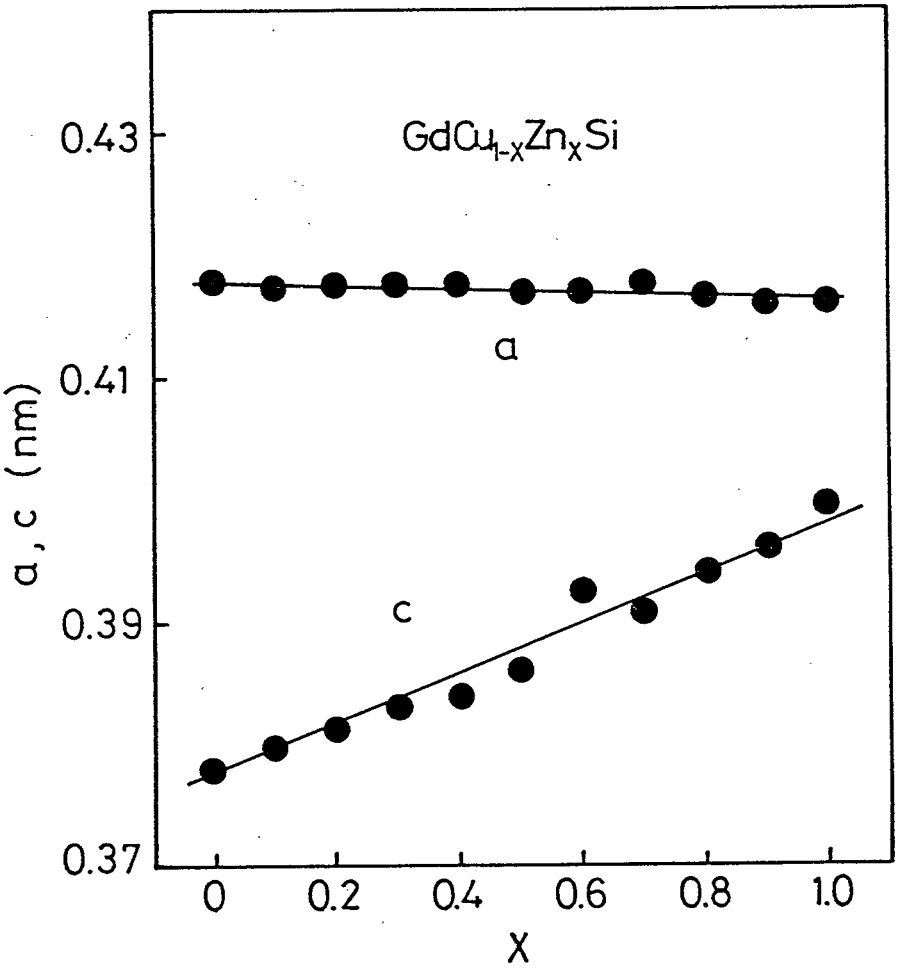

Fig. 40 Lattice constants of $GdCu_{1-x}Zn_xSi$ compounds.

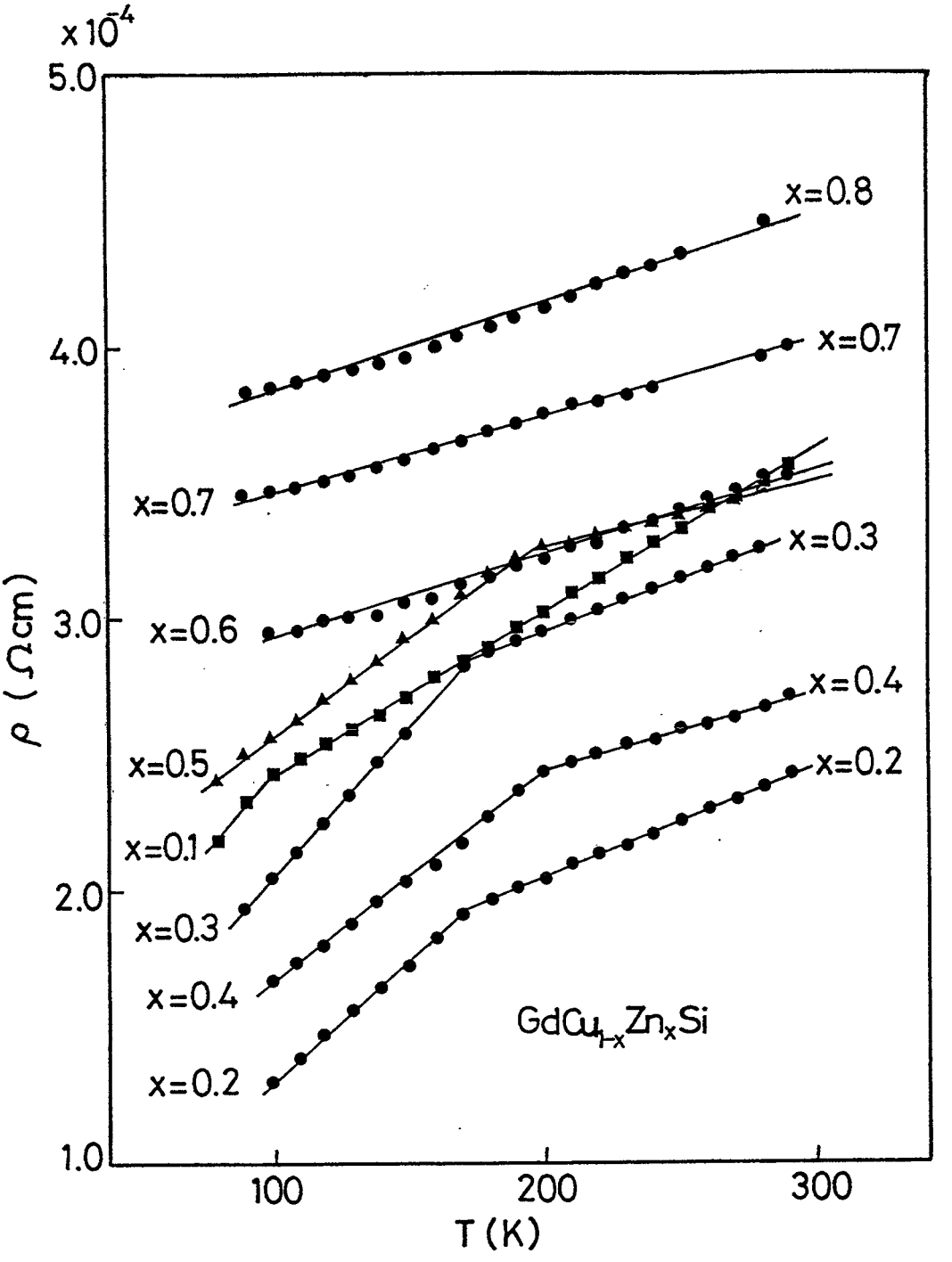

Fig. 41 Temperature dependence of electrical resistivity of $GdCu_{1-x}Zn_xSi$ compounds.

of x in Fig. 42. The change in $d\rho/dT$ is related to the concentration of conduction electrons in conduction band. The values of $d\rho/dT$ decreased with drawing an arc having the negative derivative with respect to x.

The magnetization, σ, versus applied magnetic field H, for $GdCu_{1-x}Zn_xSi$ is shown in Fig. 43. The σ of samples having chemical compositions from x=0.1 to x=0.6 were saturated above 10 kOe at 77 K, but magnetic moments of other compositions were not saturated up to 13 kOe.

The temperature dependences of σ and inverse magnetic susceptibility, χ^{-1}, of $GdCu_{1-x}Zn_xSi$ are shown in Fig. 44. From Fig. 44, it was found that $GdCu_{1-x}Zn_xSi$ (x=0.1-0.6) were ferromagnetic, and χ^{-1}-T relation obeyed the Curie-Weiss law in the paramagnetic region.

Both ferromagnetic moments, n_f, and Curie temperatures, T_c, are plotted against the compositional parameter, x, in Fig. 45. The values of n_f and T_c had the maximum values of n_f=6.4 μ_B and T_c=195 K at x=0.4. It is considered that the value of n_f=6.4 μ_B is due to the almost parallel alignment of the Gd^{3+} spins.

The effective magnetic moments, μ_{eff}, and paramagnetic Curie temperatures, θ_a, are shown in Fig. 46. All values of θ_a were positive, and also had a peak at x=0.4. The values of μ_{eff} were about 7 μ_B for all composition range, which agreed well with the calculated values for Gd^{3+} ion. These results suggested that magnetic interactions between Gd^{3+} spins play an important role to determine the magnetic properties of $GdCu_{1-x}Zn_xSi$ compounds and they

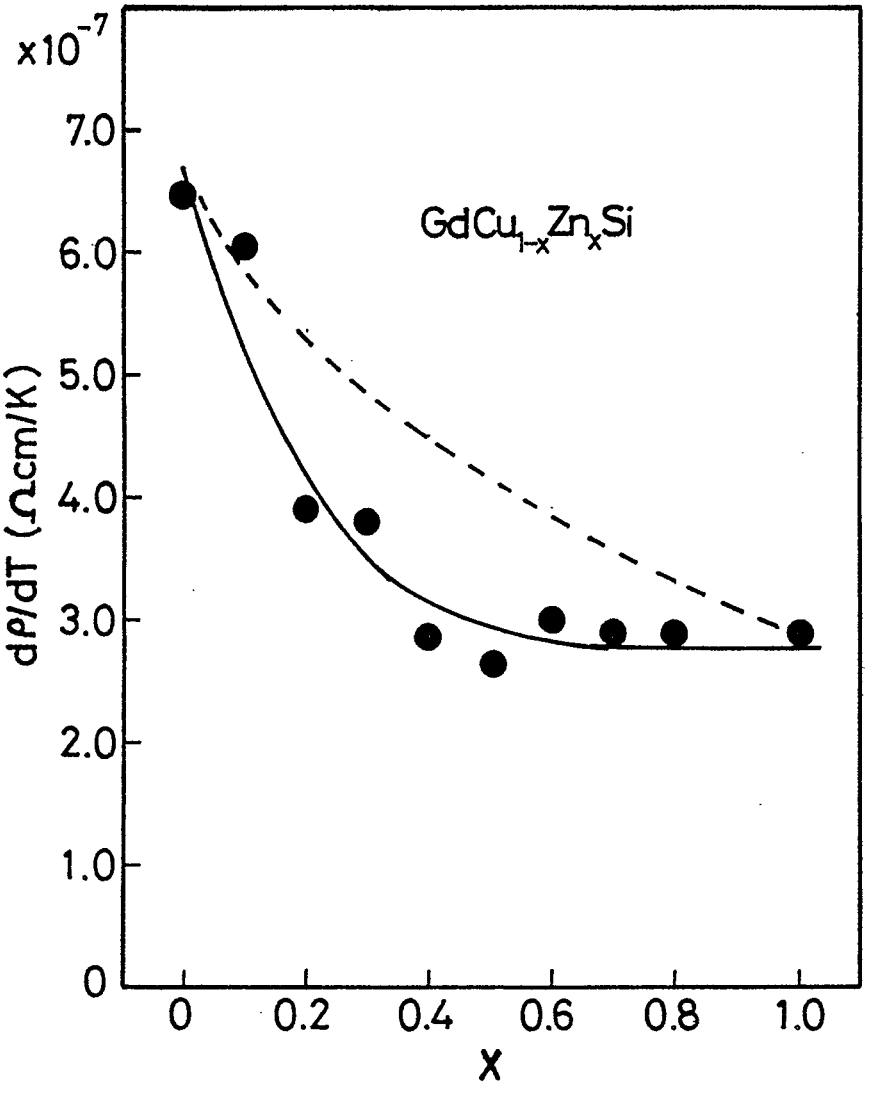

Fig. 42 Compositional dependence of temperature gradient of electrical resistivity for $GdCu_{1-x}Zn_xSi$ in the paramagnetic region.

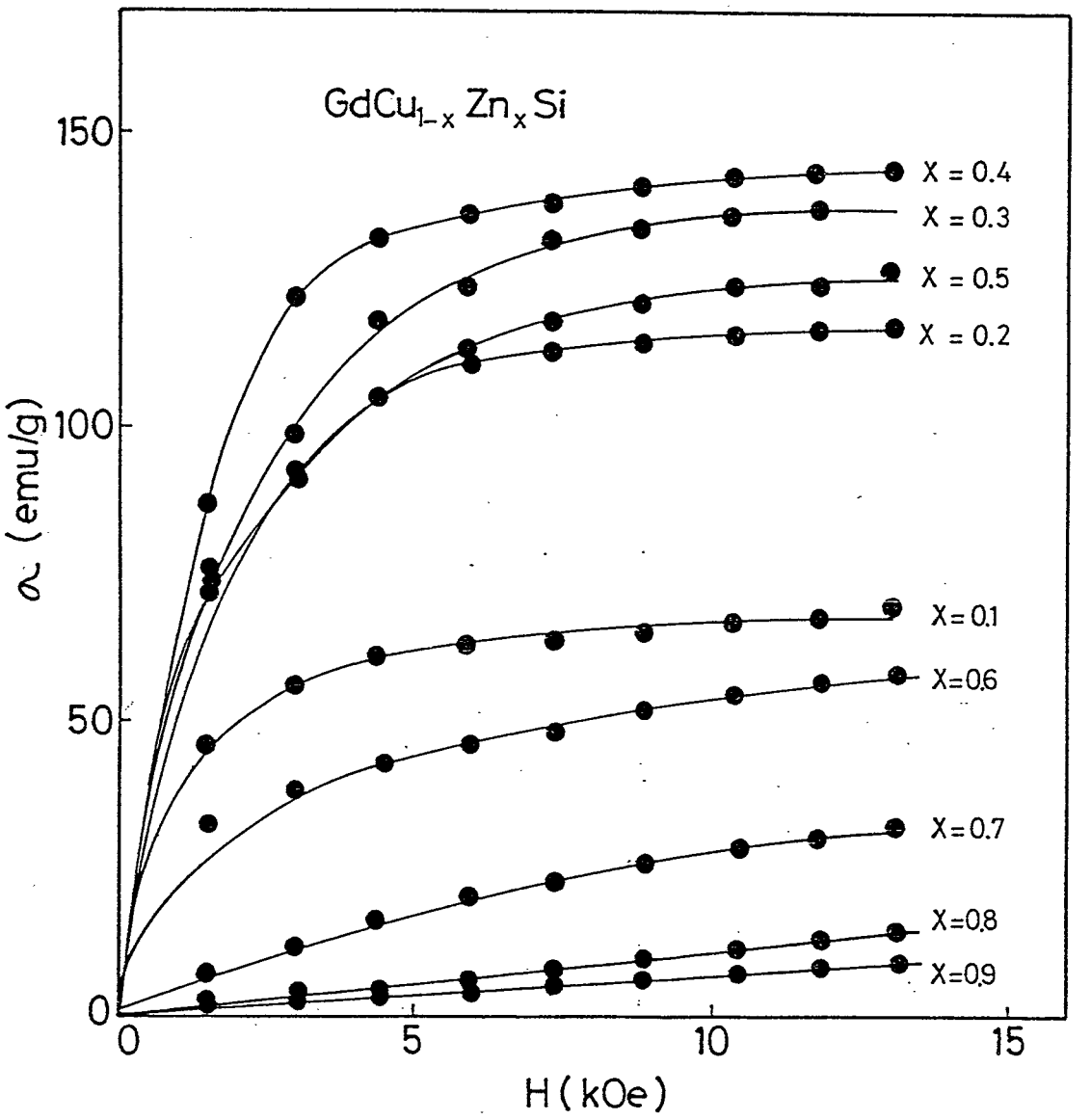

Fig. 43 Magnetization versus magnetic field for $GdCu_{1-x}Zn_xSi$ compounds.

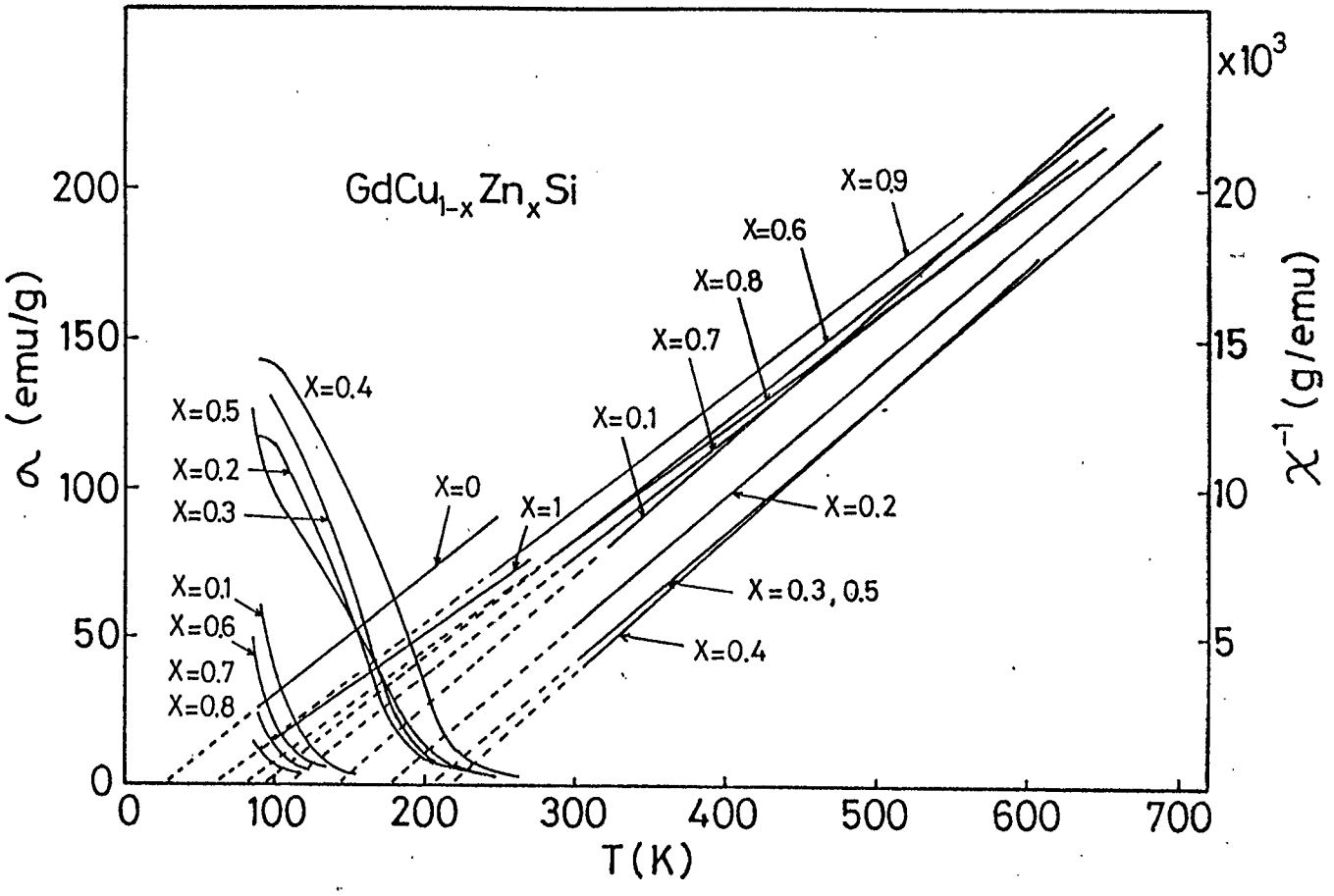

Fig. 44 Temperature dependences of magnetization and inverse magnetic susceptibility of $GdCu_{1-x}Zn_xSi$ compounds.

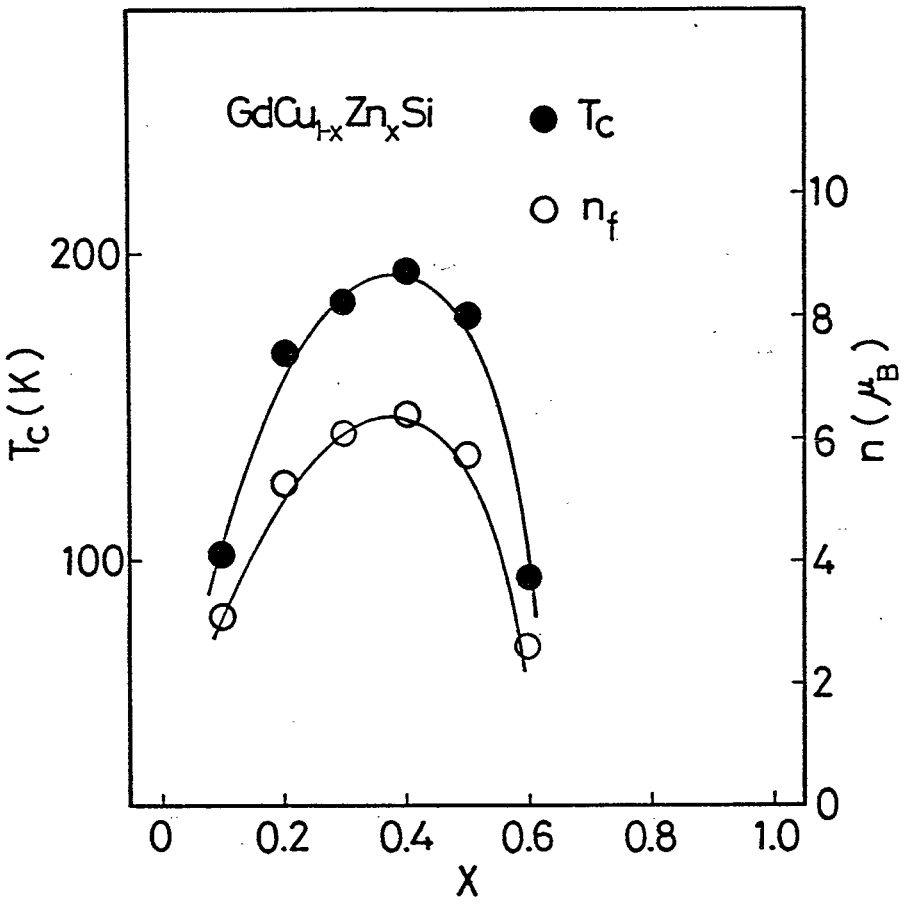

Fig. 45 Ferromagnetic moments, n_f, and Curie temperature, T_c, versus composition x of $GdCu_{1-x}Zn_xSi$.

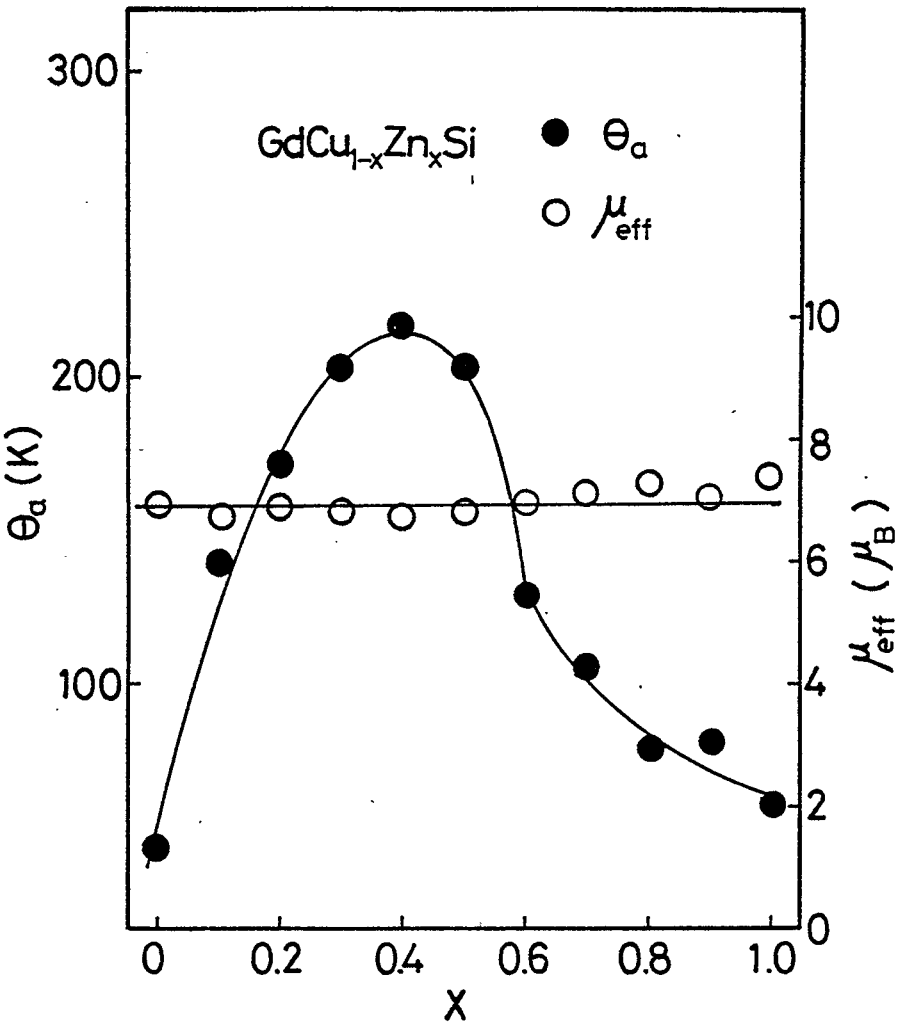

Fig. 46 Effective magnetic moment, μ_{eff}, and paramagnetic Curie temperature, θ_a, versus composition x of $GdCu_{1-x}Zn_xSi$.

are ferromagnetic.

The magnetic parameters of $GdCu_{1-x}Zn_xSi$ compounds are summarized in Table 9.

Table 9 Lattice constants and magnetic parameters of $GdCu_{1-x}Zn_xSi$

x	Lattice constants a (10^{-1}nm)	c (10^{-1}nm)	T_c (K)	n_f (μ_B)	Θ_a (K)	μ_{eff}(μ_B)
x=0	4.178	3.781			26	6.94
x=0.1	4.172	3.797	102	3.12	140	6.73
x=0.2	4.178	3.813	168	5.24	175	6.79
x=0.3	4.176	3.831	164	6.11	203	6.80
x=0.4	4.179	3.838	195	6.40	217	6.71
x=0.5	4.176	3.861	180	5.72	203	6.82
x=0.6	4.172	3.930	94	2.59	129	6.98
x=0.7	4.178	3.910			106	7.12
x=0.8	4.171	3.943			80	7.31
x=0.9	4.163	3.961			82	7.01
x=1.0	4.163	4.000			61	7.41

3-8 Preparation and magnetic and electrical properties of $DyCu_{1-x}Zn_xSi$ ($0 \leq x \leq 1$)

The pseudo-ternary $DyCu_{1-x}Zn_xSi$ compounds were prepared in the same way as in case of $GdCu_{1-x}Zn_xSi$ compounds (87).

The crystal structure of these compounds was the hexagonal AlB_2-type. The lattice constants are shown in Fig. 47. Lattice constants decreased linearly with increasing the compositional parameter x.

The temperature dependence of the electrical resistivity, ρ, of these compounds is shown in Fig. 48. increased with increasing temperature. These compounds were metallic. The temperature gradient, $d\rho/dT$ of $DyCu_{1-x}Zn_xSi$ is plotted as a function of composition x in Fig. 49. The $d\rho/dT$ decreased with increasing x.

The temperature dependences of magnetic susceptibility, χ, and χ^{-1} are shown in Fig. 50. These compounds were paramagnetic above 77K. The temperature dependence of χ^{-1} obeyed the Curie-Weiss law.

The effective magnetic moment, μ_{eff}, and paramagnetic Curie temperature, θ_a, are shown in Fig. 51. The μ_{eff} were almost constant over the whole composition range, and agreed well with the calculated value for the Dy^{3+} ion. The values of θ_a were positive and had a peak at x=0.4.

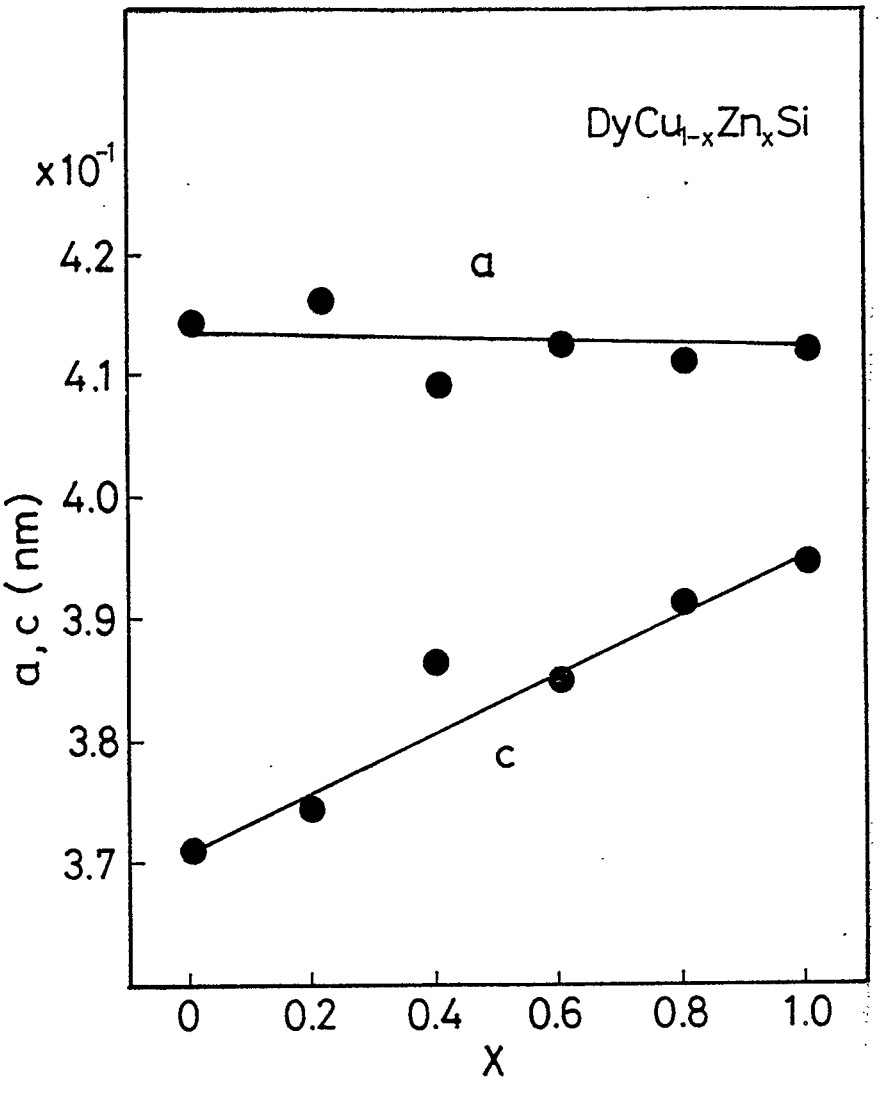

Fig. 47 Lattice constants of $DyCu_{1-x}Zn_xSi$.

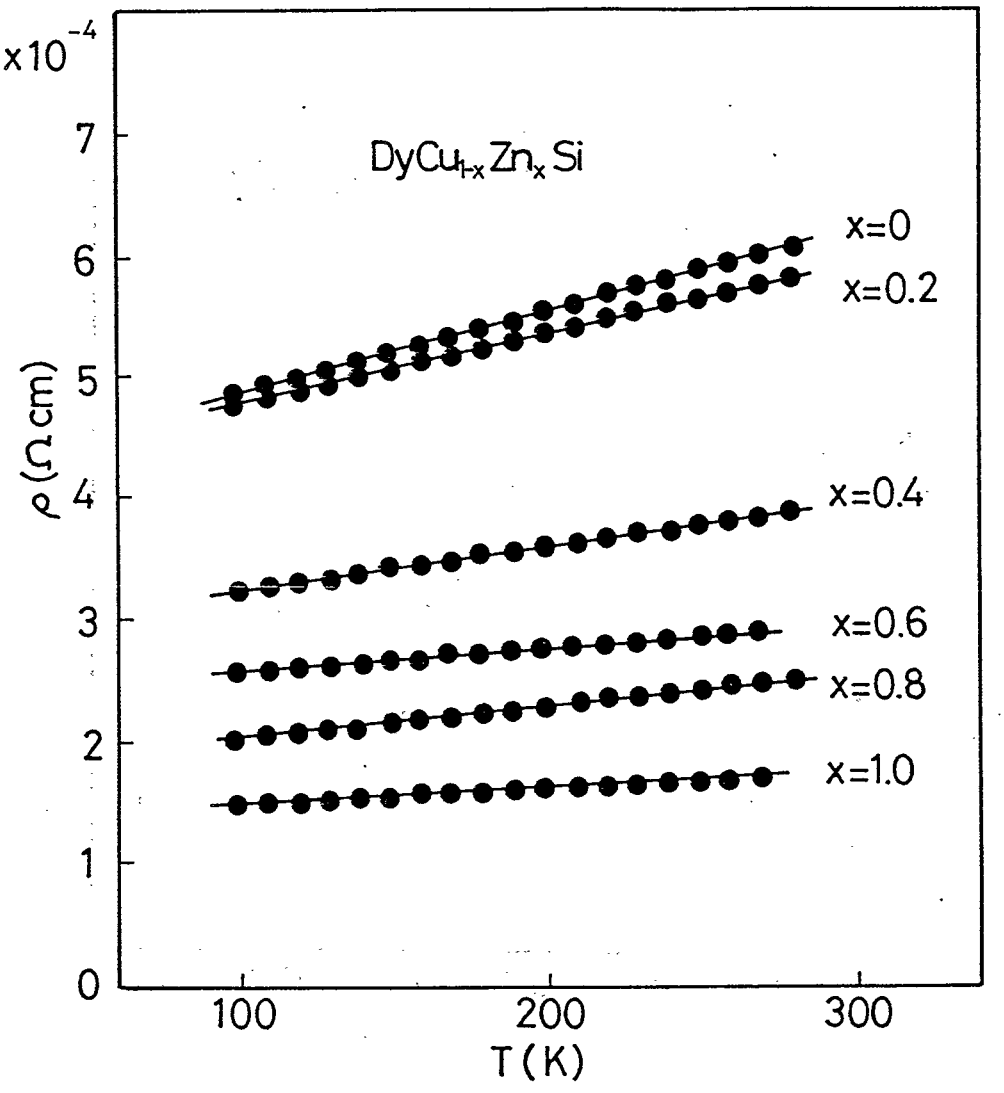

Fig. 48 Temperature dependence of electrical resistivity of $GdCu_{1-x}Zn_xSi$ compounds.

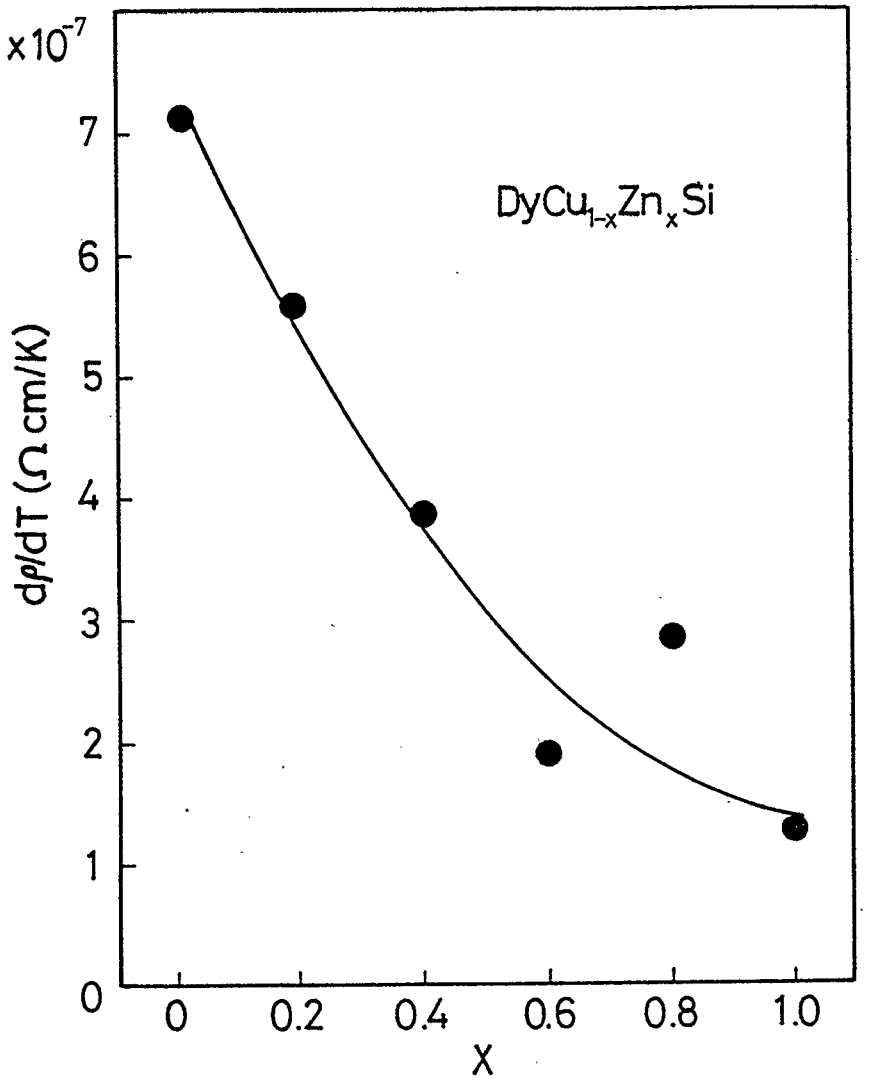

Fig. 49 Temperatue gradient of electrical resistivity of $DyCu_{1-x}Zn_xSi$ versus composition x.

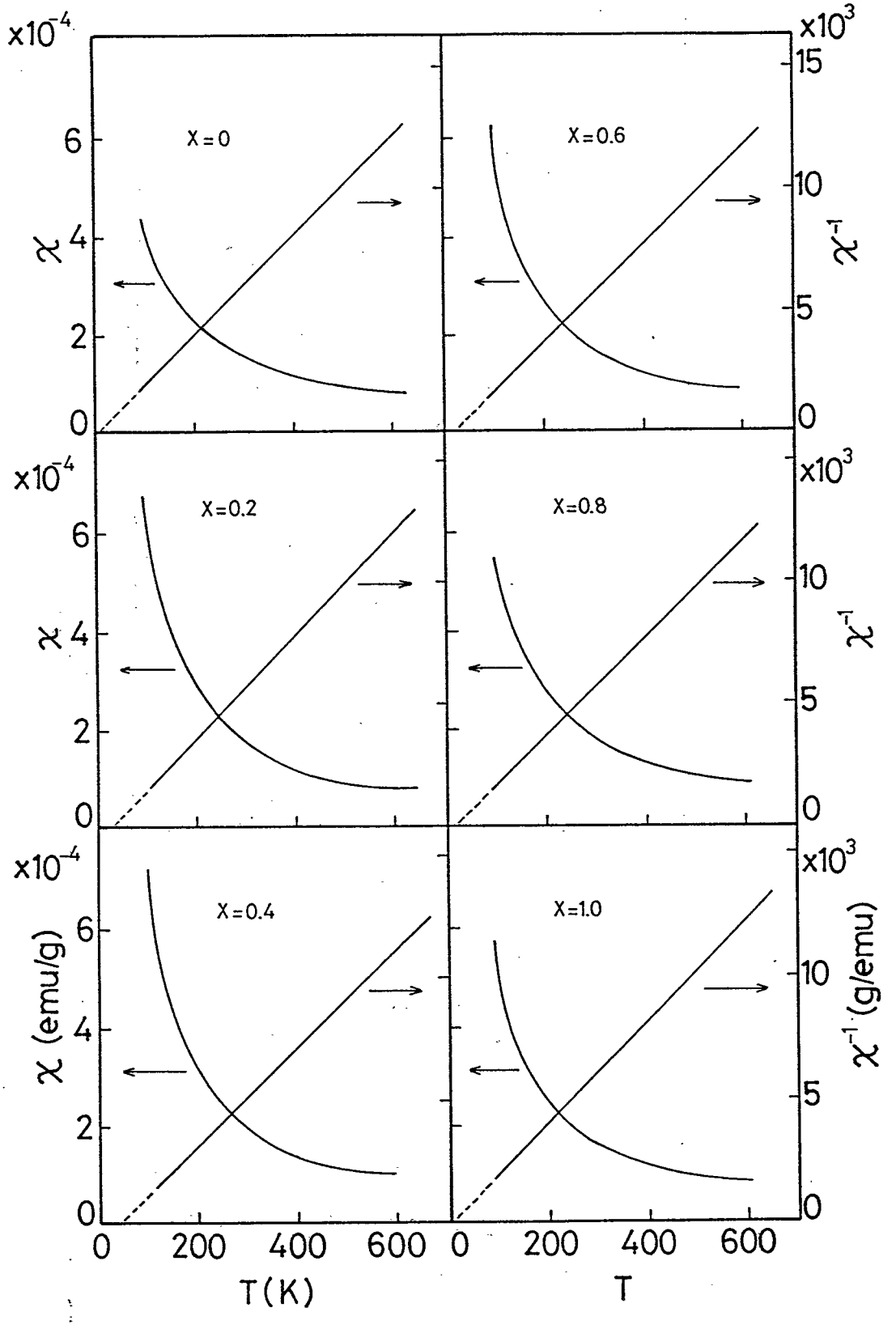

Fig. 50 Temperature dependences of magnetic susceptibility and inverse magnetic susceptibility of $DyCu_{1-x}Zn_xSi$.

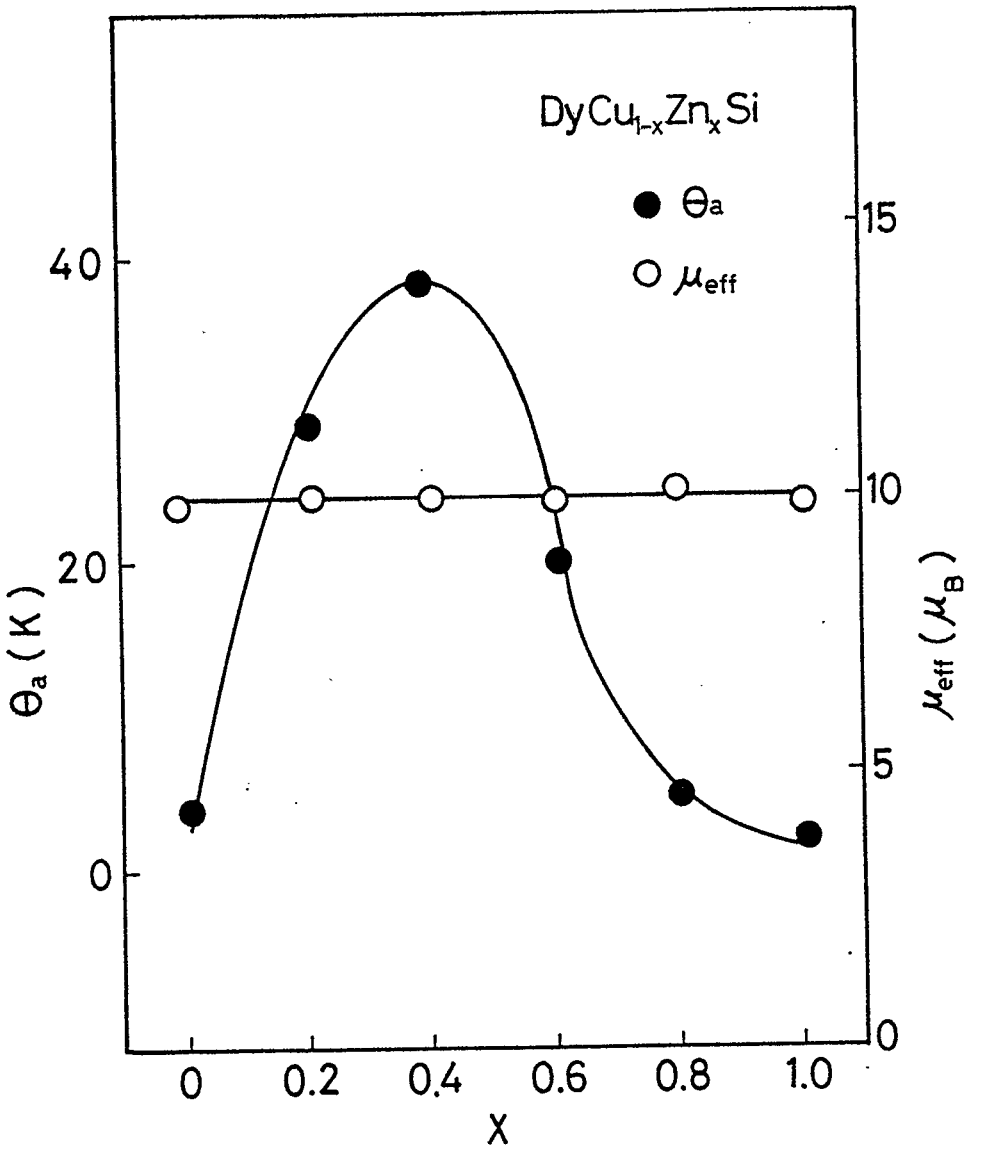

Fig. 51 Effective magnetic moment, μ_{eff}, and paramagnetic Curie temperature, θ_a, versus composition x of $DyCu_{1-x}Zn_xSi$.

3-9 Preparation and magnetic and electrical properties of $HoCu_{1-x}Zn_xSi$ ($0 \leq x \leq 1$) and $NdCu_{0.6}Zn_{0.4}Si$

The pseudo-ternary $HoCu_{1-x}Zn_xSi$ and $NdCu_{0.6}Zn_{0.4}Si$ were prepared in the same way as in case of $GdCu_{1-x}Zn_xSi$ (88).

The crystal structure of these compounds was the hexagonal AlB_2-type. The lattice constants of $HoCu_{1-x}Zn_xSi$ are shown in Fig. 52. Lattice constants decreased with increasing the compositional parameter x. Lattice constants of $NdCu_{0.6}Zn_{0.4}$ Si were a=0.4193 nm and c=0.4026 nm.

The temperature dependence of the electrical resistivity, ρ, of $HoCu_{1-x}Zn_xSi$ is shown in Fig. 53. The linearly increased with increasing temperature, indicating that these compounds were metallic. $NdCu_{0.6}Zn_{0.4}Si$ was also metallic. The $d\rho/dT$ of $HoCu_{1-x}Zn_xSi$ compounds are shown in Fig. 54. The $d\rho/dT$ decreased with increasing x.

The temperature dependences of magnetic susceptibility , χ, and χ^{-1} of $HoCu_{1-x}Zn_xSi$ and $NdCu_{0.6}Zn_{0.4}Si$ are shown in Figs. 55 and 56, respectively. These compounds were paramagnetic above 77K. The temperature dependences of χ^{-1} obeyed the Curie-Weiss law.

The effective magnetic moment, μ_{eff}, and paramagnetic Curie temperature, θ_a, of $HoCu_{1-x}Zn_xSi$ are shown in Fig. 57. The values of μ_{eff} were almost constant over all composition, and they agreed well the calculated value for the Ho^{3+} ion. The values of θ_a of $HoCu_{1-x}Zn_xSi$ were positive and had a peak at x=0.4. The μ_{eff} and θ_a of $NdCu_{0.6}Zn_{0.4}Si$ were 3.6 3.6 μ_B and 7K, respectively.

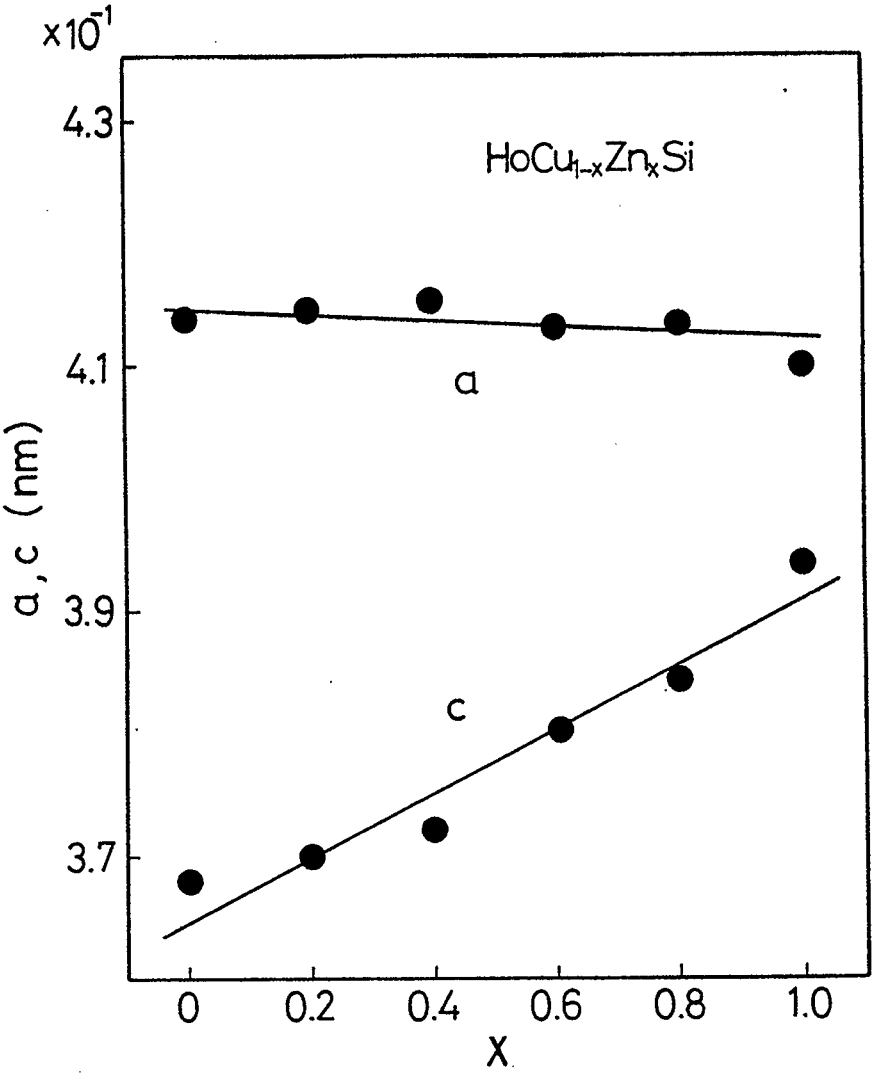

Fig. 52 Lattice constants of $HoCu_{1-x}Zn_xSi$.

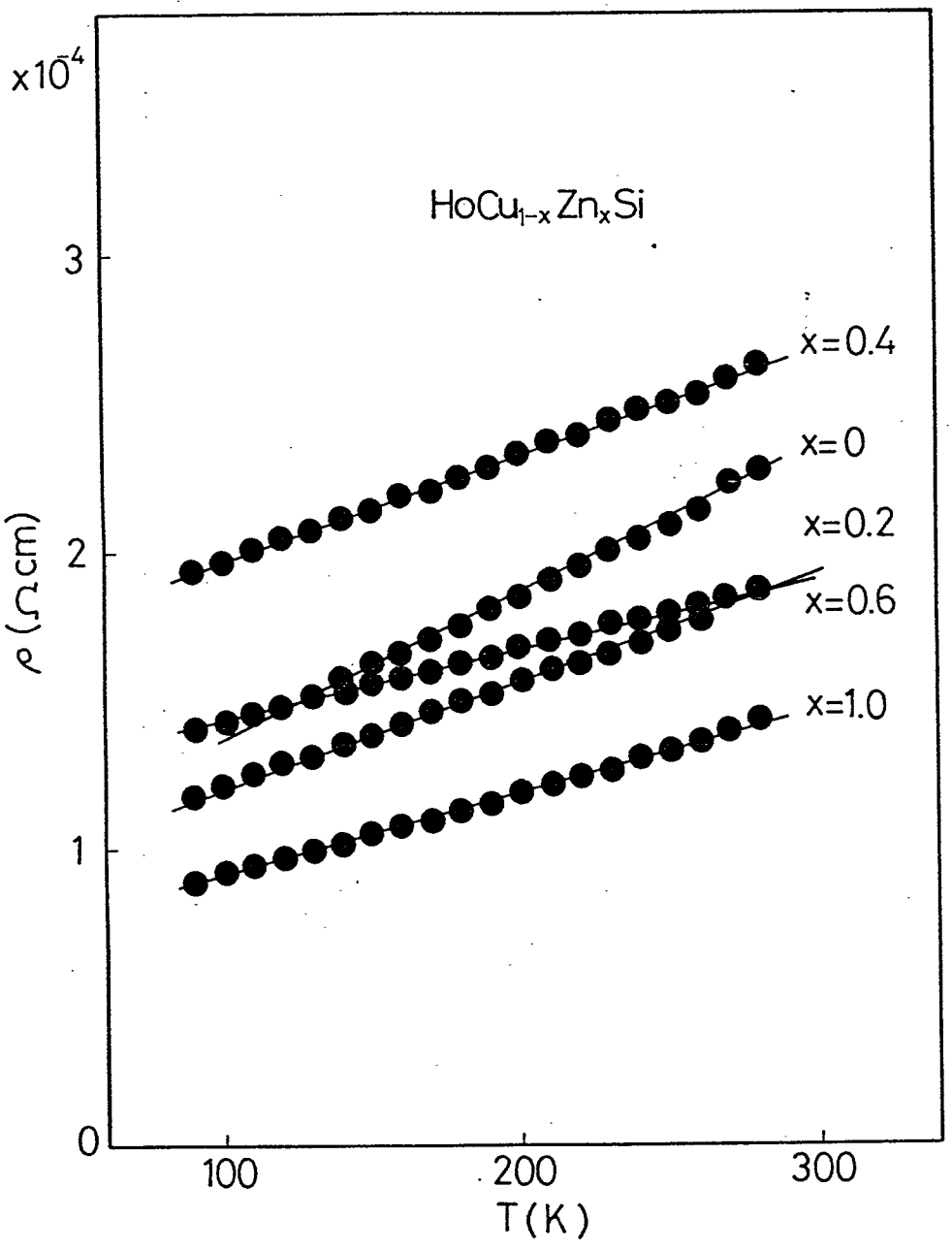

Fig. 53 Temperature dependence of electrical resistivity of $HoCu_{1-x}Zn_xSi$.

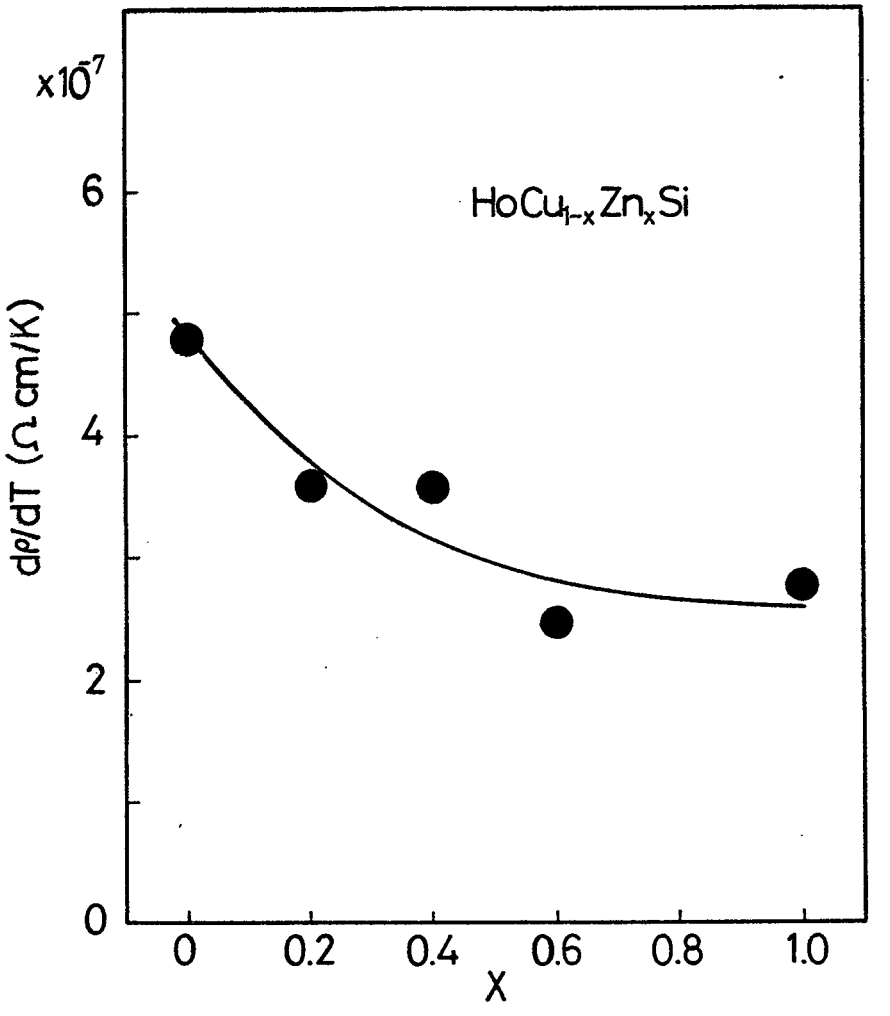

Fig. 54 Temperature gradient of electrical resistivity of $HoCu_{1-x}Zn_xSi$ versus composition x.

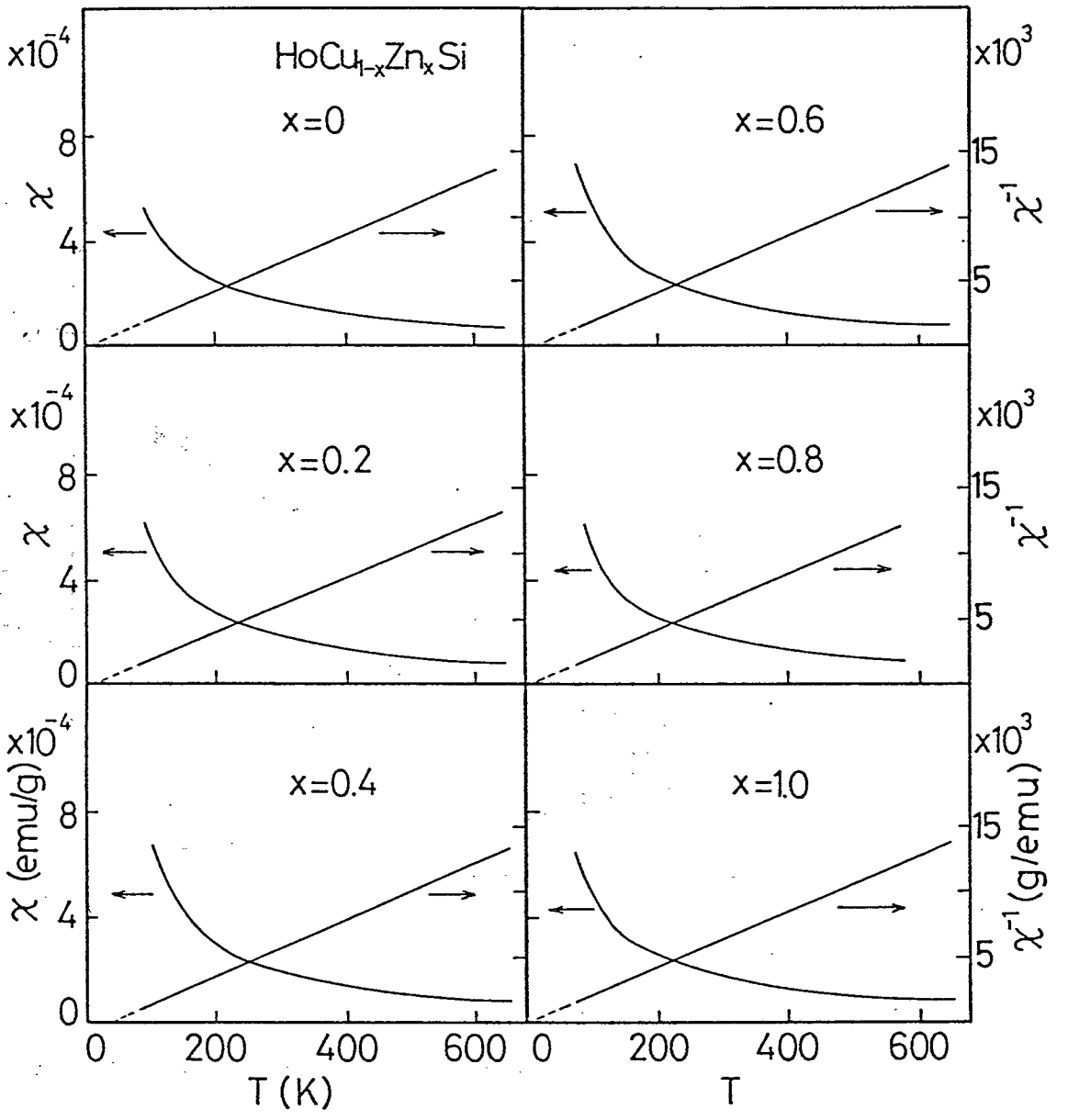

Fig. 55 Temperature dependences of magnetic susceptibility and inverse magnetic susceptibility of $HoCu_{1-x}Zn_xSi$.

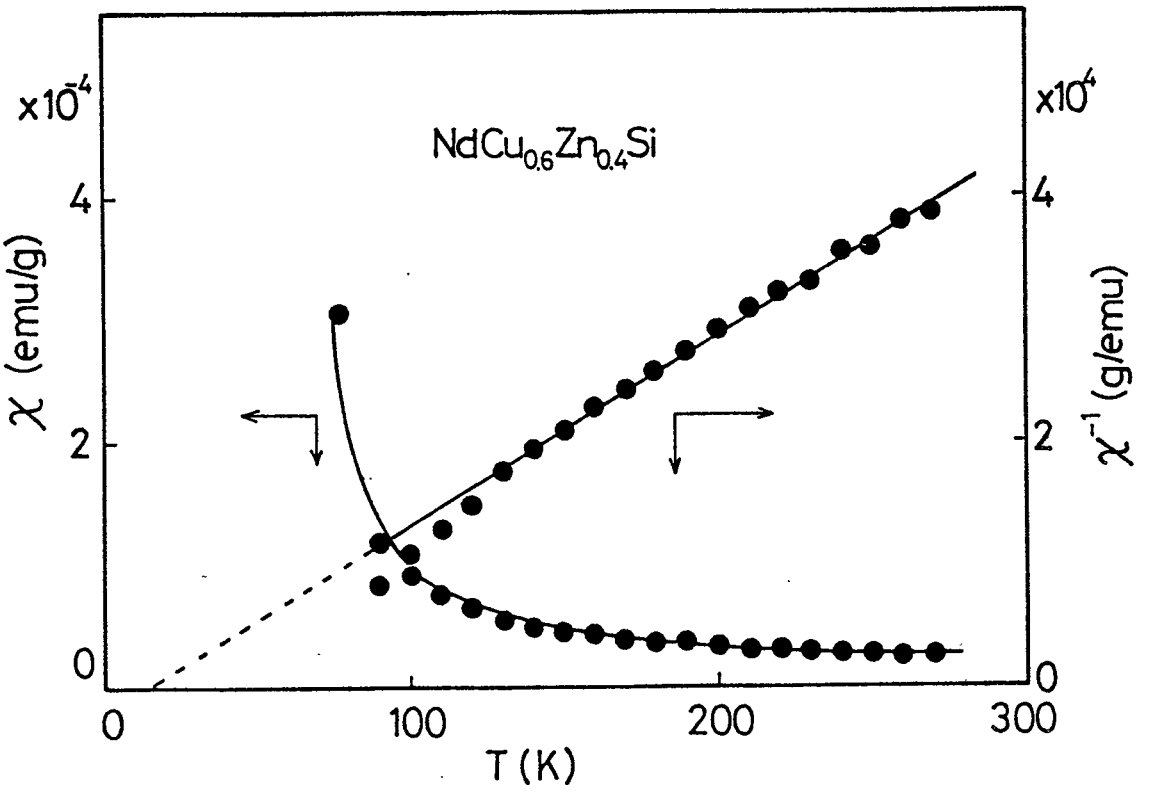

Fig. 56 Temperature dependences of magnetic susceptibility and inverse magnetic susceptibility of $NdCu_{0.6}Zn_{0.4}Si$.

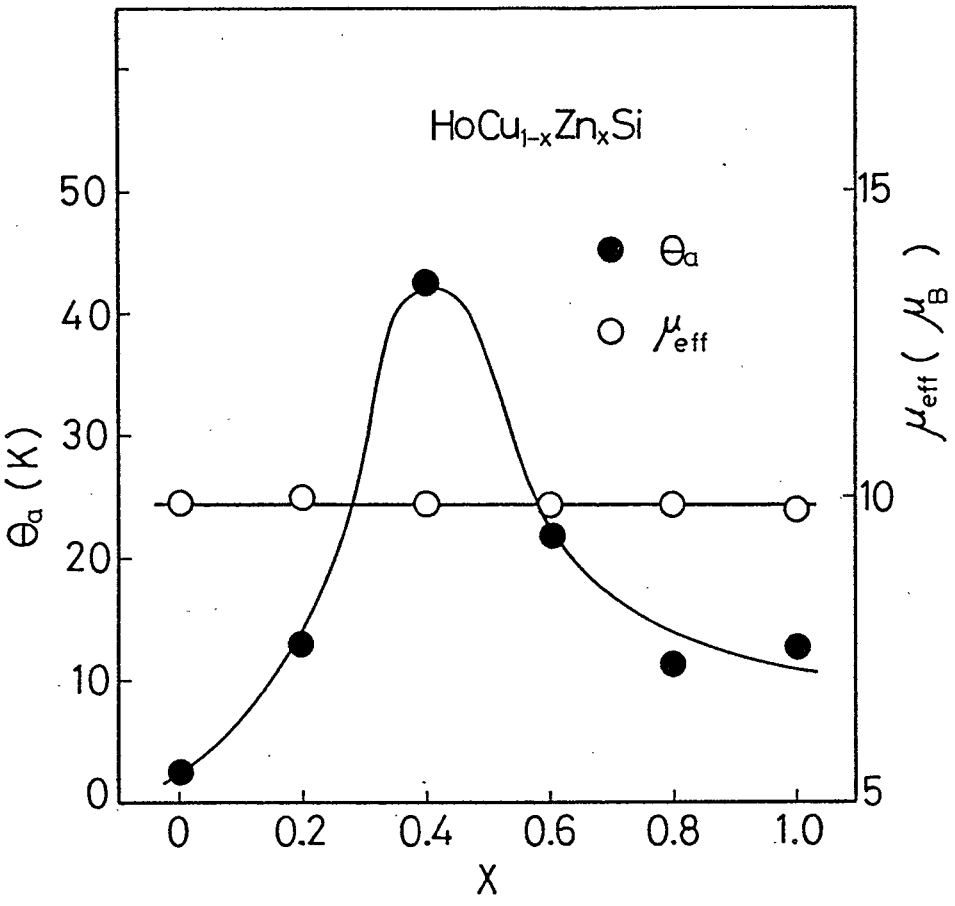

Fig. 57 Effective magnetic moment, μ_{eff}, and paramagnetic Curie temperature, θ_a, versus composition x of $HoCu_{1-x}Zn_xSi$.

3-10 Preparation and magnetic properties of RMn_2Si_2 (R=Y, Nd, Gd) and YNi_2Si_2

RMn_2Si_2 (R=Y, Nd, Gd) were prepared by heating the starting powders at 900 °C for 7 days in the evacuated silica tube. YNi_2Si_2 was prepared by using the cubic anvil-type high pressure apparatus at 1400 °C and 1.0 GPa for 1 hr.

The X-ray powder diffraction patterns of these compounds were completely indexed on the basis of the tetragonal body-centered $ThCr_2Si_2$-type crystal structure (space group: I4/mmm). The crystal structure is shown in Fig. 58. R, Mn and Si atoms occupy the (2a), (4d) and (4e) sites, respectively. Lattice constants and observed interatomic distances are listed in Table 10. These values are compared with sum of corresponding atomic radii. As seen in Table 10, interatomic distances of R-R, R-M, M-M were larger than the sum of corresponding atomic radii, while those of M-Si were much shorter.

The temperature dependences of magnetic susceptibility χ, and χ^{-1} of RMn_2Si_2 (R=Y, Nd, Gd) are shown in Fig. 59. The magnetic parameters are listed in Table 11. These compounds were antiferromagnetic with T_N=514K for YMn_2Si_2, 386K for $NdMn_2Si_2$ and 477K for $GdMn_2Si_2$. Since it is expected that magnetic moments of rare-earth atoms do not order above 200K in these silicides, the antiferromagnetic ordering is due to the magnetic interaction between Mn spins.

The paramagnetic Curie temperatures of RMn_2Si_2 (R=Y, Nd, Gd) were positive, indicating that Mn spins within the layer order ferromagnetically.

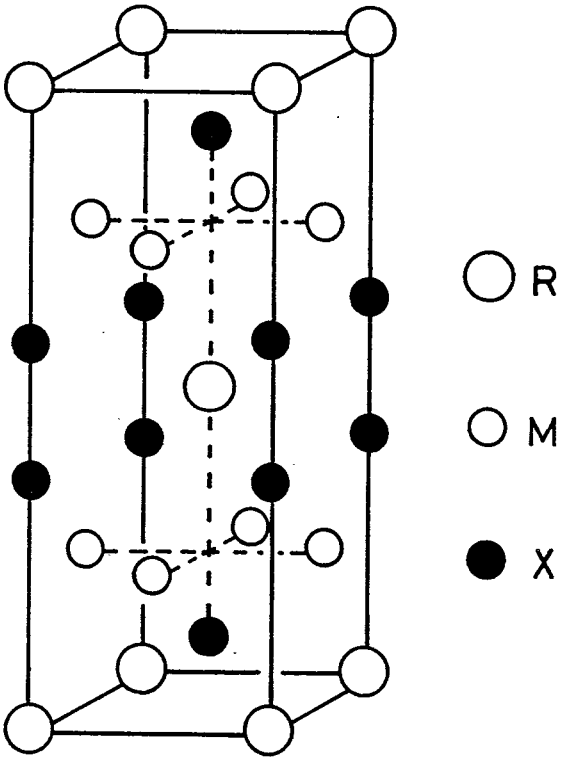

Fig. 58 Crystal structure of RM_2X_2

Table 10 Lattice constants and interatomic distances of RM_2X_2 compounds

RM_2X_2	Lattice constants (nm)	Interatomic distances (nm)					
		R-R	R-M	R-X	M-M	M-X	X-X
YMn_2Si_2	a=0.3929	0.3929	0.3262	0.3082	0.2778	0.2340	0.2667
	c=1.0417	(9.14)	(4.89)	(-1.23)	(6.04)	(-11.0)	(1.01)
$NdMn_2Si_2$	a=0.4015	0.4015	0.3914	0.3142	0.2839	0.2383	0.2694
	c=1.0522	(10.3)	(5.72)	(0.07)	(8.36)	(-9.40)	(2.03)
$GdMn_2Si_2$	a=0.3948	0.3948	0.3278	0.3097	0.2792	0.2351	0.2680
	c=1.0468	(9.67)	(5.40)	(0.75)	(6.55)	(-10.6)	(1.50)
YMn_2Si_2	a=0.3964	0.3964	0.3112	0.3060	0.2803	0.2302	0.2457
	c=0.9599	(10.1)	(2.38)	(-1.91)	(13.0)	(-10.1)	(-6.92)

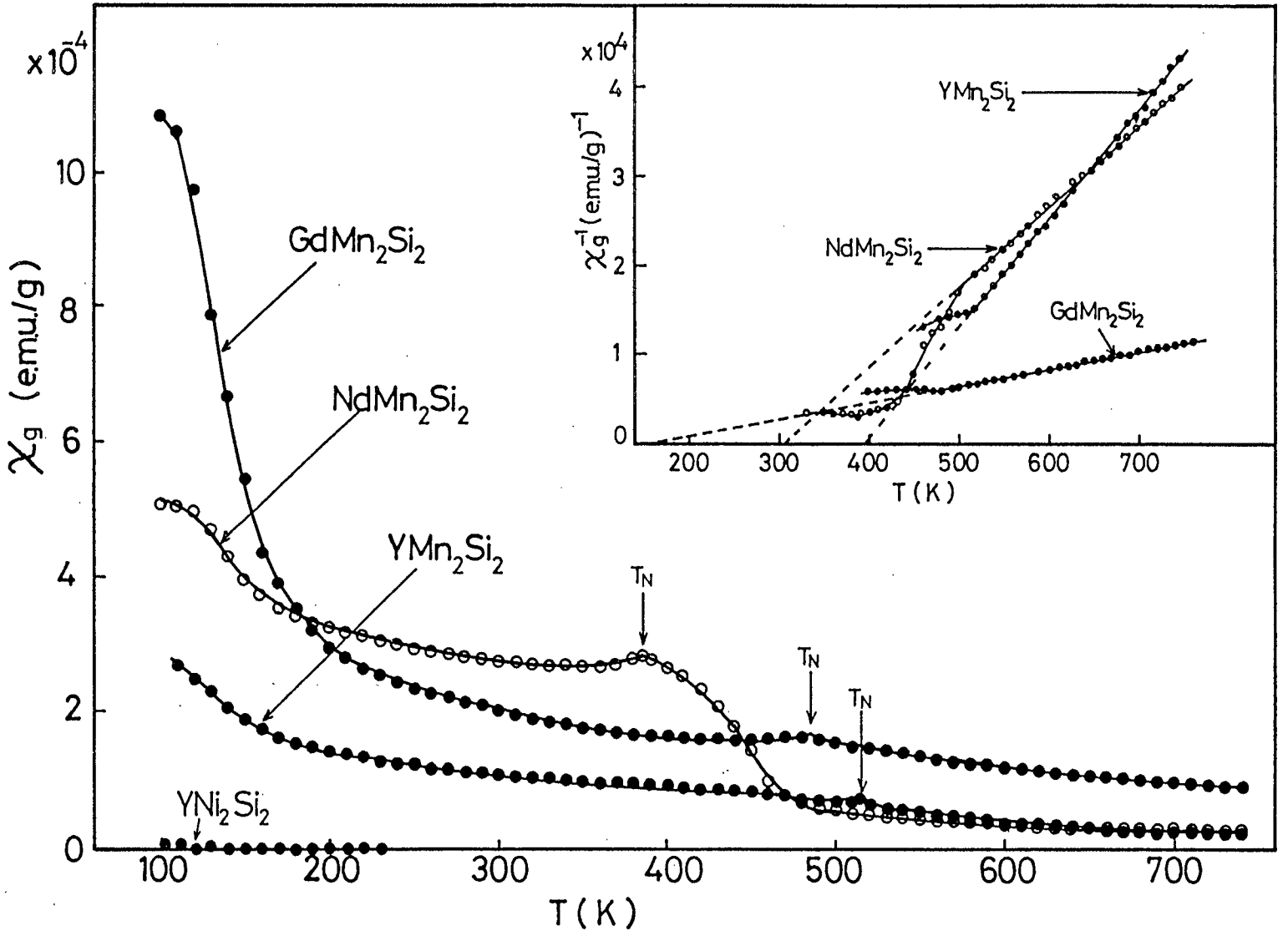

Fig. 59 Temperature dependence of magnetic susceptibility of RMn_2Si_2 (R=Y, Nd, Gd) and YNi_2Si_2, and inverse magnetic susceptibility of RMn_2Si_2.

Table 11 Magnetic parameters of RMn_2Si_2

RMn_2Si_2	T_N (K)	Θ_a (K)	μ_{eff} (μ_B)
YMn_2Si_2	514	395	4.1
$NdMn_2Si_2$	386	303	5.3
$GdMn_2Si_2$	477	162	11.6

The relation between the Néel temperature and the Mn-Mn interatomic distance is shown in Fig. 60. The Néel temperature decreased with increasing the Mn-Mn interatomic distance.

The effective magnetic moments of RMn_2Si_2 (R=Y, Nd, Gd) indicated that one Mn atom had the magnetic moment of about 1.5-2.0 μ_B, which was well corresponded to that for RMnSi.

The magnetic susceptibility of YNi_2Si_2 was independent of temperature, as seen in Fig. 59. It is expected that the 3d shells of Ni atoms are fully occupied by the electrons transfered from Si atoms.

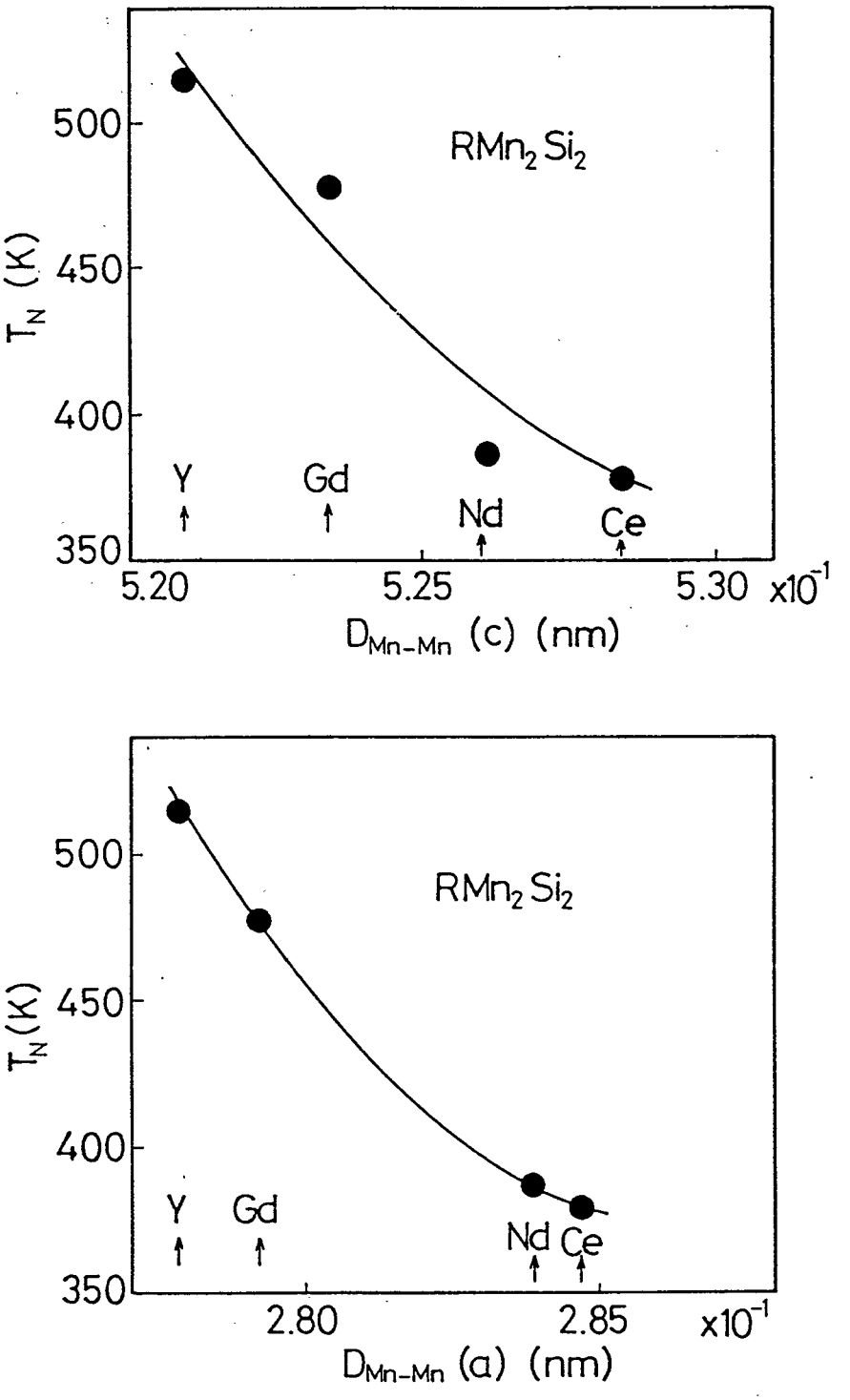

Fig. 60 Relation between Néel temperature and Mn-Mn interatomic distance for RMn_2Si_2. T_N of $CeMn_2Si_2$ was cited from ref. 65.

3-11 Preparation and magnetic properties of $YMn_2(Si_{1-x}Ge_x)_2$ $(0 \leqq x \leqq 1)$

$YMn_2(Si_{1-x}Ge_x)_2$ were prepared by heating the mixed powders of YMn_2Si_2 and YMn_2Ge_2 at 900°C for 7 days in the evacuated silica tube. YMn_2Si_2 and YMn_2Ge_2 were prepared by heating the starting powders at 900°C for 7 days in the evacuated tube, as already mentioned in 3-10.

The X-ray powder diffraction patterns of these compounds were completely indexed on the basis of the tetragonal body-centered $ThCr_2Si_2$-type structure. The lattice constants are plotted as a function of the compositional parameter x in Fig. 61. Lattice constants obeyed the Vegard's law. This result indicated that Ge atoms randomly replaced Si atoms. The lattice constants and observed interatomic distances, which were calculated using z-parameter of 0.375 for Si or Ge (48), are listed in Table 12. These interatomic distances were compared with the sum of corresponding atomic radii. The results are shown in the parenthesis in Table 12. The Mn-X interatomic distances were much shorter.

The temperature dependences of the magnetic susceptibility, χ and χ^{-1} of $YMn_2(Si_{1-x}Ge_x)_2$ are shown in Fig. 62. These compounds were antiferromagnetic with T_N=475K, 456K, 436K and 426K for x=0.2, 0.4, 0.6 and 0.8, respectively. The magnetic parameters of $YMn_2(Si_{1-x}Ge_x)_2$ are listed in Table 13.

The relation between the Néel temperature and the Mn-Mn interatomic distance for $YMn_2(Si_{1-x}Ge_x)_2$ is shown in Fig. 63 together with Néel temperatures for other RMn_2Si_2 (R=Nd, Gd) (62-66). $D_{Mn-Mn}(a)$ and $D_{Mn-Mn}(c)$ denote the Mn-Mn distances for intralayer and interlayer, respectively. The Néel

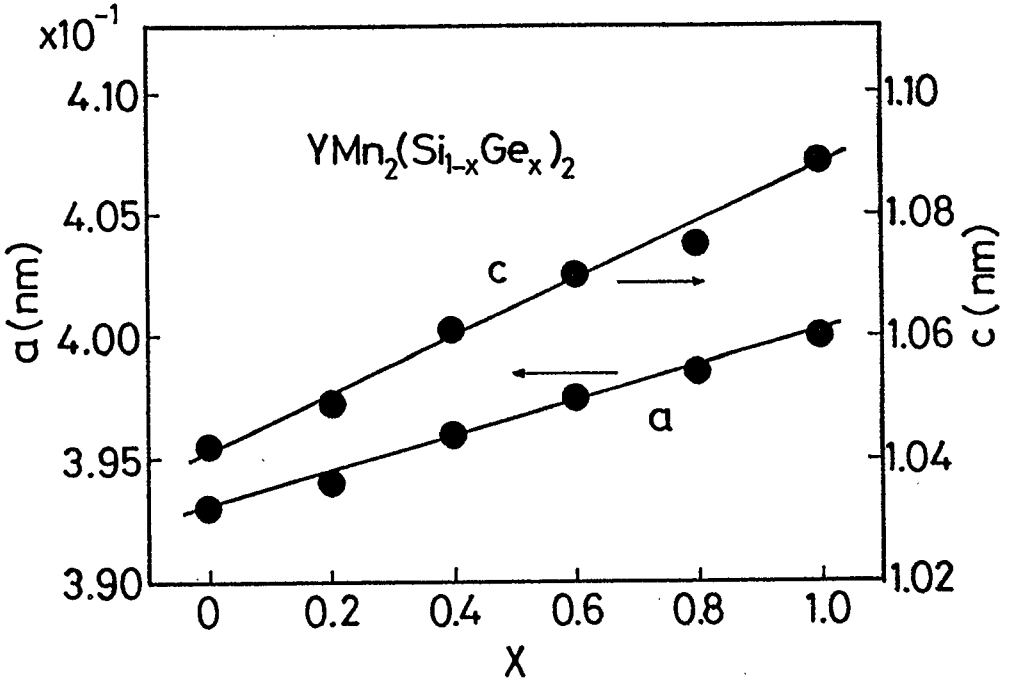

Fig. 61 Lattice constants of $YMn_2(Si_{1-x}Ge_x)_2$.

Table 12 Lattice constants and interatomic distances of $YMn_2(Si_{1-x}Ge_x)_2$

x	Lattice constants (nm)	Interatomic distances (nm) R-R	R-M	R-X	M-M	M-X	X-X
x=0	a=0.3929	0.3929	0.3262	0.3068	0.2778	0.2357	0.2604
	c=1.0417	(9.14)	(4.89)	(-1.66)	(6.04)	(-10.4)	(-1.34)
x=0.2	a=0.3940	0.3940	0.3281	0.3079	0.2786	0.2367	0.2623
	c=1.0493	(9.44)	(5.49)	(-1.62)	(6.34)	(-10.4)	(-1.38)
x=0.4	a=0.3960	0.3960	0.3310	0.3098	0.2800	0.2383	0.2652
	c=1.0609	(10.0)	(6.42)	(-1.33)	(6.88)	(-10.1)	(-1.04)
x=0.6	a=0.3975	0.3975	0.3332	0.3113	0.2811	0.2395	0.2675
	c=1.0698	(10.4)	(7.14)	(-1.19)	(7.28)	(-9.94)	(-0.94)
x=0.8	a=0.3985	0.3985	0.3345	0.3122	0.2818	0.2403	0.2687
	c=1.0749	(10.7)	(7.57)	(-1.21)	(7.55)	(-9.99)	(-1.20)
x=1*	a=0.3995	0.3995	0.3376	0.3136	0.2825	0.2417	0.2722
	c=1.0886	(11.0)	(8.55)	(-1.09)	(7.82)	(-9.82)	(-0.68)

* reference 56

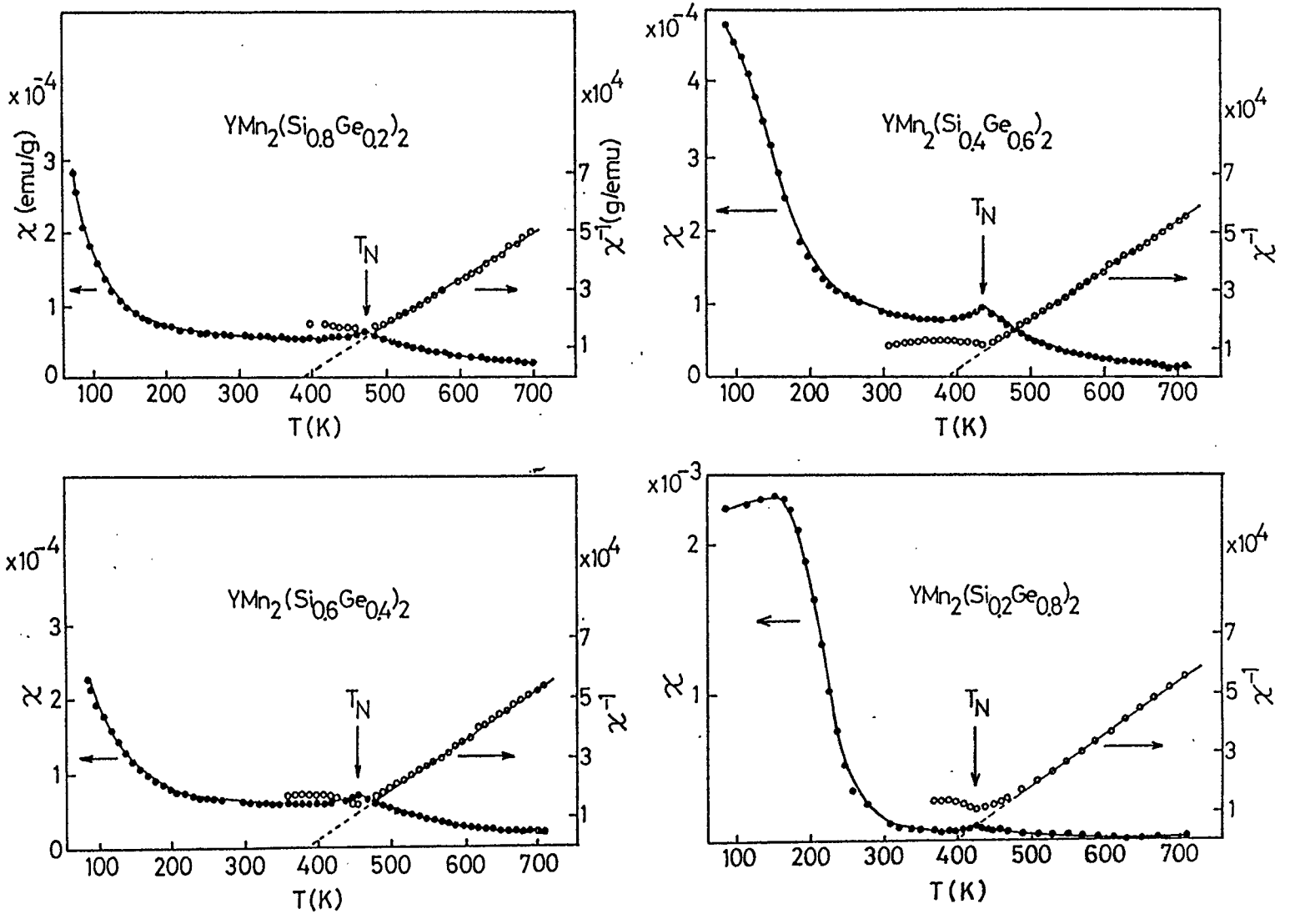

Fig. 62 Temperature dependence of magnetic susceptibility and inverse magnetic susceptibility of $YMn_2(Si_{1-x}Ge_x)_2$.

Table 13 Magnetic parameters of $YMn_2(Si_{1-x}Ge_x)_2$

x	T_N (K)	Θ_a (K)	μ_{eff} (μ_B)
x=0	514	395	4.10
x=0.2	475	385	3.72
x=0.4	456	383	3.64
x=0.6	436	387	3.64
x=0.8	426	399	3.61

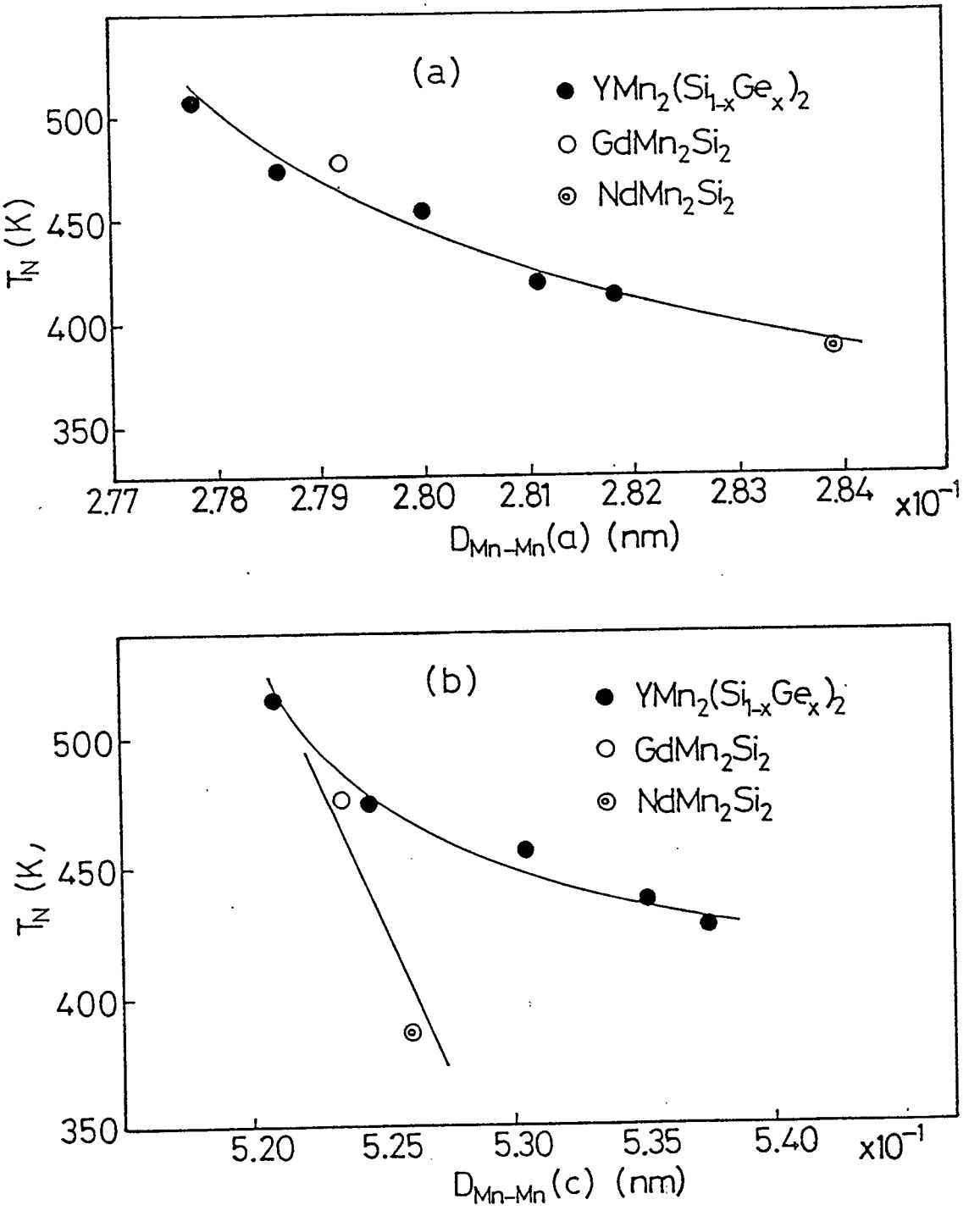

Fig. 63 Relation between Néel temperature and Mn-Mn interatomic distance for $YMn_2(Si_{1-x}Ge_x)_2$ and RMn_2Si_2.

temperature decreased with increasing the Mn-Mn interatomic distance with the curvature.

As seen in Fig. 63 (b), two curves were obtained depending upon the kinds of rare-earth elements. One curve corresponds to the case in which R had no magnetic moment, and the other corresponds to the case in which R had the magnetic moments. The Néel temperature decreased more rapidly when R had the magnetic moment.

The paramagnetic Curie temperatures θ_a of $YMn_2(Si_{1-x}Ge_x)_2$ were positive. The θ_a are plotted as a function of the Mn-Mn interatomic distance in Fig. 64, together with θ_a for RMn_2Si_2 (R=Nd, Gd) (62-66). It was found that θ_a of $YMn_2(Si_{1-x}Ge_x)_2$ were almost constant, but θ_a of RMn_2Si_2 (R=Nd, Gd) decreased with increasing the magnetic moment of R^{3+} ions.

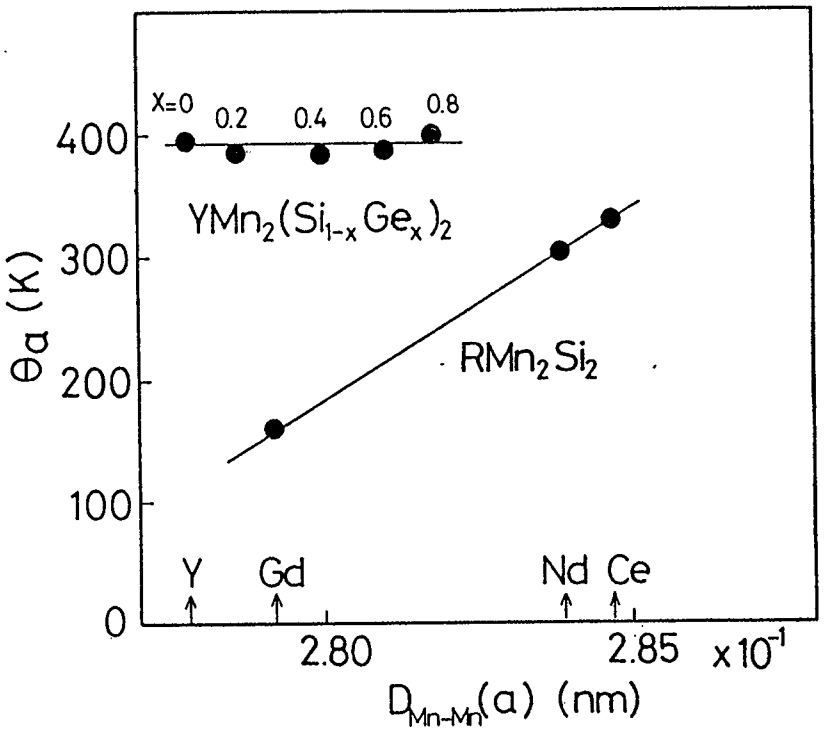

Fig. 64 Relation between paramagnetic Curie temperature and Mn-Mn interatomic distance for $YMn_2(Si_{1-x}Ge_x)_2$ and RMn_2Si_2.

CHAPTER 4

DISCUSSION

4-1 Crystal structures of RMSi compounds

The crystal structures of RMSi compounds are mainly either the tetragonal PbFCl-type or the hexagonal AlB_2-type depending on the kinds of transition metals. The former was for M=Mn, Fe, Co (77,79,84), and the latter was for M=Ti, Cu, Zn (56,76,80,81). The change in the crystal structure of the RMSi compounds is thought to be due to the change in both atomic radii of transition metal atoms and the concentration of conduction electrons in the conduction bands of the compounds. However, the qualitative discussion of the polymorphism of thorium disilicides given by Brown (89) was not applicable to the ternary silicides under the present investigation.

The volumes of the first-row transition metal atoms and the volumes per formula unit of the GdMSi compounds are shown in Fig. 65. It can be seen that the AlB_2-type structure of RMSi is corresponded to the larger volume of transition metals, and the PbFCl-type structure is obtained for transition metals with small volumes. These results can be understood by considering the crystal structures of RMSi compounds. In the AlB_2-type structure, in case of GdMSi, the gadolinium atoms occupy the centers of the hexagonal prisms formed by the transition metal and silicon atoms. The prism formed by titanium, copper

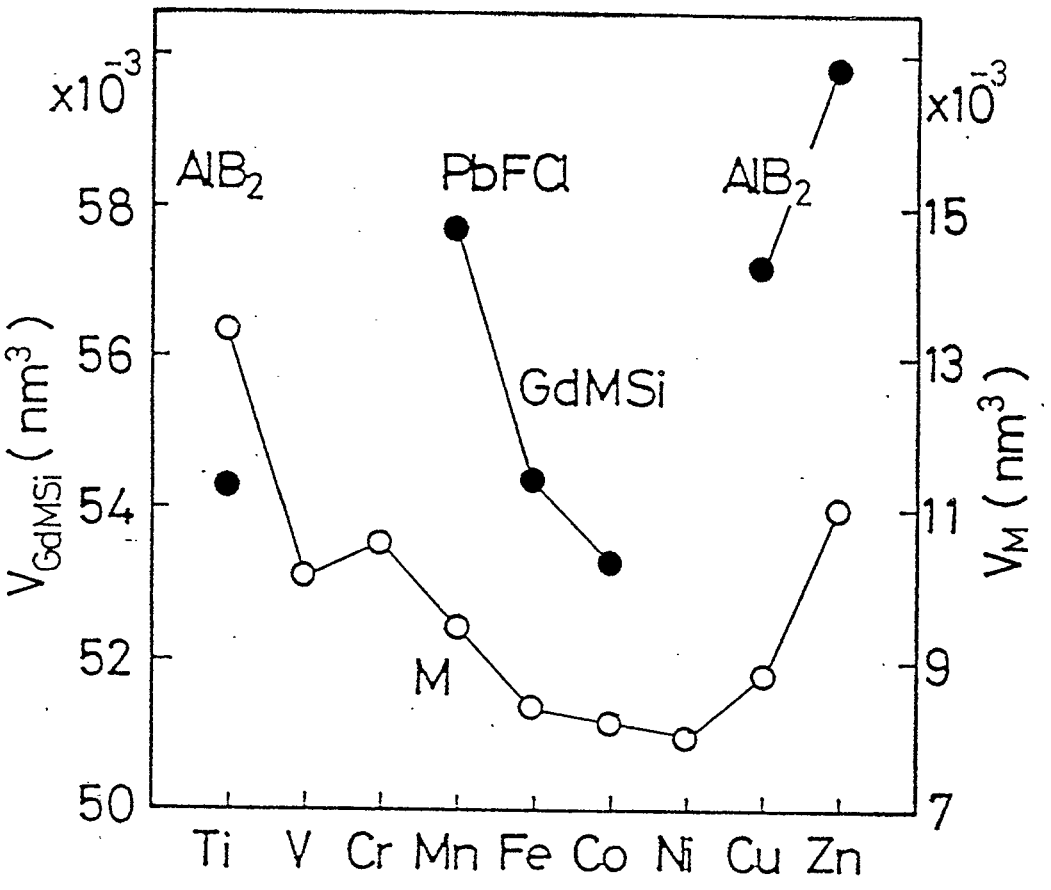

Fig. 65 Volumes of the transition metals and voluemes per formula unit of the GdMSi compounds.

and zinc atoms are large enough to accomodate the gadolinium atoms. However, the prisms formed by transition metals with small atomic radii cannot accomodate the large gadolinium atoms. Therefore, the different type of crystal structure is formed when the radius of transition metal atom is small.

The crystallographic relation between the AlB_2- and PbFCl-type structure is derived from the hexagonal AlB_2-type crystal structure after the following procedure. The atoms indicated by shaded circles in Fig. 66(a) rotate by 180 degrees about the [0001] axis and then move by a distance of c/2 along the [0001] direction. In the PbFCl-type structure, the second layer, which consists of rare-earth atoms lying along the <100> axes, is rearranged such that the atoms are prevented from overlapping those in the first and third layers by moving by a distance of a/2 along the <100> directions.

The lattice constants and ratio c/a of GdMSi are plotted against the atomic radii of the transition metals in Fig. 67. It can be seen that there was little change in the lattice parameter a of GdMSi compounds having both structure types except GdTiSi. The lattice constant a of GdTiSi, in which the atomic radius of titanium is 11% greater than that of silicon, was smaller than those of the other AlB_2-type compounds. The lattice constants c increased linearly with increasing atomic radii of the transition metals, indicating that the interlayer separation was increasing.

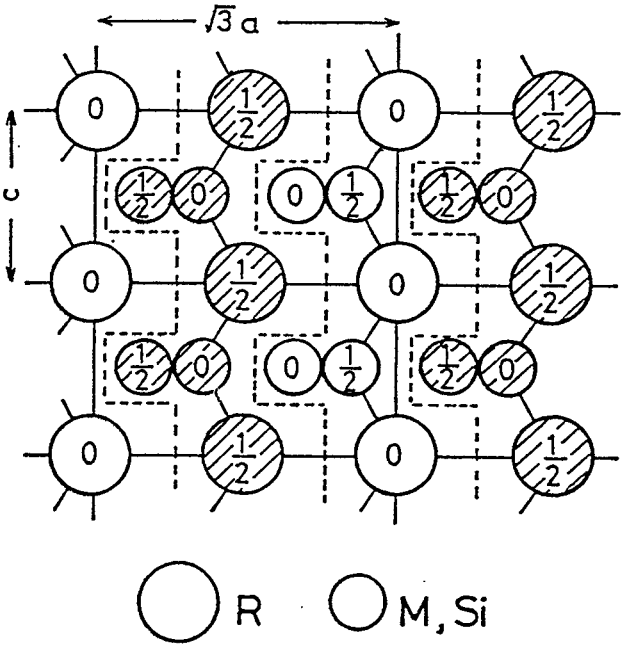

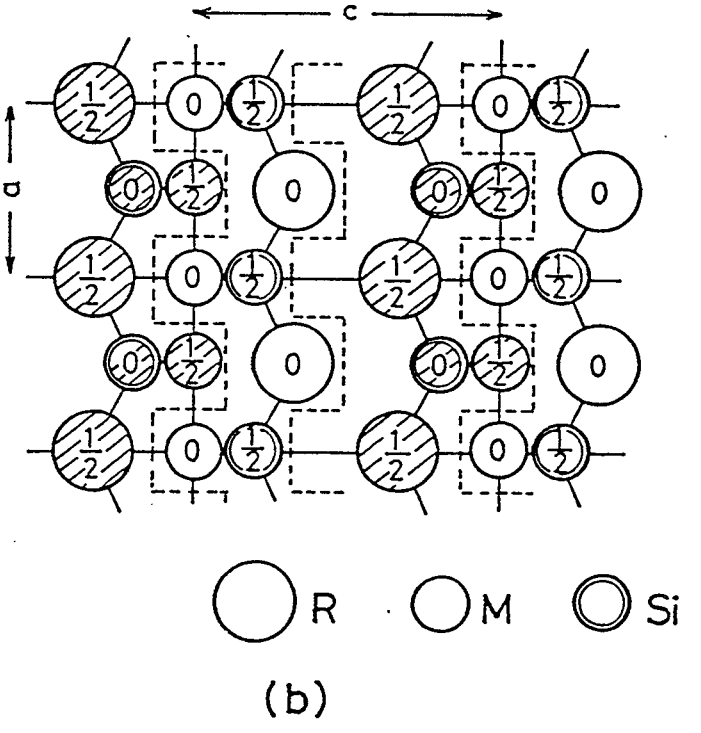

Fig. 66 Crystallographic relation between (a) the AlB_2-type and (b) the PbFCl-type structures.

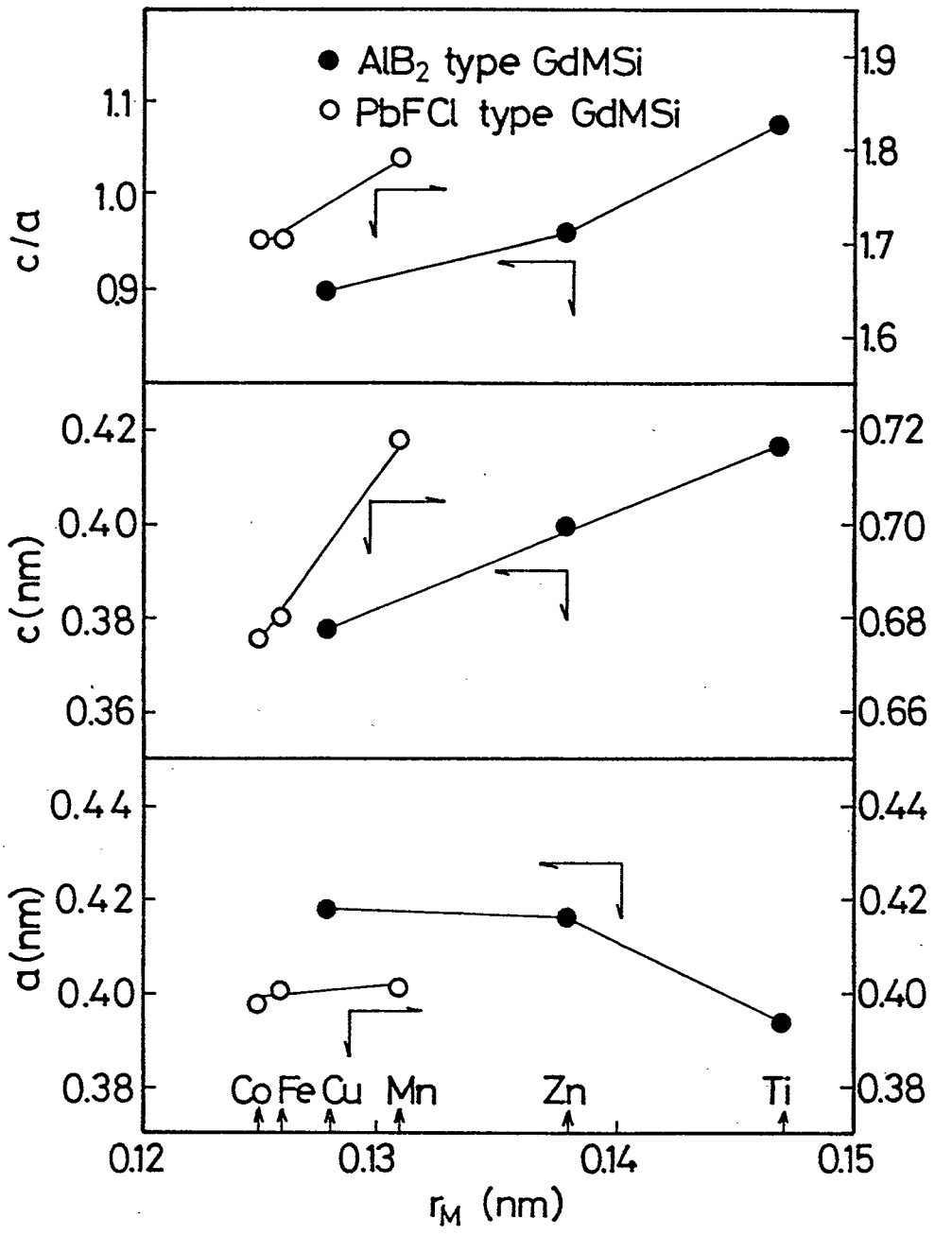

Fig. 67 Lattice constants and the ratio c/a versus the atomic radii of the transition metals.

The electrical resistivity of GdCoSi with the PbFCl-type structure was compared with that of GdCuSi with the AlB_2-type structure in Fig. 68. The slope for GdCoSi was 57×10^{-7} $\Omega cm K^{-1}$, which is less by about one order of magnitude than the slope for GdCuSi. This result suggests that there are more conduction electrons in the conduction band of GdCuSi than those of GdCoSi. This conclusion is supported by the magnetometric data for RMnSi and RCoSi compounds in which electron transfer from silicon atoms to transition metal atoms occurred and resulted in a lower concentration of conduction electrons in RMSi compounds with the PbFCl-type structure.

The crystal structure of NdNiSi was the tetragonal $ThSi_2$-type (78). This structure is similar to the AlB_2-type structure. In Fig. 69, the crystallographic relation between the $ThSi_2$-type and the AlB_2-type structures is shown. In the $ThSi_2$-type structure, three dimensional network of silicon and transition metal atoms is formed. The $ThSi_2$-type structure is derived from the AlB_2-type structure by moving the shaded circles along the $[2\bar{1}\bar{1}0]$ direction by a distance of a/2, then moving by a distance of c/2 along the [0001] direction.

The crystal structures of HoCoSi and GdNiSi were not related with the known structure types, but the X-ray powder diffraction patterns of these compounds could be indexed on the basis of the hexagonal lattice. Lattice constants were two times larger than those for the compounds with the hexagonal AlB_2-type structure. This

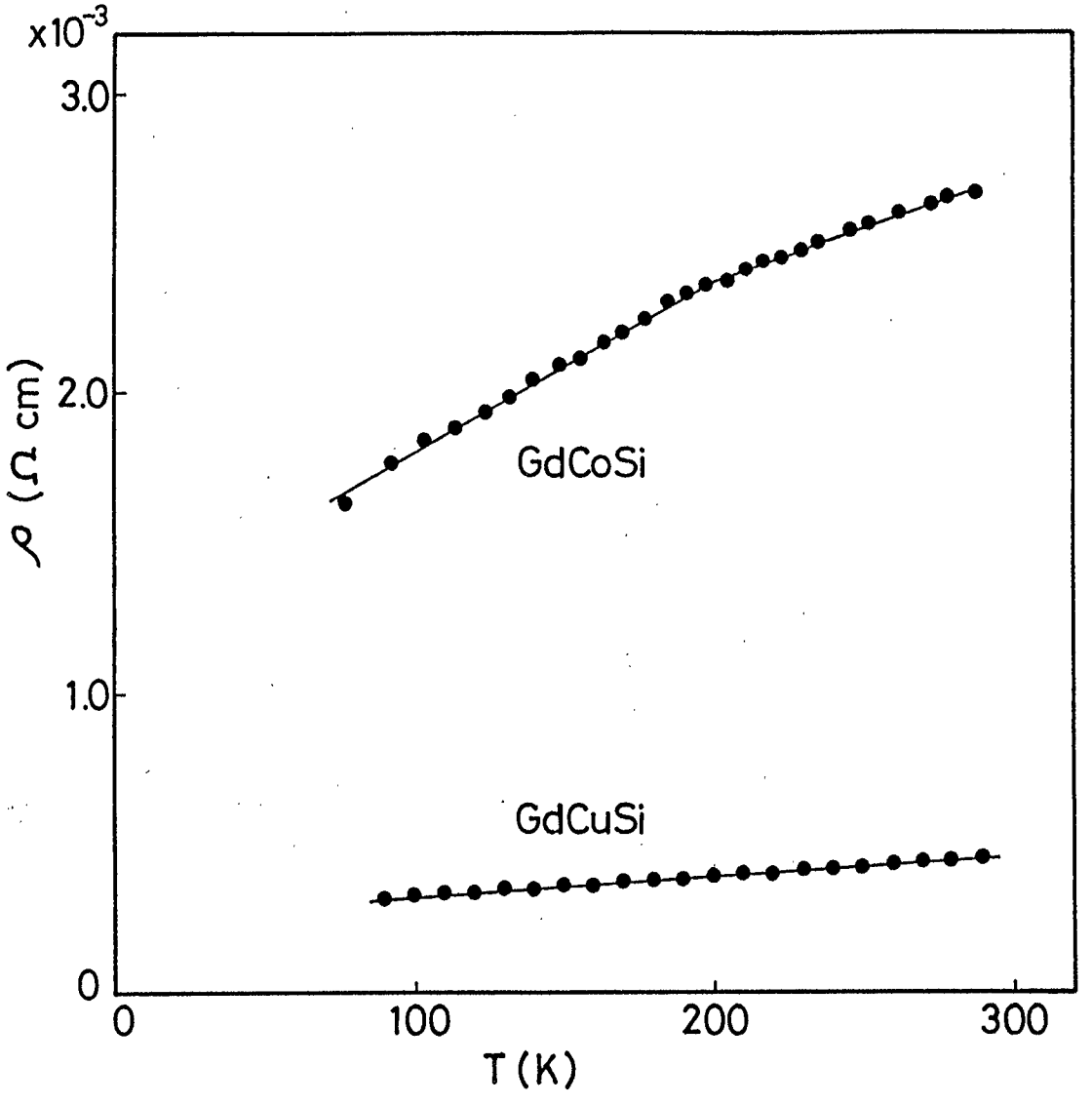

Fig. 68 Temperature dependences of electrical resitivities of GdCoSi(PbFCl-type structure) and GdCuSi (AlB_2-type structure).

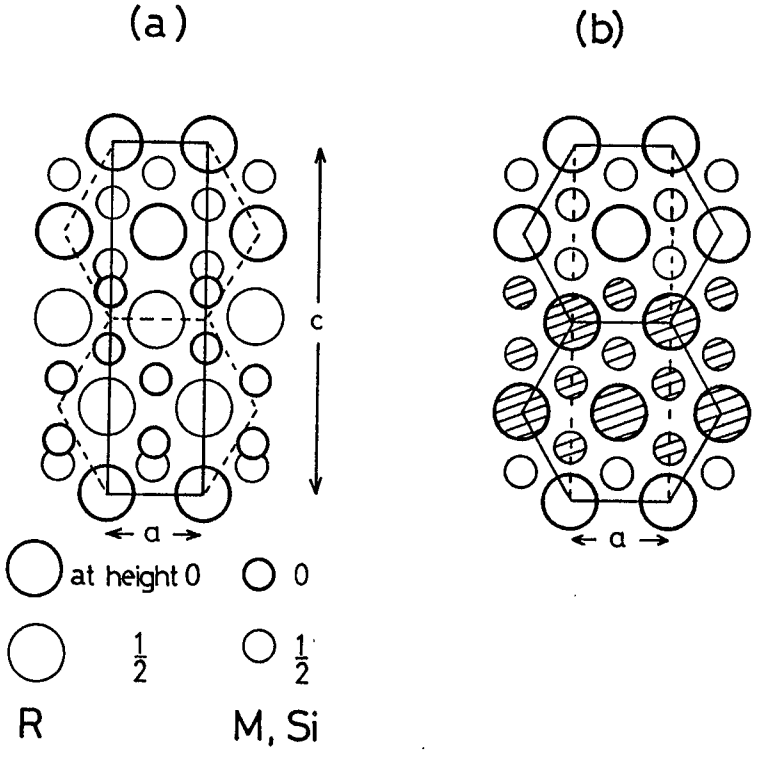

Fig. 69 Crystallographic relation between (a) the $ThSi_2$-type and (b) the AlB_2-type structures.

crystal structure was not for RFeSi (R=La-Ho, Yb). As seen in Fig. 2, this structure was found in case of M=Co and Ni, and it is found that the appearance of the crystal type is closely related to both ratio of the radius of R to those of M and Si, and also to the concentration of conduction electrons.

From the above consideration, the extension of discussion on the crystal structures of GdMSi to all RMSi compounds is possible. The most important feature of the crystal structures of RMSi is the close linkage of transition metal atoms and silicon atoms. Thus, instead of the radius of transition metal atom, the ratio of the radius of R, r_R, to the average atomic radius of M and Si, r_{Ms}, was used. the values of r_R were calculated by $r_R=a/2$ for both PbFCl-type and $ThSi_2$-type structures, and by $r_R=c/2$ for the AlB_2-type structure. The average atomic radius of M and Si was calculated by $r_{MS}=[(a/2)^2+(zc)^2]^{1/2}$ for the PbFCl-type and by $r_{MS}=(1-2z)c/2$ for the $ThSi_2$-type, and by $r_{MS}=a/(2/\bar{3})$ for the AlB_2-type structure, which corresponded to the shortest interatomic distances of M-Si. The values of z=0.175 for Si in the PbFCl-type and of z=0.393 for M or Si in the $ThSi_2$-type structure were used (77,89).

The concentration of conduction electrons was replaced by the number of conduction electron, N. Since Mn atoms in RMnSi had the magnetic moments of about 1.5-2.0 μ_B and Co atoms in GdCoSi had small magnetic moments and Ni atoms in RNiSi had little magnetic moments, Mn, Fe and Co atoms

may offer two electrons in 4s shell to the conduction band and accept three electrons from it. The Ni atoms in RMSi may offer two electrons in 4s shell to the conduction band and accept two electrons. Thus, values of N were calculated to be 6, 7, 8 and 9 for RMSi (M=Mn, Fe and Co), RNiSi, RCuSi and RZnSi, respectively. R and Si atoms were thought to offer 3 and 4 electrons to the conduction band. In the present model, the values of N are not accurate, but the order of them is available. In Fig. 70, the temperature dependence of electrical resistivity of NdMSi was shown. The value of $d\rho/dT$ decreased with increasing the atomic number of M. This result indicated that N increased with increasing the atomic number of M, which was in good agreement with above order of N.

In Table 14, values of r_R, r_{MS}, N, $p=r_{MS}/r_R$, and pN for RMSi are listed. The values of pN for RMSi (M=Mn, Fe, and Co), RNiSi, RCuSi and RZnSi were about 3.47-3.54, 4.68-5.11, 4.97-5.21, 5.18-5.43, respectively. When the compounds of RMSi have the relatively small values of pN, the crystal structure of RMSi would be the tetragonal PbFCl-type. But when RMSi have large values of pN, their crystal structure would be the hexagonal AlB_2-type.

The crystallographic relation between the PbFCl-type and the body-centered tetragonal $ThCr_2Si_2$-type structures is shown in Fig. 71. In both structures, M and Si atoms form the closely packed layers. The coordination of M and Si atoms is the same.

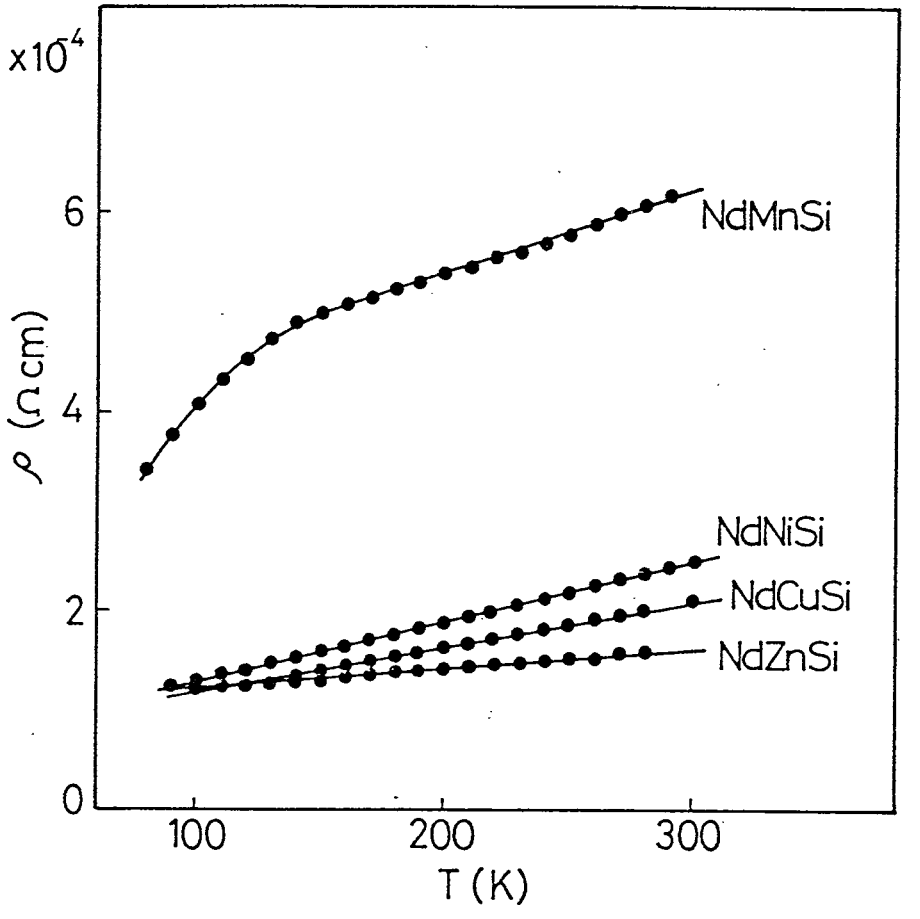

Fig. 70 Temperature dependence of electrical resistivity of NdMSi (M=Mn, Ni, Cu, Zn).

Table 14 Values of r_R, $r_{M,S}$, $p=r_{M,S}/r_R$, N and pN for RMSi

RMSi	r_R*(nm)	$r_{M,S}$*(nm)	$p=r_{M,S}/r_R$	N*	pN
YMnSi	0.1989	0.1175	0.5907	6	3.544
CeMnSi	0.2062	0.1214	0.5887	6	3.532
NdMnSi	0.2046	0.1206	0.5894	6	3.537
SmMnSi	0.2024	0.1194	0.5899	6	3.540
GdMnSi	0.2005	0.1183	0.5900	6	3.540
LaFeSi**	0.2031	0.1194	0.5879	6	3.527
CeFeSi	0.2031	0.1175	0.5785	6	3.471
PrFeSi	0.2036	0.1185	0.5820	6	3.492
NdFeSi	0.2029	0.1180	0.5816	6	3.489
SmFeSi	0.2016	0.1171	0.5809	6	3.485
GdFeSi	0.2001	0.1164	0.5817	6	3.490
TbFeSi	0.1992	0.1158	0.5813	6	3.488
DyFeSi	0.1981	0.1153	0.5820	6	3.492
HoFeSi	0.1969	0.1149	0.5835	6	3.501
YbFeSi	0.1986	0.1157	0.5826	6	3.495
LaCoSi**	0.2035	0.1196	0.5877	6	3.526
CeCoSi	0.2018	0.1180	0.5847	6	3.508
PrCoSi	0.2018	0.1177	0.5833	6	3.500
NdCoSi	0.2013	0.1175	0.5837	6	3.502
SmCoSi	0.2005	0.1165	0.5810	6	3.486
GdCoSi	0.1988	0.1156	0.5815	6	3.489
TbCoSi	0.1979	0.1151	0.5816	6	3.490
NdNiSi	0.2042	0.1490	0.7297	7	5.108
PrNiSi	0.2055	0.1374	0.6686	7	4.680
YCuSi	0.1865	0.1196	0.6413	8	5.130
CeCuSi	0.1969	0.1226	0.6227	8	4.981
NdCuSi	0.1958	0.1216	0.6210	8	4.968
SmCuSi	0.1923	0.1209	0.6287	8	5.030
GdCuSi	0.1891	0.1206	0.6378	8	5.102
TbCuSi	0.1874	0.1201	0.6409	8	5.127
DyCuSi	0.1855	0.1208	0.6512	8	5.210
HoCuSi	0.1840	0.1195	0.6495	8	5.196

Table 14 (continued)

RMSi	r_R^* (nm)	$r_{M,S}^*$ (nm)	$p=r_{M,S}/r_R$	N^*	pN
YZnSi	0.1984	0.1194	0.6018	9	5.416
CeZnSi	0.2119	0.1219	0.5753	9	5.177
NdZnSi	0.2087	0.1203	0.5764	9	5.188
SmZnSi	0.2048	0.1197	0.5845	9	5.260
GdZnSi	0.2000	0.1202	0.6010	9	5.409
TbZnSi	0.1981	0.1195	0.6032	9	5.429
DyZnSi	0.1972	0.1189	0.6029	9	5.426
HoZnSi	0.1971	0.1184	0.6007	9	5.406

*)r_R: radius of rare-earth atom, $r_{M,S}$: average atomic radius of transition metal and silicon atom, N: apparent number of electrons in conduction band of RMSi

**)Lattice constants of RFeSi and RCoSi (R=La, Ce, Pr, Sm) in ref. 77 were used for calculation.

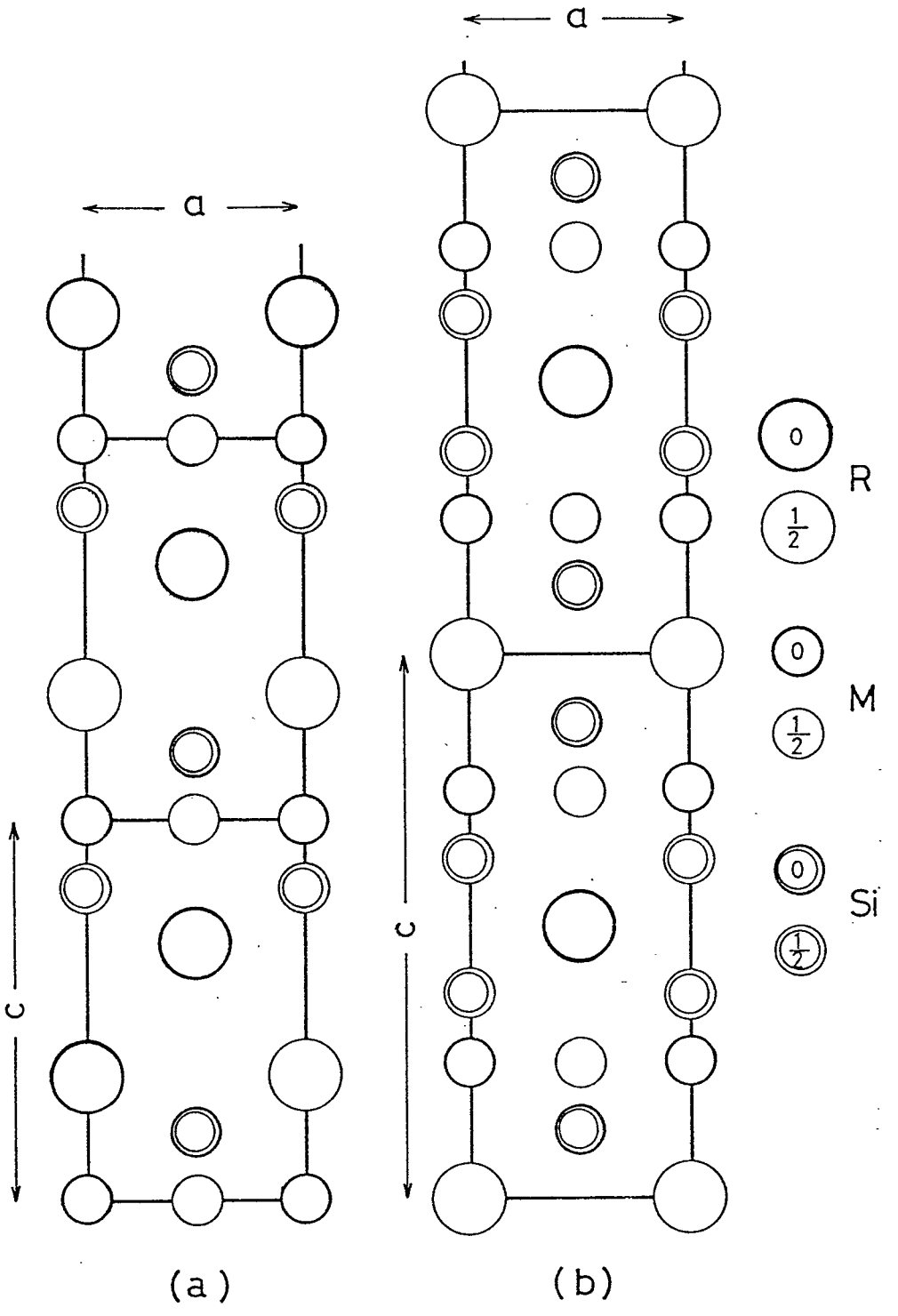

Fig. 71 Crystallographic relation between (a) the PbFCl-type and (b) the $ThCr_2Si_2$-type structures.

4-2 Magnetic and electrical properties of RMnSi, RCoSi and RNiSi

From the magnetic measurements of these compounds, it was found that Mn atoms had the magnetic moment of about 1.5-2.0 μ_B. Since the value of μ_{eff} of GdCoSi was larger than the calculated value for Gd^{3+} ion, the Co atoms in GdCoSi have small magnetic moments. However, values of μ_{eff} for other RCoSi (R=Nd, Tb, and Ho) and RNiSi (R= Nd and Gd) were almost equal to the values for the corresponding R^{3+} ions. The Co and Ni atoms in these compounds probably had little magnetic moment. The change in value of magnetic moment of Co atom by changing elements of rare-earth atoms was also observed in the related RCo_2Si_2 compounds (52).

The decrease in the magnetic moment of transition metal atom in the present ternary system is mainly due to the electron transfer from Si to transition metal atoms. In the PbFCl-type structure, interatomic distances M-Si were rather smaller than the sum of corresponding atomic radii, which may cause the electron transfer. The similar results were reported for the related RM_2X_2 compounds (50, 53,55). Further, it is well known that the magnetic properties of the first-row transition metal borides have been well explained by the electron transfer from boron atom to transition metal atoms in M_2B and MB compounds. The electrical resistivities of RMSi with the PbFCl-type structure were larger than those of RMSi (M=Ni, Cu, and Zn) compounds, which agreed with the consideration

mentioned above. The temperature dependence of electrical resistivity of GdMSi and NdMSi is shown in Figs. 68 and 70, respectively.

Since the R spins in RM_2X_2 compounds magnetically order only in the relatively low temperature range, it is suggested that the magnetic interaction between R spins is weaker. On the other hand, M spins magnetically order in the relatively high temperature range.

From the above considerations, magnetic properties of these compounds can be understood by classifying into the two following cases.

(1) The transition metal atoms in RMSi have the large magnetic moments (M=Mn) or small ones (M=Co in GdCoSi). In this case, in the relatively high temperature range, magnetic properties of RMSi are primarily determined by the magnetic interaction between M spins. And the magnetic interaction changes its sign and magnitude with increasing the interatomic distances of M-M. At low temperature range, R spins may magnetically order and couple with M spins. The magnetic ordering of R spins is thought to be dependent upon the strength of the magnetic interaction between M spins. GdMnSi was ferromagnetic, but RMnSi (R=Nd and Sm), in which interatomic distances of Mn-Mn were larger than those in GdMnSi, were antiferromagnetic. The values of Néel temperatures of NdMnSi and SmMnSi were smaller than the Curie temperature of GdMnSi. In RMnSi (R=Nd and Sm), R spins did not magnetically order above 77K. YMnSi had the shorter

distance of Mn-Mn than that in GdMnSi, and showed the unusual magnetism. The magnetic phase transition from the antiferromagnetic phase to the ferromagnetic phase was observed at about 190K. And the metamagnetic behavior was observed below 150K, indicating that the antiferromagnetic interaction between Mn spins was relatively weak. GdCoSi was ferromagnetic, which may be due to the ferromagnetic interaction between Co spins and the Gd spins slightly align below 50K.

(2) The transition metal atoms in RMSi have little magnetic moment (M=Co except in GdCoSi and Ni). In this case, the magnetic properties of RMSi primarily determined by the magnetic interaction between R spins. The antiferromagnetism of TbCoSi and ferromagnetism of HoCoSi are due to the magnetic interaction between R spins. The paramagnetic Curie temperatures of RCoSi obeyed the $\xi^{2/3}$ law, as seen in Fig. 22.

The paramagnetic Curie temperatures of RMSi compounds with the PbFCl-type structure were positive. From these results and the crystal structure, the ferromagnetic interaction between Mn spins within the layer was expected. This ferromagnetic interaction may be explained by two models. One model is the direct magnetic interaction. The ratio of the M-M interatomic distances to the radius of 3d orbitals $D_{M-M}/2d$ is about 1.66 for M=Mn and 2.33 for M=Co in RMSi with the PbFCl-type structure. The value of d was calculated by Slater's method (90). The value of 1.66 is approximately equal to that of Fe metal,

as shown in Fig. 72. It is found that the magnetic interaction between Mn spins was very large than that between Co spins in these compounds. Another model is the superexchange interaction between Mn spins via the silicon atoms. This model is supported by the experimental results that Mn-Si interatomic distances are smaller than the sum of atomic radii of M and Si. The angle of M-Si-M bond was about 120 degrees. The angle of the M-Si-M bond in RM_2X_2 was about 90 degrees. The ferromagnetic interaction between M spins within the layer for RMSi is expected to be weaker than that for RM_2X_2. The large paramagnetic Curie temperatures were obtained for RMn_2Si_2 and $YMn_2(Si_{1-x}Ge_x)_2$ compounds.

The magnetic interaction between layers changes the sign and depends on the M-M interatomic distance. This magnetic exchange interaction is probably due to the s-d indirect exchange interaction. In this model, the localized magnetic moments polarized the conduction electrons and successively interacted with the other localized magnetic moments. The strength of the interaction oscillatorily decreased with increasing the product of Fermi wave number and distance between M spins.

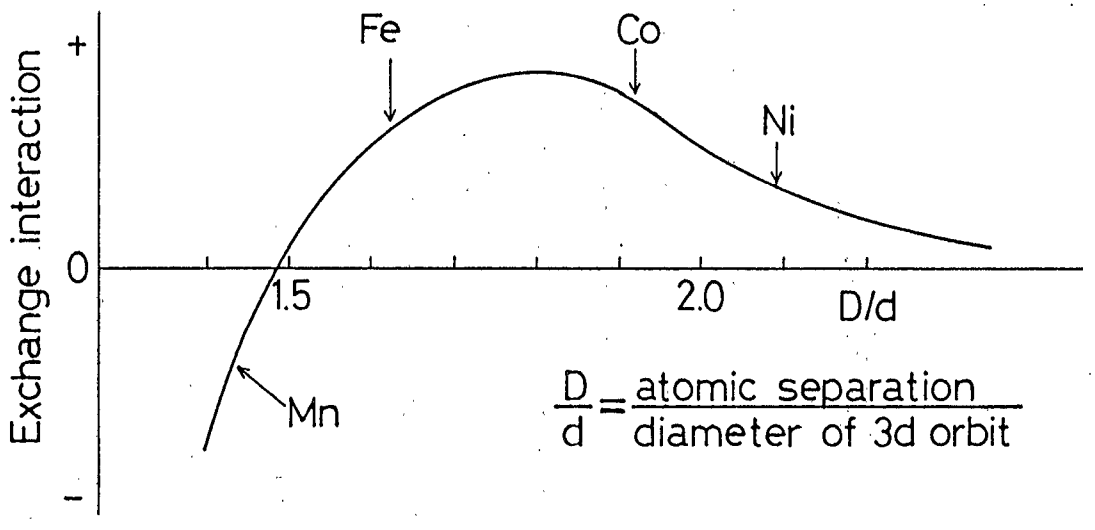

Fig. 72 Slater-Bethe curve showing the magnitude and sign of the exchange integral as a function of D/d.

4-3 Magnetic and electrical properties of RCuSi, RZnSi and $RCu_{1-x}Zn_xSi$ compounds

The electrical resistivities, ρ, which were obtained by extrapolating to 0K, of RCuSi compounds are plotted against the de Genne function, ξ, in Fig. 73. The values of ρ increased with increasing ξ. This result is due to the spin-disorder resistivity. The temperature independent resistivity is caused by defects of crystals and disordered spins. The spin-disorder resistivity in the absence of the crystalline electric field is given as the following equation (91,92)

$$\rho_s = \frac{3\pi NmA^2}{2\hbar e^2 E_F}(g-1)^2 J(J+1), \qquad (3)$$

where N is the number of scattering centers per unit volume, E_F the Fermi energy, A the s-f interaction parameter. The ρ_s increases with increasing $\xi=(g-1)^2 \cdot J(J+1)$. The temperature dependent electrical resistivity is due to the scattering of electrons by phonons. When R spins magnetically order, electrical resistivity due to scattering of electrons by spins is also temperature dependent with the form given as the following equation (93)

$$\rho_s = BT^2 \exp(-\frac{E}{kT}) \qquad (4)$$

The magnetic properties of these compounds are essentially due to the magnetic interaction between R^{3+} spins via the conduction electrons. The effective magnetic moments of these compounds were well in good agreement with the calculated ones for R^{3+}. The

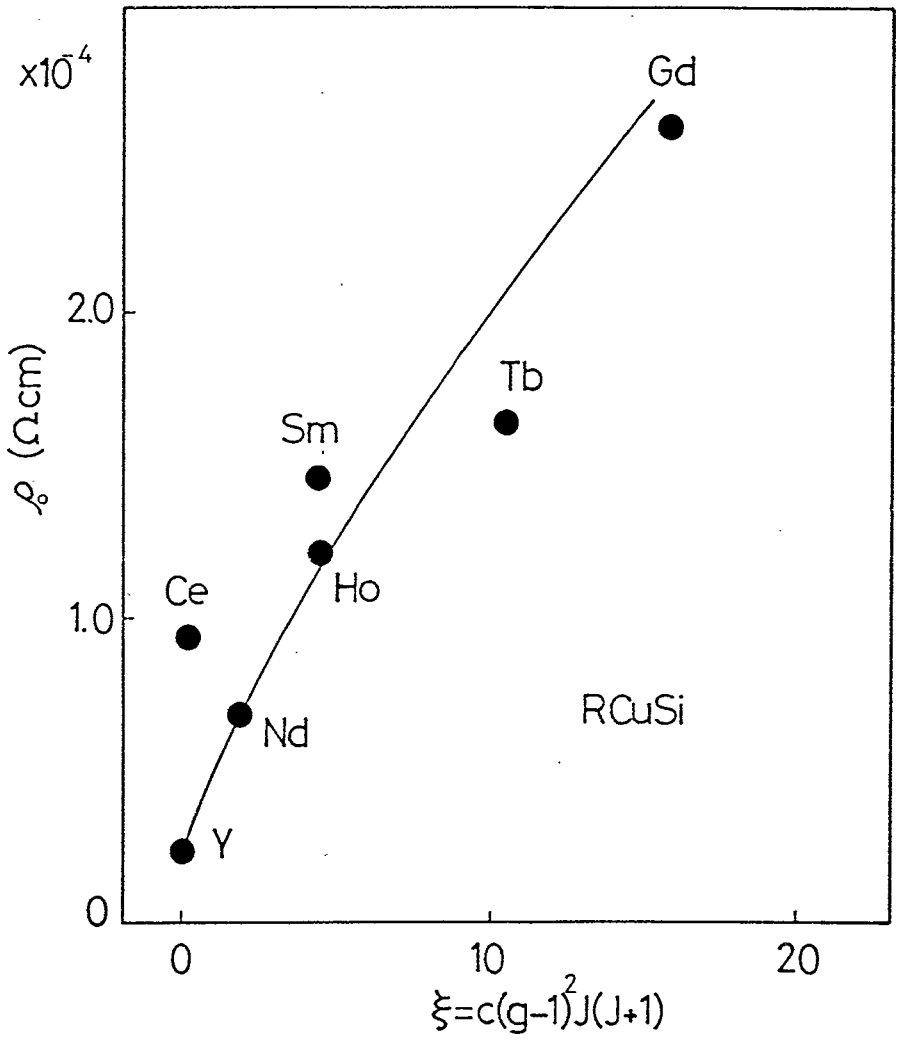

Fig. 73 Electrical resitivity extrapolated to 0 K versus the de Genne function for RCuSi.

paramagnetic Curie temperature and magnetization of $RCu_{1-x}Zn_xSi$ (R=Gd, Dy, Ho) had the maximum at x=0.4. These magnetic behaviors could be well understood by considering the s-f indirect magnetic interaction between R^{3+} spins (94,95). By applying this theory, the paramagnetic Curie temperature is given as the following equation (91,93,95).

$$\theta_a = -\frac{3\pi n^2 A^2}{kE_F} \xi \sum_{j \neq i} F(2K_F R_{ij}), \qquad (5)$$

where n is the concentration of conduction electrons, A the s-f interaction parameter, E_F the Fermi energy, K_F the wave vector at the Fermi surface, R_{ij} the distance between the i-th and j-th rare-earth metal ions, $\xi=(g-1)^2 \cdot J(J+1)$, $F(x)=(x\cos x - \sin x)/x^4$. In $RCu_{1-x}Zn_xSi$ compounds, all R atoms occupy the crystallographically equivalent positions. The summation in Eq. (5) was calculated as a function of K_F for both GdCuSi and GdZnSi within the sphere of a radius of 1×10^{-9} m for a Gd atom, and the result is shown in Fig. 74. There was small difference in amplitude between two curves, but the dependency on K_F was almost the same. This result indicates that the summation was mainly determined by the crystal structure, and its dependency on K_F for $GdCu_{1-x}Zn_xSi$ was almost same over the whole composition range. The same calculations were carried out for $DyCu_{1-x}Zn_xSi$ and $HoCu_{1-x}Zn_xSi$. The results were shown in Figs. 75 and 76. From these results, it is found that the change in θ_a of $RCu_{1-x}Zn_xSi$ by changing x was primarily due to

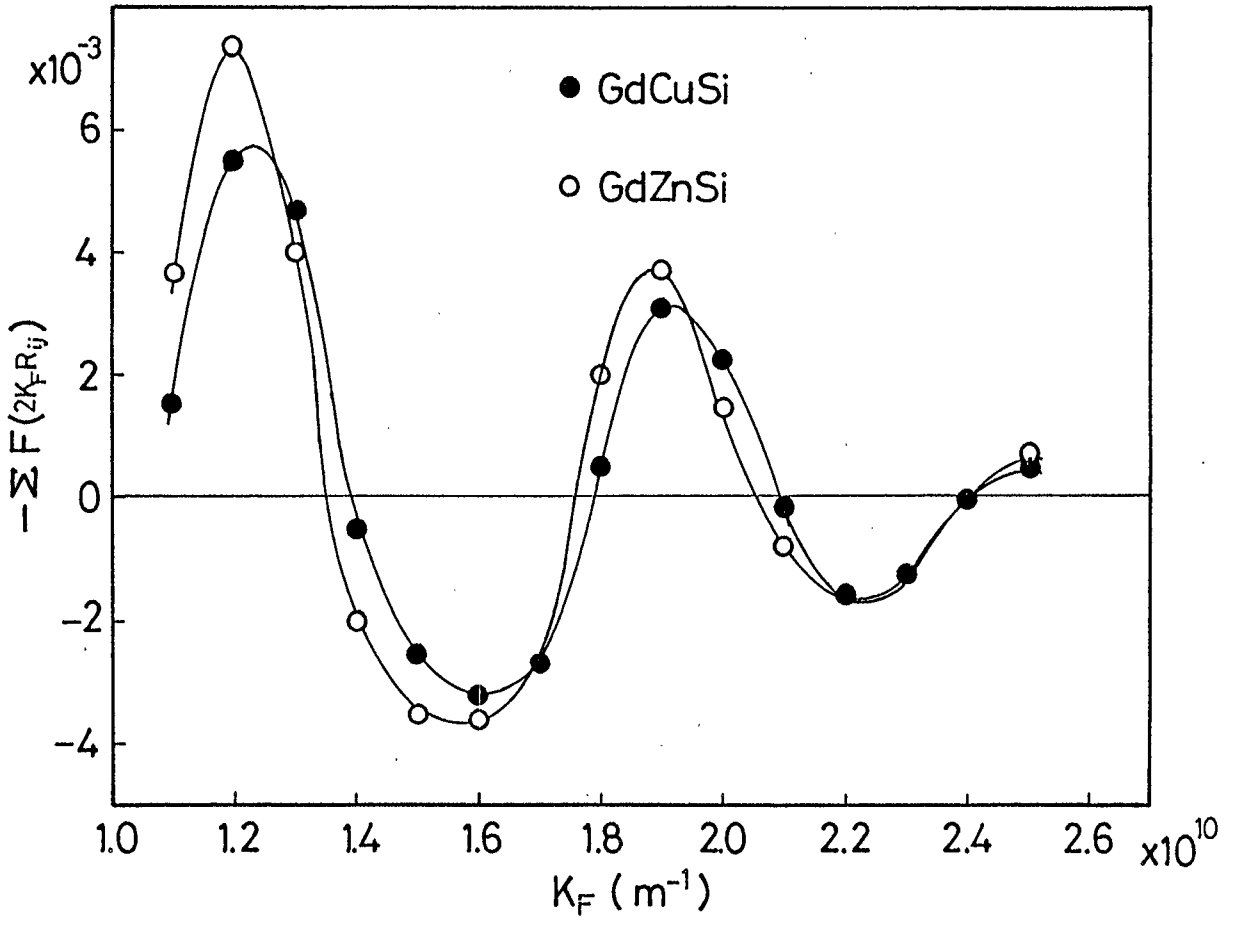

Fig. 74 Dependence of lattice sums for GdCuSi and GdZnSi on Fermi wave vector.

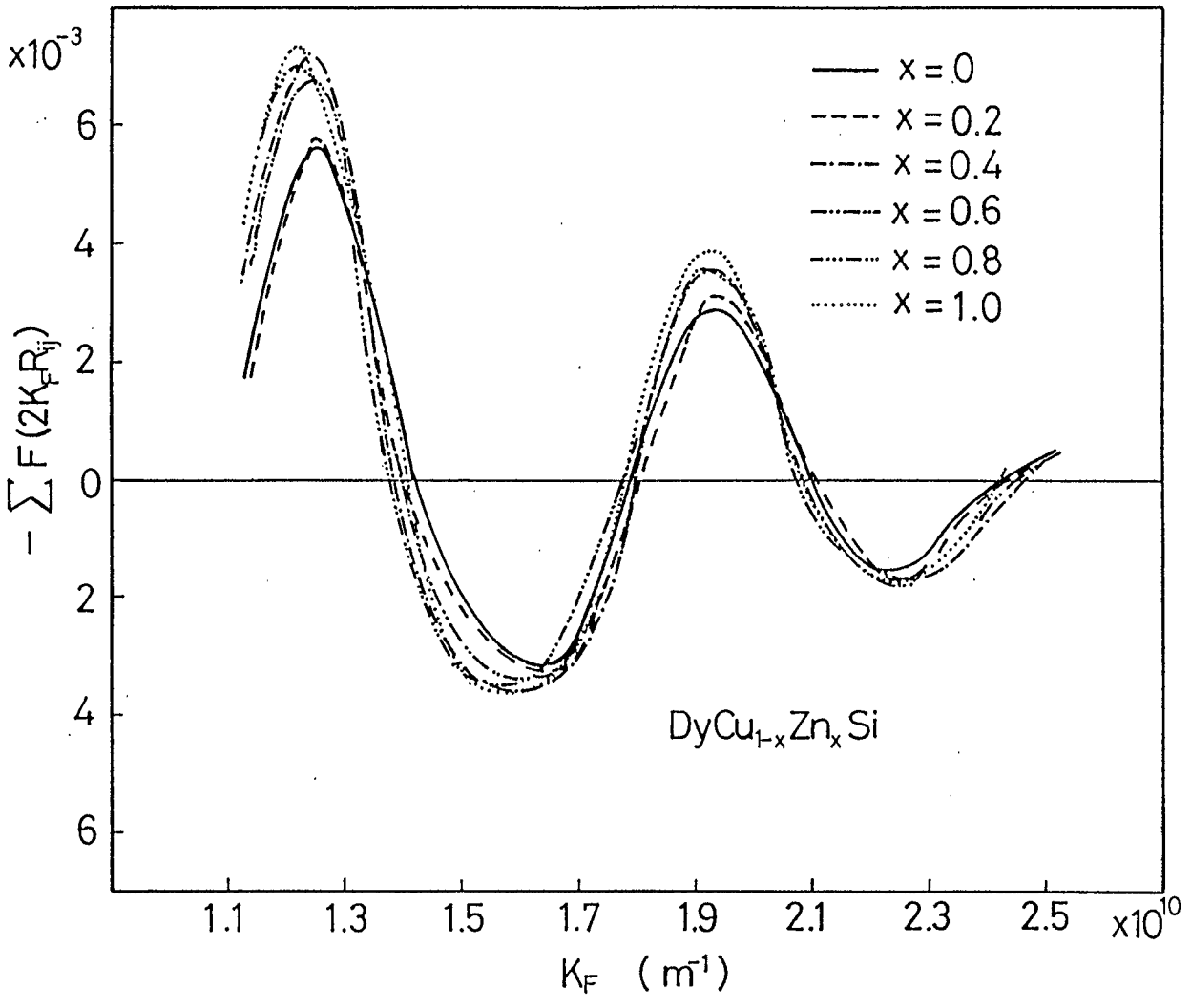

Fig. 75 Dependence of lattice sums of $DyCu_{1-x}Zn_xSi$ on Fermi wave vector.

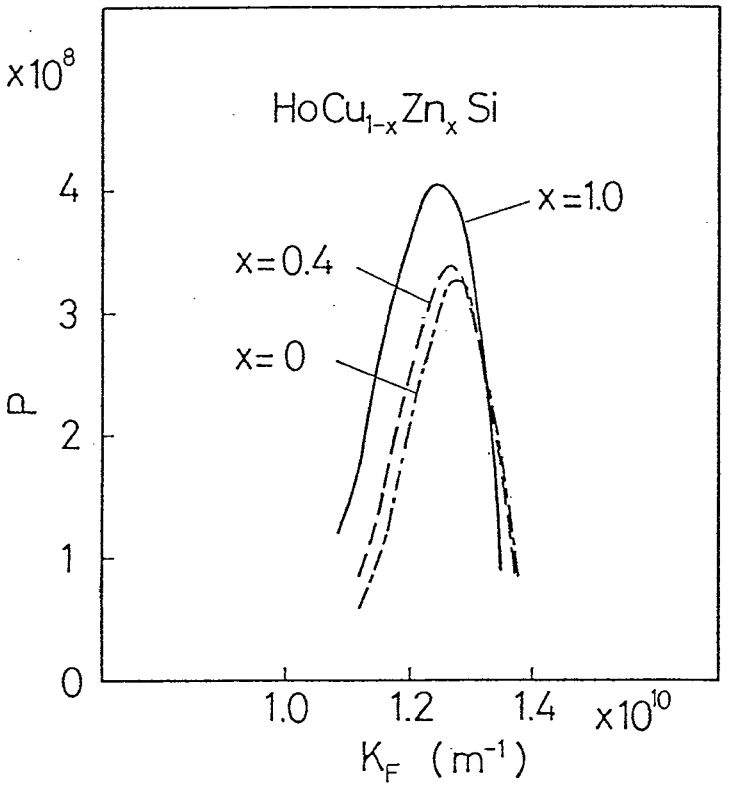

Fig. 76 Dependence of lattice sums of $HoCu_{1-x}Zn_xSi$ on Fermi wave vector.

K_F and secondarily due to R_{ij}.

Since the paramagnetic Curie temperatures of $RCu_{1-x}Zn_xSi$ (R=Gd, Dy, Ho) were positive, the summation in Eq. (5) had to be negative. This condition was satisfied at about $K_F=1.2\times10^{10}$ and 1.9×10^{10} m^{-1}, as seen in Figs. 73-75. By changing K_F at about these values, θ_a had the maximum value, which corresponded to the experimental results. But the result of calculation of the number of conduction electrons per formula unit, N, showed that the region at $K_F=1.9\times10^{10}$ m^{-1} was improbable. To evaluate N, the both relation of $N=nV$ and $K_F^3=3\pi^2n$, where V was the unit cell volume, were used. The values of N were 2.9, 4.2, 11.3 and 17.9 for $K_F=1.15\times10^{10}$, 1.3×10^{10}, 1.8×10^{10} and 2.1×10^{10} m^{-1}, respectively. From these results, it is found that one more electron per formula unit is needed to pass the peak at $K_F=1.2\times10^{10}$ m^{-1}, but seven more electrons are needed to pass the peak at $K_F=1.9\times10^{10}$ m^{-1}. The values of N=11 to 18 and seven more electrons to pass the peak at $K_F=1.9\times10^{10}$ m^{-1} are thought to be too much, and this case is unlikely. Consequently, it is consider that $RCu_{1-x}Zn_xSi$ ($0\leq x\leq1$) compounds have the N values from about 3 to 4 when x changes from 0 to 1.

The change of conduction electrons caused by changing compositional parameter x in $RCu_{1-x}Zn_xSi$ was also supported by the results of electrical resistivity measurements. As seen in Figures 41, 48 and 53, $d\rho/dT$ decreased with curvature when x was increased. The residual electrical resistivity and spin-disorder resistivity in the absence

of the crystalline field are independent of temperature (92,93,96-99). Therefore, if the contribution of the crystalline field to the resistivity could be neglected, $d\rho/dT$ in the paramagnetic region is thought to vary inversely as the square of the concentration of conduction electrons, n, in the conduction band (100). The dashed line in Fig. 42 was calculated on the basis of this assumption. The calculated curve agreed qualitatively with experimental results. From the present results, it is expected that n of $RCu_{1-x}Zn_xSi$ increases with increasing the amount of zinc metal.

The $RCu_{1-x}Zn_xSi$ (R=Gd, Dy and Ho) compounds had the maximum values of θ_a at x=0.4. However, values of θ_a in $HoCu_{0.6}Zn_{0.4}Si$ and $DyCu_{0.6}Zn_{0.4}Si$ were rather smaller than that of $GdCu_{0.6}Zn_{0.4}Si$. This result was thought to be due to the difference in the de Genne function ξ. Introducing the free electron model into the Eq. (5), it was found that θ_a was in proportion to $P=-\xi K_F \sum F(2K_F R_{ij})$. The values of P were calculated as a function of K_F for $RCu_{0.6}Zn_{0.4}Si$ (R=Gd, Dy, Ho and Nd). The results are shown in Fig. 77. The peak heights decreased with decreasing ξ. The values of for Gd, Dy, Ho and Nd are 15.75, 7.08, 4.50 and 1.84, respectively (93). Consequently, it is considered that the magnetic interaction between rare-earth spins in the $RCu_{1-x}Zn_xSi$ (R=Gd, Dy, Ho and Nd) systems would be strong as in the following order, Gd>Dy>Ho>Nd.

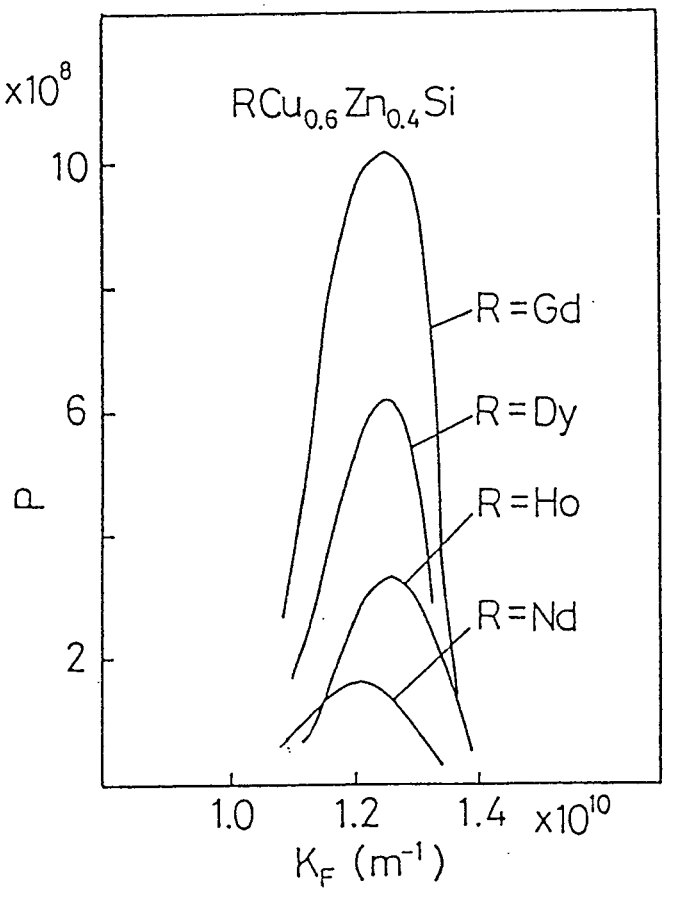

Fig. 77 Dependence of lattice sums of $RCu_{0.6}Zn_{0.4}Si$ on Fermi wave vector.

4-4 Magnetic properties of RMn_2Si_2 and $YMn_2(Si_{1-x}Ge_x)_2$ compounds

The crystal structure of RM_2X_2 compounds is well related to that of RMSi with the PbFCl-type structure. The PbFCl-type structure consists of atomic layers perpendicular to c-axis stacked with the sequency of M-Si-R-R-Si-M. On the other hand, atomic layer stacked with the sequency of R-X-M-X-R-X-M-X-R in RM_2X_2 with the $ThCr_2Si_2$-type structure. In the both crystal structures, M-X interatomic distances are much smaller. From these similarities in crystal structure, it is considered that magnetic properties of these compounds are also understood on the basis of the following two important factors.

One is the electron transfer from X to M. As seen in Tables 10 and 12, M-X interatomic distances are much smaller than those for the sum of corresponding atomic radii. This fact would result in the electron transfer from X to M. Magnetometric and neutron diffraction studies showed that M atoms in RM_2X_2 had little localized magnetic moments except M=Mn (52-69). Another factor is the M-M interatomic distance. As seen in Figs. 59 and 62, RMn_2Si_2 and $YMn_2(Si_{1-x}Ge_x)_2$ compounds were anti-ferromagnetic and T_N decreased with increasing Mn-Mn interatomic distance.

As seen in Tables 11 and 13, θ_a of these compounds were positive. Considering the results of the neutron diffraction for $ThMn_2Si_2$ (73), the present result indicated that Mn spins within the layer ordered ferromagnetically

and Mn spins between the layers ordered antiferromagnetically in these compounds.

As seen in Fig. 64, it was found that θ_a of $YMn_2(Si_{1-x}Ge_x)_2$ were almost constant, but those for RMn_2Si_2 decreased with increasing the magnetic moment of R. The disordered R spins weaken the ferromagnetic interaction between Mn spins within the layer.

To interpret the ferromagnetic interaction, two models are probable. One is the direct ferromagnetic interaction between Mn spins within the layers. The ratios of $D_{Mn-Mn}(a)$ to the diameter of 3d orbit for Mn atoms in $YMn_2(Si_{1-x}Ge_x)_2$ were about 1.65. This result and Slater-Bethe curve (Fig. 72) support the possibility of this model. Another possible model is the superexchange interaction via silicon or germanium atoms. The shorter Mn-X interatomic distances may be enable to transfer the electron from X to Mn. The angle of the Mn-X-Mn bond was calculated to be about 90 degrees, which resulted in the ferromagnetic interaction within the layers.

For the magnetic coupling between layers in the $La_{1-x}Y_xMn_2Si_2$ compounds, Sampathkumaran et al. (63) suggested the existence of the superexchange interaction. In $La_{1-x}Y_xMn_2Si_2$, the transition from antiferromagnetism to ferromagnetism was occured at the Mn-Mn interatomic distances of 0.288 nm in the a direction and o.529 nm in the c direction. However, this critical Mn-Mn distances did not hold for $YMn_2(Si_{1-x}Ge_x)_2$ system, as seen in Fig. 63. $YMn_2(Si_{1-x}Ge_x)_2$ (x=0.4, 0.6 and 0.8),

which have larger $D_{Mn-Mn}(c)$ than 0.529 nm, were antiferromagnetic. This result indicated that the magnetism of these compounds depended on both Mn-Mn interatomic distances and bonding character of Mn-X, which is affected by the electron transfer.

The other possible model for the magnetic coupling between Mn layers is the indirect s-d exchange interaction via the conduction electrons. This interaction decreased in relation to D_{Mn-Mn}^{-3} with changing the sign of the interaction. The curvature in Fig. 63 may correspond to this fact.

4-5 Thermoelectric power of RZnSi compounds

In the metallic conducters, the ratio of thermally excited electrons to all electrons in metal is expressed to be about T/T_F, where T_F is the Fermi temperature. Since the thermal energy per one excited electron is about $kT(T/T_F)$, Peltier energy π is given by the following equation

$$\pi \sim \frac{kT}{e}\frac{T}{T_F} \tag{6}$$

The thermoelectric power S is related to π as $\pi = TS$. Thus, S is expressed as the following equation (101).

$$S = \pi / T \sim \frac{k}{e}\frac{T}{T_F}. \tag{7}$$

RZnSi were metallic. Consequently, S is in relation to T, as seen in Fig. 38. Then by applying the free electron model, T_F can be written as

$$T_F = \frac{h^2(3\pi^2 n)^{2/3}}{2mk} \tag{8}$$

where n is the concentration of conduction electrons, m mass of electron. Introducing Eq. (8) into Eq. (7), S can be rewritten as

$$S = \frac{2k^2 mT(3\pi^2 n)^{-2/3}}{eh^2} \tag{9}$$

It is found that dS/dT is in relation to $n^{-2/3}$. In Fig. 78 dS/dT for RZnSi compounds were plotted against R. The value of dS/dT decreased with increasing atomic number of rare-earth elements. This fact may indicate that n for RZnSi increase with increasing atomic number of rare-earths. Since it is expected that R, Zn and Si atoms offer the constant numbers of electrons to conduction band of each RZnSi compound, above result may be due to the lanthanide contraction.

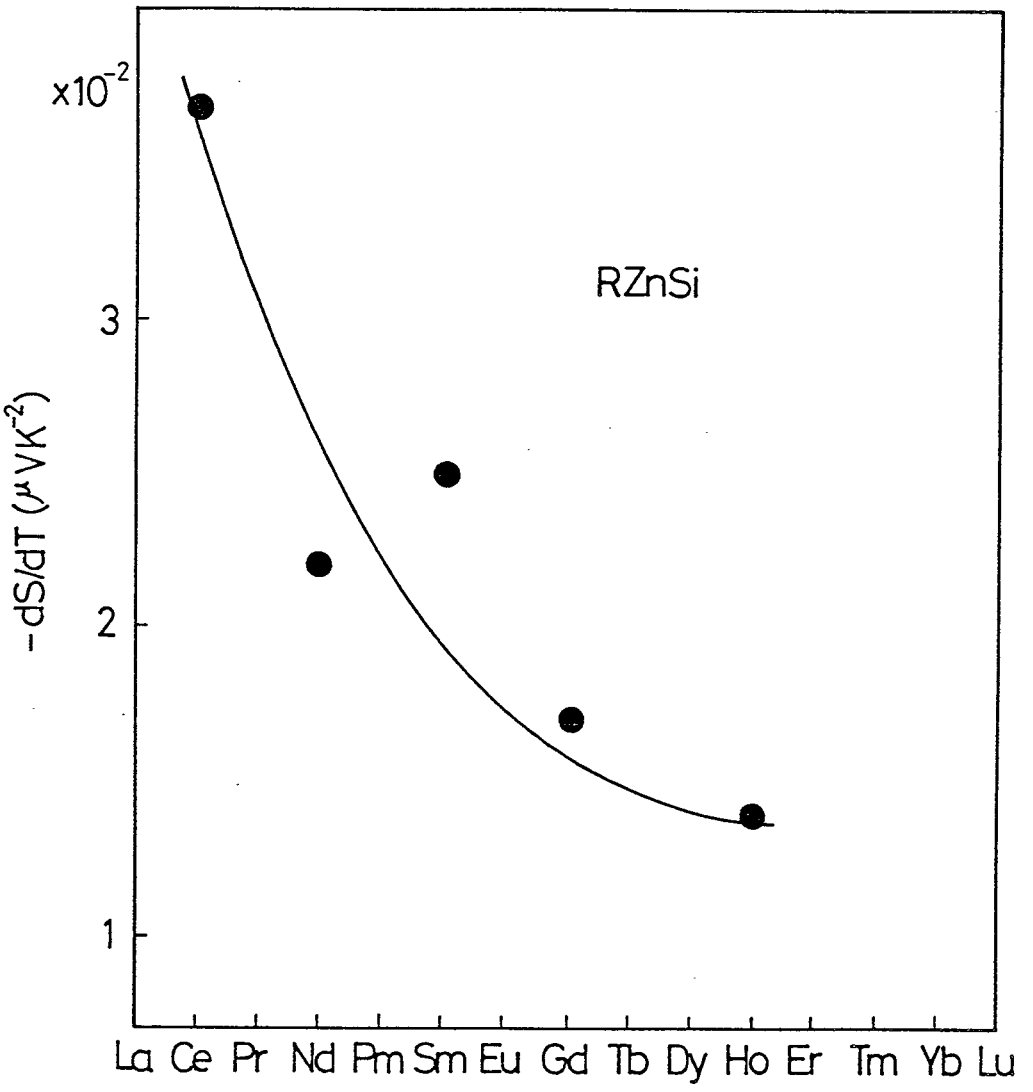

Fig. 78 Temperature gradient of thermoelectric power for RZnSi.

4-6 Solid state chemistry of rare-earth first-row transition metal silicides

The most important crystallographic feature of the rare-earth-transition metal silicides of RMSi and RM_2X_2 was the short M-Si interatomic distance. This close linkage of M and Si resulted in variation of lattice parameter of RMnSi, RCoSi, RCuSi, RZnSi, $RCu_{1-x}Zn_xSi$ and $YMn_2(Si_{1-x}Ge_x)_2$, where the lattice parameter c decreased more rapidly than the lattice parameter a, when an atomic number of R or compositional parameter x increased.

The short M-Si interatomic distance played the important role to the magnetic and electrical properties. The short M-Si distance may cause the electron transfer from Si to M, which decrease both numbers of unpaired electrons of transition metal and conduction electrons. Transition metal elements except Mn had little magnetic moment. Both electrical resistivity and its temperature coefficient of GdMSi (M=Co, Cu) and NdMSi (M=Mn, Ni, Cu, Zn) decreased with increasing the atomic number of M, as seen in Figs. 68 and 70.

The most remarkable feature of rare-earth atom is that 4f electrons are localized inside the $(5s)^2(5p)^6$ closed shell, which is different from 3d electrons. In all RMSi and RM_2Si_2 compounds investigated, the rare-earth metals had the magnetic moments which were nearly identical to those of corresponding trivalent state. This fact implies that 5d and 6s electrons are supplied to the conduction band and a highly localized magnetic moment

due to unpaired 4f electrons is left at each lattice site of rare-earth atom.

Since 4f electrons localized inside the closed shell, R spins can not interact directly with the other R spins. They interact via conduction electrons. This fact successfully explained the experimental results for $RCu_{1-x}Zn_xSi$ compounds. In $GdCu_{1-x}Zn_xSi$, both GdCuSi and GdZnSi were paramagnetic above 77K, but the compounds with x=0.1-0.6 were ferromagnetic. The ferromagnetic moment and Curie temperature showed maxima of 6.4 μ_B and 195K, respectively. This is the first compound which had a large ferromagnetic moment in RMSi compounds with the AlB_2-type structure.

The 4f electrons mainly contribute to the magnetic properties of the rare-earth transition metal silicides, and contribute secondary to the conduction phenomena. R spins acted as scattering centers of conduction electrons. The electrical resistivity extrapolated to 0K of RCuSi increased with increasing the de Genne function, which was due to the scattering of conduction electrons by disordered R spins.

Thus, rare-earth first-row transition metal silicides had the characteristic crystal structure, and revealed the interesting magnetic and electrical properties due to 4f electrons.

CHAPTER 6

SUMMARY

Ternary rare-earth first-row transition metal silicides were prepared and their crystal structures and magnetic and electrical properties were examined. The results are summarized as followings;

1) The crystal structure of GdTiSi was the hexagonal AlB_2-type. GdTiSi was paramagnetic above 77K. The effective magnetic moment, μ_{eff}, and paramagnetic Curie temperature, θ_a, were 7.1 μ_B and 10K, respectively. From the value of μ_{eff}, it was found that magnetic properties of GdTiSi was due to only Gd^{3+} spins.

2) The crystal structure of RMnSi (R=Y, Ce, Nd, Sm, Gd) was the tetragonal PbFCl-type. YMnSi was metamagnetic. The magnetic phase transition from antiferromagnetism to ferromagnetism may occur when temperature is increased. The Curie temperature, T_c, of YMnSi was 282K. The ferromagnetic moment, n_f, at 190K was 1.3 μ_B, indicating that Mn spins had the almost parallel alignment. The values of μ_{eff} and θ_a were 2.3 μ_B and 280K, respectively. NdMnSi and SmMnSi were antiferromagnetic with Néel temperatures, T_N, of 120K and 172K, respectively. The values of μ_{eff} and θ_a of NdMnSi were 5.3 μ_B and 150K, respectively. NdMnSi and SmMnSi were metallic and the temperature dependence of electrical resistivity, ρ, changed the slope at T_N. GdMnSi was ferromagnetic with T_c=320K. The value of

n_f was 5.2 μ_B at 77K and 8 kOe.

The values of T_C and T_N of RMnSi decreased with increasing Mn-Mn interatomic distances.

3) The crystal structure of RCoSi (R=Nd, Gd and Tb) was the tetragonal PbFCl-type. NdCoSi was paramagnetic above 77K. The values of μ_{eff} and θ_a were 3.2 μ_B and 32K, respectively. GdCoSi was ferromagnetic with T_C=250K. The values of μ_{eff} and θ_a were 8.7 μ_B and 131K, respectively. GdCoSi was metallic. The ρ-T curve changed the slope at T_C. TbCoSi was antiferromagnetic with T_N=128K. The values of μ_{eff} and θ_a were 9.1 μ_B and 108K, respectively. Magnetic measurements showed that Co atoms in RCoSi, except GdCoSi, probably had little magnetic moment. The Co atoms in GdCoSi had small magnetic moments. The values of θ_a obeyed the formula of $\theta_a=20.9\xi^{2/3}$.

4) NdNiSi was paramagnetic above 77K. The values of μ_{eff} and θ_a were 3.6 μ_B and -16K, respectively. The value of μ_{eff} was in good agreement with the calculated value for Nd^{3+} ions. The 3d shells of Ni atoms probably fully filled with electrons transfered from Si atoms. NdNiSi was metallic. The value of ρ was about 2×10^{-4} Ωcm. The value of $d\rho/d$ T was 6.1×10^{-7} Ωcm/K.

5) The crystal structure of RCuSi (R=Y, Ce, Nd, Sm, Gd, Tb, Dy and Ho) compounds was the hexagonal AlB_2-type. RCuSi were metallic. The ρ increased with increasing temperature. The values of ρ, which were extrapolated to 0K, increased with increasing the de Genne function. This fact is due to the spin-disorder resistivity.

The values of μ_{eff} of these compounds were in good agreement with those calculated for R^{3+} ions. The magnitude of χ of YCuSi and SmCuSi was 10^2 times smaller than those of the other compounds, and no temperature dependence was found. The values of θ_a of RCuSi (R=Ce, Nd, Gd, Tb, Dy and Ho) were negative for the light rare-earth elemnts but positive for the heavy rare-earths.

6) The crystal structure of RZnSi (R=Y, Ce, Nd, Sm, Gd, Tb, Dy and Ho) was the hexagonal AlB_2-type. RZnSi were metallic. The values of $d\rho/dT$ for RZnSi were smaller than those for RCuSi. The values of μ_{eff} of these compounds were in good agreement with those for R^{3+} ions. The values of θ_a of these compounds were positive, and larger than those for corresponding RCuSi. The thermoelectric power of RZnSi increased with increasing temperature. The order of it was 10 μV/K.

7) The crystal structure of $GdCu_{1-x}Zn_xSi$ ($0 \leq x \leq 1$) was the hexagonal AlB_2-type. Lattice constants obeyed the Vegard's law. $GdCu_{1-x}Zn_xSi$ were ferromagnetic in the composition range from x=0.1 to 0.6. The n_f, T_c and θ_a had a peak at x=0.4. The values of T_c and n_f for $GdCu_{0.6}Zn_{0.4}Si$ were 195K and 6.4 μ_B, respectively. The value of n_f=6.4 μ_B is due to the almost parallel alignment of Gd^{3+} spins. The temperature dependence of $GdCu_{1-x}Zn_xSi$ changed the slope at T_c. The values of $d\rho/dT$ of $GdCu_{1-x}Zn_xSi$ decreased with increasing x.

The crystal structure of $DyCu_{1-x}Zn_xSi$, $HoCu_{1-x}Zn_xSi$ and $NdCu_{0.6}Zn_{0.4}Si$ was the hexagonal AlB_2-type.

Both $DyCu_{1-x}Zn_xSi$ and $HoCu_{1-x}Zn_xSi$ were metallic. The values of $d\rho/dT$ decreased with increasing compositional parameter x.

The magnetic properties of $RCu_{1-x}Zn_xSi$ compounds were examined by using RKKY theory. As a result, the peak of θ_a was found to be due to the magnetic interaction between R^{3+} spins, which changed the magnitude and sign by changing the concentration of conduction electrons in conduction band. The Fermi wave number was calculated to be about 1.2×10^{10} m^{-1} at x=0.4. The number of electrons of conduction band per formula unit may change from about 3 to 4 when x changes from 0 tol. The magnitude of magnetic interaction between R^{3+} spins of $RCu_{0.6}Zn_{0.4}Si$ is dependent upon the de Genne function, ξ.

8) The crystal structure of RMn_2Si_2 (R=Y, Nd and Gd) was the tetragonal $ThCr_2Si_2$-type. RMn_2Si_2 (R=Y, Nd and Gd) were antiferromagnetic with T_N=514K, 386K and 477K, respectively. The Néel temperatures of these compounds decreased with increasing Mn-Mn interatomic distances. The values of θ_a of YMn_2Si_2, $NdMn_2Si_2$ and $GdMn_2Si_2$ were 395K, 303K and 162K, respectively. These high paramagnetic Curie temperatures indicated that Mn spins within the layer order ferromagnetically.

9) The crystal structure of $YMn_2(Si_{1-x}Ge_x)_2$ was the $ThCr_2Si_2$-type. They were antiferromagnetic with T_N=475K, 456K, 436K and 426K for x=0.2, 0.4, 0.6 and 0.8, respectively. The antiferromagnetism of these compounds is only due to magnetic interaction between Mn spins. The values of θ_a

were about 400K and independent of composition. In comparison with these results and those for RMn_2Si_2, it was found that the disordered R spins weakened the both antiferromagnetism between the layers and ferromagnetism within the layer. The values of T_N and θ_a decreased more rapidly when R had magnetic moments.

10) The crystallographic relation among the AlB_2-type, the PbFCl-type and the $ThSi_2$-type structures was found. The crystal structure of RMSi compounds was dependent on the product of the number of conduction electrons, N, and the ratio of radius of rare-earth, r_R, to that of average radius of transition metal and silicon atom, $r_{M,S}$. The magnitude of the product, $(r_{MS}/r_R)N$, increased in the following order, PbFCl-type, $ThSi_2$-type, AlB_2-type.

ACKNOWLEDGEMENTS

The author is greatly indebted to Professor M. Koizumi at Osaka University for his continuing help throughout this work and to Professors F. Kanamaru, T. Shono and J. Shiokawa at Osaka University for their valuable discussions.

The author would like to acknowledge Professor M. Shimada at Tohoku University for the continuing guidance and helpful discussions and encouragement throughout this work.

The author wishes to thank all members of the laboratories under the direction of Professors M. Koizumi and S. Kume at Osaka University.

The author also express his thanks to Drs. Y. Watanabe, K. Nara, H. Toyuki and T. Hoshikawa at Osaka Municipal Technical Research Institute for encouraging and giving the aid to complete this work.

REFERENCES

1 B. Aronsson, T. Lundström and S. Rundqvist, "BORIDES, SILICIDES AND PHOSPHIDES", John Wiley & Sons, Inc., New York, 1965.

2 A. S. Berezhnoi, "SILICON AND ITS BINARY SYSTEM" Consultants Burea, New York, 1958.

3 J. G. White and E. F. Hockings, Inorg. Chem., 10, 1934 (1971).

4 I. Engström and F. Zackrisson, Acta. Chem. Scand., 24, 2109 (1970).

5 H. Kido, M. Shimada and M. Koizumi, unpublished.

6 D. Shinoda and S. Asanabe, J. Phys. Soc. Japan, 21, 555 (1966).

7 D. Shinoda and S. Asanabe, Nippon Butsuri Gakkaishi, 21, 778 (1966).

8 Y. Ishikawa, T. Komatsubara and D. Bloch, physica 86-88B, 401 (1977).

9 D. Bloch, J. Voiron, V. Jaccarino and J. H. Werinick, Phys. Letters 51A, 259 (1975).

10 C. N. Guy, Solid State Commun. 25, 169 (1978).

11 H. Yasuoka, R. S. Hayano, N. Nishida, K. Nagamine, T. Yamazaki and Y. Ishikawa, Solid State Commun. 26, 745 (1978).

12 Y. Ishikawa, K. Tajima, D. Bloch and M. Roth, Solid State Commun. 19, 525 (1976).

13 K. Motoya, H. Yasuoka, Y. Nakamura and J. H. Wernick, Solid State Commun. 19, 529 (1976).

14 S. Kasuya, K. Yamamoto, T. Komatsubara and Y. Ishikawa, Solid State Commun. 20, 925 (1976).

15 K. Motoya, H. Yasuoka, Y. Nakamura, V. Jaccarino and J. H. Wernick, J. Phys. Soc. Japan 44, 833 (1978).

16 H. Yasuoka, V. Jaccarino, R. C. Sherwood and J. H. Wernick, J. Phys. Soc. Japan 44, 842 (1978).

17 M. Date, K. Okuda and K. Kadowaki, J. Phys. Soc. Japan 42, 1555 (1977).

18 Y. Ishikawa, G. Shirane, J. A. Tarrin, M. Kohgi, Phys. Rev. 16, 4956 (1977).

19 V. Jaccarino, G. K. Wertheim, J. H. Wernick, L. R. Walker and S. Arajs, Phys. Rev. 160, 476 (1967).

20 H. Watanabe, H. Yamamoto and K. Ito, J. Phys. Soc. Japan 18, 995 (1963).

21 M. Kohgi and Y. Ishikawa, Solid State Commun. 37,833 (1981).

22 R. Benoit, J. Chem. Phys. 52, 119 (1955).

23 G. K. Wertheim, J. H. Wernick and D. N. E. Buchanan, J. Appl. Phys. 37, 3333 (1966).

24 H. J. Williams, J. H. Wernick, R. C. Sherwood and G. K. Wertheim, J. Appl. Phys. 37, 1256 (1966).

25 D. Shinoda, phys. stat. sol. (a) 11, 129 (1972).

26 S. Kawarazaki, H. Yasuoka and Y. Ishikawa, Solid State Commun. 10, 919 (1972).

27 J. H. Wernick, G. K. Wertheim and R. C. Sherwood, Mat. Res. Bull. 7, 1431 (1972).

28 C. B. Shoemaker and D. P. Shoemaker, Acta Cryst. 18, 900 (1965).

29 V. Johnson and W. Jeitschko, J. Solid State Chem. 4, 123 (1972).

30 V. Johnson and C. G. Frederick, phys. stat. sol. (a) 20, 331 (1973).

31 H. Binczycka, A. Szytula, J. Todorovic, T. Zaleski and A. Zieba, phys. stat. sol. (a) 35, K69 (1976).

32 S. Niziol, H. Binczycka, A. Szytula, J. Todorovic, R. Fruchart, J. P. Senateur and D. Fruchart, phys. stat. sol. (a) 45, 591 (1978).

33 V. Johnson, Inorg. Chem. 14, 1117 (1975).

34 R. M. Ware and D. J. McNeil, Proc. IEE 111, 178 (1964).

35 S. Asanabe and D. Shinoda, Bussei No. 6, 309 (1964).

36 D. Hohnke and E. Parthe, Acta Cryst. 20, 572 (1966).

37 E. Parthe, Acta Cryst. 12, 559 (1959).

38 V. N. Nguyen, J. Laforest and J. Sivardiere, Solid State Commun. 8, 23 (1970).

39 V. N. Nguyen, F. Tcheou and J. Rossat-Mignod, Solid State Commun. 23, 821 (1977).

40 J. A. Perri, E. Banks and B. Post, J. Phys. Chem. 63, 2073 (1959).

41 J. A. Perri, E. Banks and B. Post, J. Phys. Chem. 63, 616 (1959).

42 I. P. Mayer, E. Banks and B. Post, J. Phys. Chem. 66, 693 (1962).

43 I. Mayer, E. Yanir and I. Shidlovsky, Inorg. Chem. 6, S42 (1967).

44 K. Sekizawa and K. Yasukochi, J. Phys. Soc. Japan 21, 274 (1966).

45 G. S. Smith, A. G. Tharp and Q. Johnson, Act Cryst. 22, 940 (1967).

46 W. Rieger and E. Parthe, Monatsh. Chem. 100, 444 (1969).

47 D. Rossi, R. Marazza and R. Ferro, J. Less-Common Met. 58, 203 (1978).

48 D. Rossi, R. Marazza, D. Mazzone and R. Ferro, J. Less-Common Met. 59, 79 (1978).

49 I. Mayer, J. Cohen and I. Ferner, J. Less-Common Met. 30, 181 (1973).

50 I. Felner and I. Mayer, A. Grill and M. Schieber, Solid State Commun. 16, 1005 (1975).

51 S. G. Sanker, S. K. Malik, V. U. S. Rao and R. Obermyer, A. I. P. Conf. Proc. 34, 236 (1976).

52 J. K. Yakinthos and CH. Routsi, J. Less-Common Met. 72, 205 (1980).

53 W. M. McCall, K. S. V. L. Narasimhan and R. A. Butera, J. Appl. Phys. 44, 4724 (1973).

54 H. Oesterreicher, phys. stat. sol. (a) 39, K75 (1977).

55 P. A. Kotsanidis and J. K. Yakinthos, Solid State Commun. 40, 1041 (1981).

56 Z. Ban, L. Omejec, A. Szytula and Z. Tomkowicz, phys. stat. sol. (a)27, 338 (1975).

57 F. Steglich, J. Aarts, C. D. Bredl, W. Licke, D. Meschede, W. Franz and H. Schäfer, Phys. Rev. Lett. 43, 1892 (1979).

58 M. Ishikawa, H. F. Braun and I. L. Jorda, Phys. Rev. B27, 3092 (1983).

59 H. Schneider, Z. Kletowski, F. Osfer and D. Wohlleben, Solid State Commun. 48, 1093 (1983).

60 I. Felner, J. Phys. Chem. Solids 36, 1063 (1975).

61 K. S. V. L. Narasimhan, V. U. S. Rao, R. L. Bergner and W. E. Wallace, J. Appl. Phys. 46, 4957 (1975).

62 K. S. V. L. Narasimhan, V. U. S. Rao, W. E. Wallace and I. Pop, A. I. P. Conf. Proc. No. 29, 594 (1975).

63 H. Kido, T. Hoshikawa, M. Schimada and M. Koizumi, Powder and Powder Metallurgy 31, 29 (1984).

64 R. Obermyer, S. G. Sanker and V. U. S. Rao, J. Appl. Phys. 50, 2312 (1979).

65 S. Siek, A. Szytula and J. Leciejewicz, phys. stat. sol. (a) 46, K101 (1978).

66 E. V. Sampathkumaran, R. S. Chughule, K. V. Gopalakrishnan, S. K. Malik and R. Vijayaraghavan, J. Less-Common Met. 92, 35 (1983).

67 A. Szytula, I. Szott, Solid State Commun. 40, 199 (1981).

68 H. Pinto and H. Shaked, Phys. Rev. 7, 3261 (1973).

69 A. Szytula, W. Bazela and J. Leciejewicz, Solid State Commun. 48, 1053 (1983).

70 H. Pinto, M. Melamud, J. Gal, H. Shaked and G. M. Kalvins, Phys. Rev. B27, 1861 (1983).

71 J. Leciejewicz, S. Siek, A. Szytula and A. Zygmunt, "Proc. Int. Conf. on Crystalline Electric Field and Structural Effects in f-electron System, Wroclaw 1981, Edited by R. P. Guertin, W. Suski and Z. Zolnierek, p. 327. Plenum Press, New York, 1982.

72 J. Leciejewicz, H. Kolenda and A. Szytula, Solid State Commun. 45, 145 (1983).

73 Z. Ban, L. Omejec, A. Szytula and Z. Tomkowicz, phys. stat. sol. (a)27, 338 (1975).

74 P. A. Kotsanidis, J. K. Yakinthos and E. Roudaut, Solid State Commun. 50, 413 (1984).

75 M. Shimada, N. Ogawa, M. Koizumi, F. Dachille and R. Roy, Amer. Ceram. Soc. Bull. 58, 519 (1979).

76 W. Rieger and E. Parthe, Monatsh. Chem., 100, 439 (1969).

77 O. I. Bodak, E. I. Gladyshevskii, and P. I. Kripyakevich, Zh. strukt. Khim., 11, 283 (1970).

78 I. Mayer and I. Felner, J. Solid State Chemistry 7, 292 (1973).

79 H. Kido, M. Shimada and M. Koizumi, phys. stat. sol. (a)70, K23 (1982).

80 H. Kido, T. Hoshikawa, M. Shimada and M. Koizumi phys. stat. sol. (a)77, K121 (1983).

81 H. Kido, T. Hoshikawa, M. Schimada and M. Koizumi, phys. stat. sol. (a)80, 601 (1983).

82 W. D. Kingery, H. K. Bowen and D. R. Uhlmann, "Introduction to Ceramics" p. 402, John Wiley & Sons, New York, 1976.

83 M. S. Crowley, Bull. Am. Ceram. Soc. 46, 679 (1967).

84 H. Kido, T. Hoshikawa, M. Shimada and M. Koizumi, phys. stat. sol. (a)88, K39 (1985).

85 "Butsuri Teisū Hiyō", Asakura Shoten, Tokyo, 1978.

86 H. Kido, T. Hoshikawa, M. Shimada and M. Koizumi, phys. stat. sol. (a)83, 561 (1984).

87 H. Kido, T. Hoshikawa, M. Shimada and M. Koizumi, phys. stat. sol. (a) 90, (1985) in press.

88 H. Kido, T. Hoshikawa, M. Shimada and M. Koizumi, phys. stat. sol. (a)87, 273 (1985).

89 A. Brown, Acta Cryst. 14, 860 (1961).

90 J. C. Slater, Phys. Rev. 36, 57 (1930).

91 A. J. Dekker, J. Appl. Phys. 36, 906 (1965).

92 V. U. S. Rao and W. E. Wallace, Phys. Rev. B2, 4613 (1970).

93 Yu. V. Serdyuk, R. P. Krentsis, P. V. Gel'd and V. G. Batalin, Fiz. Tverd. Tela 22, 2149 (1980).

94 M. A. Ruderman and C. kittel, Phys. Rev. 96, 99 (1954).

95 Yu. V. Serdyuk, R. P. Krentsis and P. V. Gel'd, Fiz. Tverd. Tela 23, 2716 (1981).

96 T. Kasuya, Prog. Theor. Phys. 16, 58 (1956).

97 T. Kasuya, Prog. Theor. Phys. 22, 227 (1959).

98 T. van Peski-Tinbergen and A. J. Dekker, Physica 29, 917 (1963).

99 S. Bakanowski, J. E. Crow, N. F. Berk and T. Mihalisin, Solid State Commun. 17, 111 (1975).

100 N. F. Mott and H. Jones, "The Theory of the Properties of Metals and Alloys", Clarendon Press, Oxford, 1936.

101 J. S. Dugdale, " The electrical Properties of Metals and Alloys", Edward Arnold Ltd., London, 1977.

PUBLICATION LIST

1 "Synthesis and Magnetic Properties of GdCoSi and GdMnSi", H. Kido, M. Shimada and M. Koizumi, phys. stat. sol. (a) 70, K23 (1982).

2 "Synthesis and Magnetic Properties of RCuSi (R=Y, Ce, Nd, Sm, Gd, Ho)", H. Kido, T. Hoshikawa, M. Shimada and M. Koizumi, phys. stat. sol. (a) 77, K121 (1983).

3 "Preparation and Magnetic and Electrical Properties of RZnSi", H. Kido, T. Hoshikawa, M. Shimada and M. Koizumi, phys. stat. sol. (a) 80, 601 (1983).

4 "Synthesis and Magnetic Properties of RMn_2Si_2 (R=Y, Nd, Gd) and YNi_2Si_2", H. Kido, T. Hoshikawa, M. Shimada and M. koizumi, J. Jpn. Soc. Powder and Powder Metallurgy 31, 29 (1984).

5 "Crystal Structure and Magnetic and Electrical Properties of GdMSi (M=First-row Transition Metal)", H. Kido, T. Hoshikawa, M. Shimada and M. Koizumi, J. Less-Common Met. 99, 151 (1984).

6 "Crystal Structure and Magnetic and Electrical Properties of Pseudo-Ternary $GdCu_{1-x}Zn_xSi$ Compounds", H. Kido, T. Hoshikawa, M. Shimada and M. Koizumi, phys. stat. sol. (a) 83, 561 (1984).

7 "Crystal Structure and Magnetic and Electrical Properties of Pseudo-Ternary $HoCu_{1-x}Zn_xSi$ and $NdCu_{0.6}Zn_{0.4}Si$ Compounds", H. Kido, T. Hoshikawa, M. Shimada and M. Koizumi, phys. stat. sol. (a) 87, 273 (1985).

8 "Preparation and Magnetic Properties of $YMn_2(Si_{1-x}Ge_x)_2$ Compounds", H. Kido, T. Hoshikawa, M. Shimada and M. Koizumi, phys. stat. sol. (a) 87, K61 (1985).

9 "Preparation and Magnetic Properties of YMnSi", H. Kido, T. Hoshikawa, M. Shimada and M. Koizumi, phys. stat. sol. (a) 88, K39 (1985).

10 "Crystal Structure and Magnetic and Electrical Properties of Pseudo-Ternary $DyCu_{1-x}Zn_xSi$ Compounds" H. Kido, T. Hoshikawa, M. Shimada and M. Koizumi, phys. stat. sol (a) 90, (1985) in press.